ULTRAFAST EXCITED-STATE STRUCTURAL DYNAMICS AND CHARGE TRANSFER IN PHOTORESPONSIVE CONJUGATED MOLECULAR MATERIALS

by

Jiawang Zhou

A dissertation submitted to Johns Hopkins University in conformity with the requirements for the degree of Doctor of Philosophy

Baltimore, Maryland

August, 2016

© 2016 Jiawang Zhou

All Right Reserved

Abstract

As many fundamental light-induced photochemical processes, e.g. isomerization, intramolecular electron or hydrogen transfer, happen on timescales ranging from femtoseconds to picoseconds, further understanding of these intriguing phenomena at the molecular level requires powerful tools to efficiently probe ultrafast excited-state dynamics. Femtosecond transient absorption spectroscopy (TAS) has proven to be a valuable method for interrogating excited-state evolution, providing significant insight about the nature of the elementary reactions that control the macroscopic properties of photo-activated systems and how they are influenced by the local environment. On the other hand, transient electronic spectroscopy reveals limited information about structural evolution, unlike vibrationally resolved spectroscopy. Femtosecond stimulated Raman spectroscopy (FSRS) provides access to this level of detail, and is also highly compatible and complementary to TAS. The scope of this dissertation involves application of both TAS and FSRS to the interrogation of structural and charge-transfer dynamics in various photo-responsive conjugated materials.

Chapter 2 presents the study of S_1 structural relaxation in two quaterthiophenes as probed by FSRS. This is a good example where a vibrationally resolved method is more suitable to examine the structural dynamics of a molecular material on sub-ps timescales, while TAS cannot specifically characterize such a detailed process merely on electronic level.

Chapter 3 describes the interrogation of E/Z photoisomerization found in a novel diarylethene derivative. This photoswitchable molecule operates through state-selective (E and Z isomer) photoactivation with visible light. The ensuing mechanistic study by

TAS reveals that this structural switching occurs via multiplicity-exclusive photoisomerization pathways.

Chapter 4 focuses on the intramolecular charge transfer (ICT) and recombination in σ-π conjugated organosilanes upon photo excitation. Results from steady-state spectroscopies imply the occurrence of excited-state ICT in these donor-acceptor complexes, which has been definitively proven by FSRS. Meanwhile, the charge recombination process is comprehensively studied by TAS regarding the dependence of central oligosilane length and solvent.

Chapter 5 describes excited-state intramolecular hydrogen transfer in benzoindolizine (bi). Two bi compounds with different substituents exhibit dramatically distinct fluorescence behaviors upon protonation. TAS reveals that the electron donating group in the protonated bi compound can facilitate hydrogen transfer in the excited state, thus quenching the radiative relaxation pathway.

Thesis Committee: Arthur E. Bragg (Advisor), Paul J. Dagdigian and Harris J. Silverstone

Acknowledgements

I would like to thank my parents for all their support and education for the past twenty eight years. I feel that I can always learn something valuable from them, which is not available in textbooks or laboratories. Their unconditional love consistently helps me go through every difficulty in my life.

I want to express my sincere appreciation to my research advisor Dr. Arthur Bragg for his extraordinarily conscientious and meticulous instructions. I thoroughly enjoy the freedom in the laboratory where I can individually design and carry out experiments to explore new subjects with his professional suggestions.

I would like to acknowledge my research collaborators. Xin Guo first synthesized the diarylethene derivative described in Chapter 3, which led to the first Angewandte Chemie and JACS papers in our group. Cody Pitts not only synthesized samples for us, but also taught me basic synthesis skills. Sravan Surampudi and Victor Outlaw also made fabulous molecules that exhibit excited-state charge and hydrogen transfer, respectively. I also highly appreciate my coworkers, especially Wenjian Yu, Joshua Snyder and Timothy Magnanelli, who enabled my progress in the past six years.

I want to thank my committee members, professors, colleagues at Chemistry Department, for their great helps from different perspectives towards my research.

Last but not least, I am extremely grateful to all my family members and friends. I cannot describe how lucky I am to have you in my life.

Table of Contents

Chapter 1: Introduction to Photo-Responsive Conjugated Materials and Ultrafast Spectroscopies 1
1.1 Photo-responsive conjugated materials 1
1.1.1 Structural relaxation in excited-state quaterthiophenes 2
1.1.2 Visible light-triggered molecular photoswitch 3
1.1.3 Photo-induced charge transfer in organosilanes 4
1.1.4 Excited-state effective hydrogen shift in a pH-responsive fluorophore (benzoindolizine) 6
1.2 Femtosecond transient absorption spectroscopy (TAS) 8
1.3 Femtosecond stimulated Raman spectroscopy (FSRS) 11
1.4. References 16
Chapter 2: Structural Relaxation of Photoexcited Quaterthiophenes Probed with Vibrational Specificity 20
2.1. Introduction 20
2.2. Experimental materials 22
2.3. Computational methods 23
2.4. Results and discussion 24
2.5. Supporting material 37
2.5.1. Steady-state UV-Vis and fluorescence spectroscopy of 4T and DH4T 37
2.5.2. Quantum-chemical calculations 37
2.5.3. Transient absorption spectroscopy (TAS) of 4T 42
2.5.4. TAS of relaxed S_1 4T and DH4T (2 ps pump-probe delay) 43
2.5.5. Fitting of weighted average wavelength of 4T and DH4T stimulated emission 44
2.5.6. Additional details of experimental setup 45
2.5.7. FSRS signal analysis procedures 45
2.6. References 48
Chapter 3: Visible-Light-Induced E/Z Isomerization of a 1,2-Dicyanoethene Derivative via Multiplicity-Exclusive Photoisomerization Pathways 52
3.1. Introduction 52

3.2. Experimental and computational methods ... 57
3.2.1. Sample preparation and characterization. ... 57
3.2.2. Transient absorption (TA). ... 58
3.2.3. Computational. ... 59
3.3. Experimental results ... 60
3.3.1. Photoinduced dynamics of *trans*-4TCE. ... 60
3.3.2. Photoinduced dynamics of *cis*-4TCE. ... 65
3.3.3. Triplet-sensitized energy transfer. ... 69
3.3.4. Computational results. ... 71
3.4. Discussion. ... 74
3.4.1 Energy-dependent relaxation pathways and photoswitching mechanisms. ... 74
3.4.2 Photoisomerization of 4TCE through the triplet manifold. ... 77
3.5. Conclusions ... 81
3.6. Supporting material ... 84
3.6.1. Measurement of isomerization quantum yields at 420 nm ... 84
3.6.2. Actinometry ... 87
3.6.3. Data acquisition of transient spectra ... 88
3.6.4. Translation stage alignment. ... 88
3.6.5. Fitting and comparison of GSB, SE and STA spectral dynamics in TAS of trans-4TCE following 530-nm photoexcitation ... 89
3.6.6. Separation of GSB and SE contributions to TAS of *trans*-4TCE photoexcited at 420 and 530 nm ... 90
3.6.7. Global analysis of *trans*-4TCE TAS following 420-nm excitation ... 93
3.6.8. Fitting and comparison of STA 2 spectral dynamics in TAS of *cis*-4TCE following 530-nm and 420-nm photoexcitation ... 94
3.6.9. Fitting of STA 1 spectral dynamics in TAS of cis-4TCE following 530- nm excitation... 95
3.6.10. Global analysis of *cis*-4TCE TAS following 420-nm excitation. ... 96
3.6.11. Nanosecond TAS measurements ... 96
3.6.12. Excitation-dependent transient spectra of *trans*-4TCE 1 ns after excitation ... 97
3.6.13. Excitation-dependent transient spectra of *cis*-4TCE 2 ps and 316 ps after excitation ... 99
3.6.14. Quantum-chemical calculations ... 102
3.7 References ... 106

Chapter 4: Photoinduced Charge Separation and Recombination in σ-π Conjugated Organosilanes 113

4.1. Introduction 113

4.2. Experimental methods 115

4.3. Results and discussion 116

4.4. Supporting material 129

4.4.1. General Information 129

4.4.2. Time-resolved transient absorption (TA) spectra of 1b in CH_2Cl_2 following 360-nm excitation 130

4.4.3. Acquisition algorithms for femtosecond stimulated Raman spectroscopy (FSRS) 131

4.4.4. Time-resolved FSRS spectra of 1b in CH_2Cl_2 following 360-nm actinic and 480-nm Raman excitations 133

4.4.5. Fitting of ring-stretching mode intensity of 1b in CH_2Cl_2 observed with FSRS following 360-nm actinic excitation 134

4.4.6. Quantum-chemical calculations 135

4.5 References 139

Chapter 5: Quenching of pH-Responsive Luminescence of a Benzoindolizine Sensor by Ultrafast Hydrogen Shift 142

5.1. Introduction 142

5.2. Experimental methods 143

5.3. Computational methods 144

5.4. Results and discussion 145

5.5. Supporting material 155

5.5.1. Dispersed fluorescence spectra of $biMeH^+$ and $biOMeH^+$ in CH_3CN, $CHCl_3$, toluene and CH_3OH 155

5.5.2. NMR spectra of neutral and protonated biMe and biOMe in CD_3OD 156

5.5.3. Fitting of time-dependence of $biMeH^+$ excited-state absorption (ESA) following 360-nm excitation 157

5.5.4. Fitting of transient shift in SE peak position for $biMeH^+$ following 360-nm excitation 158

5.5.5. TAS of biMe in CH_3OH following 360-nm excitation 159

5.5.6. Decay-associated spectra obtained from global analysis of $biOMeH^+$ TAS (~ 0 – 21 ps) following 360-nm excitation 160

5.5.7. Decay-associated spectra from global analysis of biOMeH$^+$ TAS 21 – 1000 ps following 360-nm excitation 161

5.5.8. TAS of biOMe in CH_3OH following 360-nm excitation 162

5.5.9. Concentration-dependent fluorescence spectroscopy of biOMeH$^+$ in CH_3OH 163

5.5.10. Acid-responsive optical properties of other benzo[1,2-*b*]indolizines compounds .. 164

5.5.11. Quantum-chemical calculations 164

5.6 References 173

Curriculum Vitae 176

List of Figures

Figure 1.1. Diagram showing the multiplicity-exclusive E/Z photoisomerization pathways of 4TCE ... 4

Figure 1.2. Direct photoinduced intramolecular charge transfer in an organosilane ... 6

Figure 1.3. Observed blue shift in emission upon protonation of 2-methyl-6-amino-8-cyanobenzo[1,2-b]indolizine ... 8

Figure 1.4. Jablonski diagram outlining the photophysical relaxation mechanisms of protonated methylated (biMeH$^+$) and methoxylated (biOMeH$^+$) bi compounds ... 8

Figure 1.5. Comparison between steady-state and transient spectroscopies ... 9

Figure 1.6. Layout for the transient absorption spectroscopy (TAS) set up ... 11

Figure 1.7. Pulse sequence and timing in FSRS ... 13

Figure 1.8. Schematic representation of the energy diagram for a time-resolved FSRS experiment ... 14

Figure 1.9. Layout for the femtosecond stimulated Raman spectroscopy set up. ... 14

Figure 2.1. Time-dependence of three major FSRS features obtained from (a) 4T and (b) DH4T following photoexcitation at 350 nm. (c) The blue and red lines plot the FSRS spectra of photoexcited 4T and DH4T, respectively, obtained 2 ps after photoexcitation. Residual solvent signals are marked with asterisks. ... 27

Figure 2.2. Normalized time-resolved intensities for ring deformation, in-phase C=C (Я) and out-of-phase C=C (Z) stretching modes of (a) 4T and (b) DH4T following photoexcitation at 350 nm. The C-S-C deformation and Я intensities are offset to those of Z for clarity. (c) Ratio of out-of-phase to in-phase feature intensities (ROI) for 4T and DH4T. The ROI for DH4T is multiplied by 0.25 for better visual comparison. Both curves are fit well with a single exponential function with timescale of 0.40 and 1.73 ps, for 4T and DH4T, respectively. ... 29

Figure 2.3. Comparisons of weighted peak positions of (a) out-of phase C=C (Z) and (b) in-phase C=C (Я) and ring deformation modes of 4T and DH4T excited at 350 nm. The blue shift of Z mode of both quaterthiophenes can be well fitted with a single exponential function with timescale of 0.40 and 0.86 ps, for 4T and DH4T, respectively. ... 31

Figure 2.4. Calculated frequencies of the in-phase and out-of-phase C=C stretching modes of 2T as a function of torsional dihedral angle, θ. ... 32

Figure 2.1S. Normalized steady-state UV-Vis absorption and fluorescence spectra of 4T and DH4T dissolved in chlorobenzene (CB) $(2.0 \times 10 - 3$ M). The structures of 4T and DH4T are shown in the inset. The relative UV-Vis peak position for DH4T (compared to 4T) can be attributed to the effect of the alkyl substituents on the structure (vide infra) and, therefore, π conjugation of the oligothiophene chromophore in its ground state. 37

Figure 2.2S. S_0 optimized structure of 4T viewed from top (above) and side (bottom). 38

Figure 2.3S. S_0 optimized structure of DE4T viewed from top (above) and side (bottom). 38

Figure 2.4S. S_1 optimized structure of 4T viewed from top (above) and side (below). 39

Figure 2.5S. S_1 optimized structure of DE4T viewed from top (above) and side (below). 39

Figure 2.6S. Visualization of the (a) in-phase C=C stretch mode (above) and out-of-phase C=C stretch mode (below) in S_0 2T, 4T and DH4T and (b) ring deformation mode (above), in-phase C=C stretch mode (middle) and out-of-phase C=C stretch mode (below) in S_1 2T, 4T and DH4T. All the calculated frequencies from 4T and DH4T are consistently higher than those measured experimentally and presented in the main text, as no frequency scaling factors have been applied. Figures were prepared using GaussView 5.0. 40

Figure 2.7S. (a) Calculated ER of 2T compared with the FSRS spectra of photoexcited 4T and DH4T obtained 2 ps after photoexcitation. Although an intense H bending mode and a C-C interring stretching mode predicted at 1107 cm^{-1} and 1695 cm^{-1} do not appear in the experimental spectra, the positions of the three main excited-state Raman bands observed are identified and are in qualitative accord with the results of the Raman intensity calculation. (b) Frequencies and intensities of the in-phase and out-of-phase C=C stretching modes of 2T as a function of torsional dihedral angle, θ, plotted at the left and right side of the break, respectively. When θ varies from 40 to 0 degree, the Я mode shows only a 3-cm^{-1} blue shift and modest intensity increase, whereas the Z mode exhibits a 16-cm^{-1} blue shift and an 8.5 fold intensity decrease. 41

Figure 2.8S. TAS spectra of 4T at (a) early and (b) late delays following photoexcitation at 420 nm in CB. (The uneven spectral shapes occur near the driving wavelength for white-light generation between 720 and 840 nm.) Early delays illustrate the appearance and relaxation of the S_1 state; the latter is most apparent from the time-dependent position of the stimulated emission (described further below). Data collected on later delays illustrate that S_1 4T decays in part via ISC to the triplet manifold, with characteristic triplet features near 600 nm. 42

Figure 2.9S. Comparison of normalized TAS spectra of 4T and DH4T at a 2 ps time delay following photoexcitation at 420 nm in chlorobenzene (CB). (The uneven spectral shapes occur near the driving wavelength for white-light generation between 720 and 840 nm.) Transient spectra of the two species are highly similar. Raman–excitation wavelengths used in our experiments were chosen to be resonant with the red edge of the S_1 absorption band (850 and 880 nm for 4T and DH4T, respectively). 43

Figure 2.10S. Weighted average wavelength of the simulated emission of (a) 4T and (b) DH4T. Weighted average wavelengths were determined between 460 and 505 nm. Shifting timescales are similar to the relaxation time-scales obtained from Raman spectra (main text) and are similar to relaxation timescales obtained for 4T analogs via TAS previously.[14] 44

Figure S2.11. (a) Raw FSRS data of DH4T at 0.6 ps time delay and solvent subtraction routine. GR was multiplied by a factor m = 0.66 and employed to fully subtract the solvent and any non-resonant solute features from RC. Residual solvent signals are marked with asterisks. The RC – GR (i.e. ER) spectrum is offset vertically for clarity. (b) Removal of residual baseline. The ER spectrum was first smoothed in a Labview Program (Savitzky-Golay filter, polynomial order = 3, side points = 16). The baseline shape was determined with a linear spline. Finally the estimated baseline was subtracted from the smoothed ER spectrum to generate the baseline free ER...... 47

Figure 3.1. (a) UV-vis absorption spectra of pure cis and trans isomers of 4TCE in toluene solution (the same below) at room temperature. Insets: calculated UV-vis spectra (top right) and a picture showing the obviously different color of two isomers in solution. (b) E→Z photoisomerization of the 4TCE, irradiated by white light. (c) Z→E photoisomerization of the 4TCE, irradiated by blue light at 420 nm. (d) Thermal Z→E isomerization of the 4TCE. All these experiments are carried out in 10^{-5} M solutions. 55

Figure 3.2. Transient absorption (TA) spectra of *trans*-4TCE in chlorobenzene excited at (a) 530 nm and (b) 420 nm. (a) Spectral evolution is characterized by decay of all three signals (GSB, SE, and STA) within 500 ps. A permanent GSB signal persists on longer timescales, reflecting that a fraction (11.6 %) of the excited state population isomerizes. (b) Spectral evolution is similar to that observed after 530-nm excitation at delays earlier than 20 ps, but exhibits signatures of triplet absorption on longer timescales.. 62

Figure 3.3. (a) TA spectra of *cis*-4TCE in chlorobenzene following 530-nm excitation: Spectral dynamics are similar to those observed for the *trans* isomer, but exhibit negligible signatures of isomerization. TA spectra of *cis*-4TCE in chlorobenzene excited at 420 nm (b) ~0-30 ps and (c) after 30-1500 ps. (b) Ultrafast ISC occurs in the first 2 ps, with a decay of STA 1 at 720 nm and an appearance of TTA at 620 nm. (c) From 30 to 1500 ps the intensity of TTA is substantially reduced, while absorption of the S_0 *trans* isomer concurrently appears between 450 and 560 nm. This *cis*-to-*trans* ISC is evidenced by the isosbestic point at 556 nm. 67

Figure 3.4. Evolution of UV-vis spectra recorded during 650 nm light illumination (I = 2.6 mW) of (a) *cis*-4TCE (c = 2.2×10^{-5} M) and methylene blue (MB, c = 4.6×10^{-6} M) and (b) trans-4TCE (c = 3.2×10^{-5} M) and MB (c = 1.2×10^{-5} M) in acetonitrile. Neither solution was degased................... 71

Figure 3.5. Diagram of calculated state energies for 4TCE. Energies of singlet excited states are evaluated at the optimized ground-state geometry. The S_1 geometries of both isomers were also optimized; high-lying triplet levels were calculated from the S_1 minimum geometries. Although isomerization likely involves multiple coordinates, the dihedral angle of the central ethylene is anticipated to be significant. Relaxed PES scans of S_0 and T_1 were performed in steps of 10 deg. These two potential curves intersect near $\theta = 90^{o}$.. 73

Figure 3.6. Schematic of isomerization pathways for 4TCE excited at (a) 530 nm and (b) 420 nm. For 530 nm excitation 11.6% of S_1 *trans* isomer undergoes isomerization to *cis*. For 420 nm excitation the relaxation for both isomers occurs in the triplet manifold. Ultrafast ISC (~2 ps) occurs in *cis*-4TCE, and *cis*-to-*trans* isomerization occurs through the T_1/S_0 coupling on a timescale of 0.4 ns. 75

Figure 3.1S. Exponential fit of the *trans* molar fraction vs. the integrated photokinetic factor x.86

Figure 3.2S. Intensities at 600 and 740 nm are fitted with a biexponential function, exhibiting decay on both 2-3 ps and 38 ps timescales. GSB intensity at 510 nm recovers with a lifetime of 39.2 ps. Best-fit timescales for each trace are presented in Table 3.1 in the main text. 89

Figure 3.3S. TAS with the GSB components subtracted are shown in (a) and (b) for 530 nm and 420 nm excitation of *trans*-4TCE, respectively. 91

Figure 3.4S. The intensity weighted averaged wavelength of the isolated SE bands were calculated for 530 nm pump (averaged from 550 to 630 nm region) and 420 nm pump (averaged from 550 to 620 nm region) TAS, and the single exponential fit results are plotted in (a) and (b), respectively. The band area from 550 to 620 nm region was also calculated for the 420 nm excitation TAS, and it is shown in (c). For 420 nm pump TAS the time delays only extend up to 10 ps, since ISC begins to occur at longer delays. 92

Figure 3.5S. The TAS of *trans*-4TCE with 420 nm excitation was globally fitted between 10 ps and 215 ps using a sequential kinetic interconversion model for ISC, producing an S_1 lifetime of 40.0 ps. Experimental data at selected probe wavelengths (525, 570, 620, 715 nm) are plotted and compared with the global fits. 93

Figure 3.6S. Absorption decays at 452 nm and 472 nm were chosen to present the spectral dynamics of the STA 2 band following 530-nm and 420-nm excitation of *cis*-4TCE. Exponential fits give excited-state relaxation timescales of 4.8 ps and 3.6 ps, respectively. 94

Figure 3.7S. The intensity at 700 nm of TAS of *cis*-4TCE was chosen to present the spectral dynamics of the STA 1 band with 530-nm excitation and was fit with a biexponential function. Experimental data are plotted and compared with fits. 95

Figure 3.8S. The TAS of *cis*-4TCE photoexcited with 420 nm was globally fitted between 30 ps and 1500 ps using a sequential kinetic interconversion model for relaxation from the T_1 state to S_0 trans, which returns a 396 ps lifetime. Experimental data at selected probe wavelengths (485, 525, 615, 680 nm) are plotted and compared with the global fits. 96

Figure 3.9S. Average intensity for the SE (390-410 nm) and TTA (550-600 nm) obtained via nanosecond TAS with (a) *trans* and (b) *cis* isomers. 97

Figure 3.10S. TA spectra captured 1 ns after excitation with various wavelengths covering the S_1 absorption of *trans*-4TCE (360 to 530 nm). Time-resolved spectra were normalized according to SE peak intensity at 528 nm at a delay of 10 ps. TA spectra obtained with 460 to 530 nm match the steady-state difference spectrum between *cis* and *trans* isomers, whereas higher energy excitation leads to increased triplet absorption. 99

Figure 3.11S. TA spectra of *cis*-4TCE collected with various excitation wavelengths at (a) 2-ps and (b) 316-ps time delays; both sets are normalized according to the STA 2 peak intensity at 2 ps. A consistent red shift of the STA 2 is observed with increased pump energy. Excitations at low energy (between 460 and 530 nm) give a signal of STA 1 and SE, whereas high-energy excitations (420 and 440 nm) lead to TTA centered at 620 nm. 101

Figure 3.12S. Natural transition orbital analysis of S_1, S_2, S_4 for *cis* and S_1, S_6 for *trans* 106

Figure 4.1. FTIR spectra of **1a** in a film and **1b** and **3a** in dichloromethane solution. Calculated IR spectra of **1a**, neutral **3b** and reduced **3b**$^{\cdot-}$ are plotted for comparison. Spectra are scaled according to the C=O feature intensity. 118

Figure 4.2. UV-Vis absorption (solid lines) and dispersed fluorescence (dash lines) of **1b** in various solvents. Second-order scatter from the fluorescence excitation (360 nm) is marked with an asterisk. The emission peak red-shifts with increasing solvent polarity (noted by the black arrow) 119

Figure 4.3. Lippert plot of emission Stokes shift, Δv, vs. solvent orientation polarizability, Δf, for **1a-c** 120

Figure 4.4. TA spectra of **1b** in dichloromethane solution (red) and **1d** cast as a film (black) probed 1 ps after excitation at 360 nm. The TA spectrum of the **1d** film is scaled by a factor of four for comparison with solution data. Inset: Transient decay of excited **1b** in solution as probed at 450 nm. 122

Figure 4.5. Excited-state Raman (ER) of **1a-c** and ground-state Raman (GR) of **1c** in dichloromethane with 360 nm actinic and 480 nm Raman excitations. The time delay between actinic and Raman pulses is 10 ps. Calculated Raman spectra of neutral and reduced forms of **3b** are also plotted for comparison. Residual solvent signals at 1139 and 1415 cm^{-1} are marked with asterisks. 123

Figure 4.6. TA spectra of **1c** in $CHCl_3$ following 405 nm excitation: (a) ~ -0.25 – 0.3 ps (b) ~ 0.4 – 12.5 and (c) ~ 15.7 – 681 ps. 127

Figure 4.1S. TA spectra of **1b** in CH_2Cl_2 excited at 360 nm (a) before and (b) after 5 ps. 130

Figure 4.2S. (a) Raw ER and GR spectra and their difference after scaled subtraction. In order to fully remove the solvent signal, a scaling factor of 0.89 has been determined using the intensity of the 700 cm^{-1} solvent feature. (b) The broad baseline remaining is fit with a second-order polynomial, and contributions to the spectrum from only Raman-active excited-state vibrations are isolated by baseline subtraction. No spectral smoothing process has been applied. Residual solvent signals from imperfect subtraction are marked with asterisks. 132

Figure 4.3S. Time-resolved excited-state Raman spectra from **1b** in dichloromethane with 360 nm actinic and 480 nm Raman excitations. Ground-state Raman signals have been scaled based on the size of the solvent peak at 700 cm^{-1} and subsequently subtracted at all delays. The broad baseline has not been removed and the entire spectra are presented without smoothing. Residual solvent signals at 1139 and 1415 cm^{-1} are marked with asterisks. 133

Figure 4.4S. A single exponential fit to the intensity of the ring stretching mode returns a lifetime of 66 ps. The different in the lifetimes obtained from TA and FSRS arises from the different polarization conditions of these measurements: in TA the angle polarization of the pump and probe pulses is set to magic angle, whereas in FSRS all polarization directions of the actinic pump, Raman pump and probe are parallel. Consequently, the lifetime estimated from FSRS is considerably shorter than that from TA, as it includes relaxation of the polarization anisotropy not present in magic angle TA measurements. 134

Figure 4.5S. S_0 optimized structure of neutral acceptor. 135

Figure 4.6S. S_0 optimized structure of negatively charged acceptor.. 136

Figure 4.7S. Strongly Raman-active vibrational mode of the neutral acceptor (present in FSRS spectrum).. 137

Figure 4.8S. Weakly Raman-active vibrational modes of the neutral acceptor (not apparent in experimental FSRS spectrum).. 137

Figure 4.9S. Strongly Raman-active vibrational modes of the reduced acceptor (present in experimental FSRS spectrum). In Figure 3 of the main text the three FSRS features in the region between 1000 and 1400 cm^{-1} can be assigned as Si-C stretching at 1085 cm^{-1}, C-H bending at 1197 cm^{-1} and C-H rocking on the aryl ring at 1333 cm^{-1}... 138

Figure 4.10S. Weakly Raman-active vibrational modes of the reduced acceptor (not apparent in the experimental FSRS spectrum).. 139

Figure 5.1. (a) UV-Vis and (b) fluorescence spectra of biMe and (c) UV-Vis and (d) fluorescence spectra of biOMe upon addition of TFA (vol %).The concentrations of biMe and biOMe in fluorescence measurement are 5.4 µM and 2.8 µM, respectively.. 147

Figure 5.2. Normalized absorption (solid) and dispersed fluorescence (dashed) of $biMeH^+$ and $biOMeH^+$ in MeOH. Fluorescence excitation – 370 nm. 147

Figure 5.3. TA spectroscopy of $biMeH^+$ in MeOH following 360 nm excitation (a) ~ 0 – 56 ps (b) ~ 56 – 1000 ps.. 149

Figure 5.4. TA spectroscopy of $biOMeH^+$ in MeOH following 360 nm excitation (a) ~ 0 – 21 ps (b) ~ 21 – 1000 ps. Insets: Experimental data at selected probe wavelengths (symbols) compared with global fits (solid lines) from three- and two-state interconversion models in (a) and (b), respectively. 151

Figure 5.5. Optimized structures of S_0 T1, and S_1 T1, a C-8 protonated intermediate (Int), and T2. The H shifted is highlighted in light blue. 153

Figure 5.1S. Normalized dispersed fluorescence spectra of $biMeH^+$ (solid lines) and $biOMeH^+$ (dash lines) dissolved in CH_3CN, $CHCl_3$, toluene and CH_3OH excited at 360 nm. Neither sample exhibits significant solvatochromism relative to the large difference in emission peak for these two species. 155

Figure 5.2S. NMR analysis of (a) $biMeH^+$ and (b) $biOMeH^+$ in CD_3OD. Red arrows denote features that disappear due to facile H/D exchange. 156

Figure 5.3S. Excited-state absorption (ESA) of $biMeH^+$ in methanol as probed by TAS at 600 nm following 360-nm excitation. Time-dependent absorption (symbols) was fit with a convoluted biexponential function (red line), yielding decay time scales of 3.2 and 65 ps. The former dominates the decay and is consistent with the time-dependent shift in SE, whereas the latter may be associated with further vibrational cooling of the long-lived excited state. 157

Figure 5.4S. Single exponential fit of the intensity-weighted averaged wavelength of the SE band (averaged from 425 to 500 nm region) as measured following 360-nm excitation of biMeH$^+$ in CH_3OH. 158

Figure 5.5S. TA spectra of neutral biMe in CH_3OH following 360 nm excitation (a) ~ 0 – 0.6 ps (b) ~ 0.6 – 1000 ps. 159

Figure 5.6S. Decay-associated spectra obtained by global analysis of TAS of biOMeH$^+$ in CH_3OH ~ 0 – 21 ps following 360 nm excitation. Global analysis used a sequential kinetic interconversion model (A→B→C). 160

Figure 5.7S. Decay-associated spectra obtained by global analysis of TAS of biOMeH$^+$ in CH_3OH 21-1000 ps following 360-nm excitation. Global analysis used a sequential kinetic interconversion model (C→D). 161

Figure 5.8S. TA spectra of neutral biOMe in CH_3OH following 360 nm excitation (a) ~ 0 – 0.4 ps (b) ~ 0.4 – 1000 ps. 162

Figure 5.9S. Normalized dispersed fluorescence spectra of biOMeH$^+$ in CH_3OH excited at 370 nm. No noticeable change in either band shape or band position is observed while the biOMeH$^+$ concentration is decreased from 240 to 2.5 µM. 163

Figure 5.10S. Fluorescence spectra excited at 370 nm of other benzo[1,2-b]indolizines compounds with TFA (vol %) titration in methanol. Their structures are displayed in the inset. 164

Figure 5.11S. S_0 optimized structure of biMeH$^+$ (N) viewed from top (above) and side (bottom). 165

Figure 5.12S. S_0 optimized structure of biMeH$^+$ (T1) viewed from top (above) and side (bottom). 166

Figure 5.13S. S_0 optimized structure of biMeH$^+$ (T2) viewed from top (above) and side (bottom). 166

Figure 5.14S. S_0 optimized structure of biOMeH$^+$ (N) viewed from top (above) and side (bottom). 167

Figure 5.15S. S_0 optimized structure of biOMeH$^+$ (T1) viewed from top (above) and side (bottom). 167

Figure 5.16S. S_0 optimized structure of biOMeH$^+$ (T2) viewed from top (above) and side (bottom). 168

Figure 5.17S. S_1 optimized structure of biMeH$^+$ (N) viewed from top (above) and side (bottom). 169

Figure 5.18S. S_1 optimized structure of biMeH$^+$ (T1) viewed from top (above) and side (bottom). 169

Figure 5.19S. S_1 optimized structure of biMeH$^+$ (Int) viewed from top (above) and side (bottom). 170

Figure 5.20S. S_1 optimized structure of biMeH$^+$ (T2) viewed from top (above) and side (bottom). 170

Figure 5.21S. S_1 optimized structure of biOMeH$^+$ (N) viewed from top (above) and side (bottom). 171

Figure 5.22S. S_1 optimized structure of biOMeH$^+$ (T1) viewed from top (above) and side (bottom). 171

Figure 5.23S. S_1 optimized structure of biOMeH$^+$ (int) viewed from top (above) and side (bottom). 172

Figure 5.24S. S_1 optimized structure of biOMeH$^+$ (T2) viewed from top (above) and side (bottom). 172

List of Tables

Table 3.1. Lifetimes from best-fit decay models for 4TCE excited at 420 and 530 nm................. 65

Table 3.2. Experimental and calculated energies of S_0-S_1 and S_0-T_1 energy gaps for 4TCE and MB (unit: eV). 70

Table 3.1S. DFT/TDDFT Calculated energies of the optimized S_0 geometries, S_1 Franck-Condon state, and S_1 minima for both isomers (unit: eV) 106

Table 4.1. Dipole moments for **1a-c** 121

Table 5.1. Calculated Energies, Absorption and Emission Gaps/Wavelengths of N, T1, T2, and C-8 Protonated (Int) Tautomers of biMeH$^+$ and biOMeH$^+$ in MeOH (DFT/TDDFT at CAM-B3LYP/6-31G*/PCM).. 148

Table 5.15S. Sums of natural charges for enamine (C6-NH$_2$), methylene (C7-H$_2$) and methine (C9-H) groups in the T1 tautomeric structure of the S_0 and S_1 biMeH$^+$ and biOMeH$^+$. 173

Table 5.16S. Natural charges for hydrogen in the T1 tautomeric structure of the S_1 biMeH$^+$ and biOMeH$^+$.. 173

List of Schemes

Scheme 2.1. The structures of 2,2′ :5′ ,2′ ′ :5′ ′ ,2′ ′ ′ −quaterthiophene (4T) and 3,3′ ′ ′ -Dihexyl-2,2′ :5′ ,2′ ′ :5′ ′ ,2′ ′ ′ −quaterthiophene (DH4T) 25

Scheme 4.1. Structures of organosilanes, the carbon analogue and the acceptor moiety 114

Scheme 5.1. 6-amino-8-cyanobenzo[1,2-*b*]indolizines (bi) and their protonated amino (N) and methylene (T1, T2) tautomers. 146

Chapter 1: Introduction to Photo-Responsive Conjugated Materials and Ultrafast Spectroscopies

1.1 Photo-responsive conjugated materials

Interaction between light and matter in the microscopic domain has fascinated researches since it show promising applications, such as solar energy harvesting, photoluminescence and photochromism. Photoactivated organic systems can have various distinct deactivation pathways, e.g. fluorescence, intersystem crossing, charge separation and transfer, etc., with relaxation timescales ranging from femtoseconds to seconds. Better utilization of these systems for various applications demands deeper understanding pertaining to these mechanisms and how they are determined intimately by reactant structure. Thanks to the advent of femtosecond lasers, it has been possible to extend research of these processes nearly to the moment of photoexcitation, where relaxation of highly excited electronic states, vibrational relaxation and fluorescence occur. Interrogation of these photoinduced dynamics is of fundamental interest as well as critical for developing photochemical and photophysical applications with molecular materials.

This thesis describes the use of transient absorption and femtosecond stimulated Raman spectroscopies to interrogate dynamics associated with excited-state conformational relaxation, isomerization, and electron and hydrogen transfer in conjugated organic molecular materials. Generally, the time scale of these fundamental dynamics falls within the regime of femtoseconds to picoseconds. By means of femtosecond stimulated Raman and transient absorption spectroscopies we aim to obtain deeper insights into dynamics of various photo-responsive materials, which are essential to enhancing their performances via additional structural modification or design.

Each project is briefly introduced below and thoroughly described in the following chapters.

1.1.1 Structural relaxation in excited-state quaterthiophenes

There is continuing interest in the photophysics of conjugated polymers (CPs), as CPs have significant processing advantages for manufacturing optoelectronic devices, including photovoltaics and light-emitting diodes.[1,2] CPs also present highly interesting questions regarding the nature of localized excitation (bond charge-pair excitons) in highly inhomogeneous systems and the structural features along an extended π-conjugated framework that are responsible for localizing transient states.[3,4] However, the complication arising from the structural inhomogeneity in CPs hinders precise characterization regarding the evolution of excitons and the dynamics of their localization. A sensible strategy to isolate signatures of structural dynamics, rather than exciton localization or charge separation, is to study oligothiophenes, since their well-defined structures will potentially give clean signatures associated with excited-state nuclear motions. Quaterthiophene, in particular, is the minimum thiophene oligomer necessary to model excited state dynamics in thiophene polymers, so this approach can be used to clarify the dynamics associated with an important broad class of materials.

In electronic transient absorption spectroscopy, the redshift of a stimulated emission band is a common signature for nuclear relaxation in conjugated systems.[5-7] However, it contains rather limited information pertaining to structural dynamics, such as planarization of the conjugated backbone in quaterthiophenes as predicted by computations.[8] On the other hand, Raman spectroscopy is a particularly powerful tool for monitoring the structural characteristics and nuclear dynamics of excited states according to the time- and excitation-dependence of vibrational spectra. Resonant enhancement increases Raman cross-sections and is highly sensitive to structural changes that occur along totally symmetric nuclear coordinates, like the benzoidal to quinoidal structural change that occurs in most conjugated polymers upon photoexcitation.[9] Additionally, the force constants of modes along the conjugated backbone (and particularly the C=C symmetric stretch) are related to the effective delocalization length.[10] With insight from quantum chemical calculation, we can closely monitor and analyze the ultrafast structural relaxation dynamics through these conformation-sensitive modes.

1.1.2 Visible light-triggered molecular photoswitch

Another intriguing photoresponse of conjugated materials is photochromism. Conventional photochromic molecules, like azobenzene (AB) and its derivatives, enjoy particular interest for applications such as optical memory and logic devices, or as molecular motors, machines, or manipulators due to their unique properties to be reversibly switched between two isomeric forms with different colors and structures.[11,12] Despite these advantages, AB suffers from a drawback that limits its practical use in biological and materials sciences, since the utilization of UV light, necessary to induce the Z → E isomerization via $\pi \rightarrow \pi^*$ excitation, may potentially lead to photodamage to other moieties attached to the AB unit.[13] Additionally, overlap between n-π^* bands of the two azobenzene isomers leading to low conversion yield.[14]

Recently we have reported that tetrathienyl-1,2-dicyano ethene (4TCE), can circumvent this limitation, because the very transition band associated with the Z → E isomerization falls within the visible region of the spectrum. Moreover, the visible absorption bands of both isomers are well separated, with a fairly large disparity in the oscillator strength, which gives rise to wavelength selectivity for exciting *cis* or *trans* isomer. Furthermore, TAS interrogation of 4TCE photophysics reveals that it switches via multiplicity-exclusive E/Z photoisomerization pathways. Specifically, *trans*-to-*cis* isomerization only occurs via electronic relaxation within the singlet manifold, whereas *cis*-to-*trans* isomerization happens via two rapid ISC processes into and out of the triplet manifold (Figure 1.1). The unique photoresponse of this system presented new possibilities for designing switches and tailoring their performance (e.g. manipulating spin-orbit couplings through variations in molecular structure or physical environment).

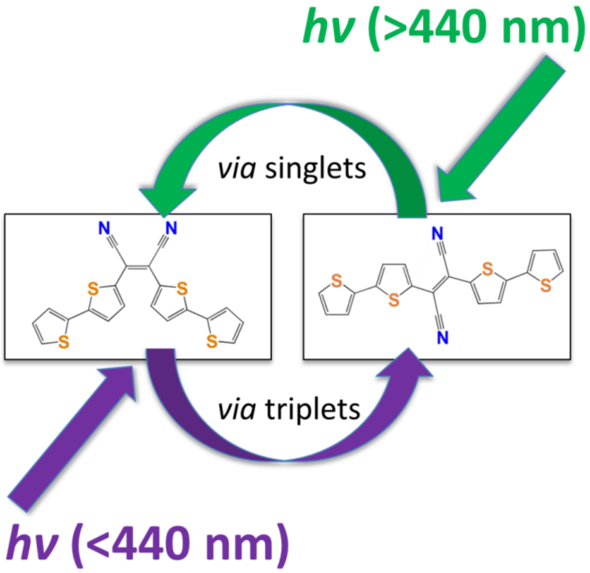

Figure 1.1. Diagram showing the multiplicity-exclusive E/Z photoisomerization pathways of 4TCE

1.1.3 Photo-induced charge transfer in organosilanes

Interest in molecular silicon semiconductors arises from the properties they shared with bulk silicon (e.g. material earth abundance) and the unique, flexible σ-conjugated architectures that are distinctly different from π-conjugated organic semiconductors. Promising steady-state conductivities have been measured for molecular silicon at the single molecule level.[15-17] More recently a series of oligosilane-arene σ, π-hybrid compounds have been synthesized; these comprise a peralkylsilane core capped by cyanovinyl groups and exhibit large device mobilities and facile charge transport in films.[18] However, there are few reports pertaining to the photoinduced intramolecular charge transfer, which is of great importance for the possibility of photovoltaic responses in molecular silicon-based devices.

Previous work exploring the photophysics of molecular silicon has primarily involved steady-state spectroscopic methods. UV-vis and fluorescence spectroscopies applied to linear permethlhexadecasilane ($Si_{16}Me_{34}$)[19] and permethylhexasilane (Si_6Me_{14})[20] to characterize their electronic spectroscopy in their singlet manifolds and in the presence of charge accepting molecules. Intermolecular charge transfer from oligosilane to the electron deficient tetracyanothylene (TCNE) has been probed by solution-phase EPR.[21,22] However, relatively little is known about mechanisms and therefore possibilities for rationally manipulating charge separation in molecular silicon materials with light. By means of FSRS and TAS, we demonstrate that photoexcitation of these compounds leads to a direct intramolecular charge transfer from the silane core donor to cyanovinyl acceptors (Figure 1.2). The rate of the ensuing charge recombination is closely related to silane chain length and polarity of the surrounding solvent medium and photoexcitation energy, which provides ways to precisely manipulate the charge transfer evolution in terms of microscopic structural modulation and local environmental control.

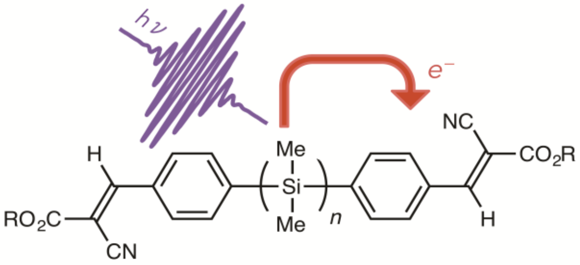

Figure 1.2. Direct photoinduced intramolecular charge transfer in an organosilane

1.1.4 Excited-state effective hydrogen shift in a pH-responsive fluorophore (benzoindolizine)

Stimuli-responsive fluorescent probes, such as pH-sensitive fluorophores, can serve as important tools to monitor chemical reaction or biological dynamics in a convenient way.[23-25] The general underlying principle for these fluorescent indicators involves tautomerization to structures that differ significantly from that of the reactant prior to photoexcitation and is accompanied frequently by a sizeable Stokes shift and quenching of fluorescence. Excited-state proton transfer (ESPT) has been extensively studied in recent years, and it has been demonstrated that fluoreophore structure will have a noticeable impact on the ESPT dynamics and indicator performance.[26-34] Depending on the structures of the molecules and means of proton migration, ESPT can be classified into two categories: intra or intermolecular proton transfer.[35,36] The former has been observed in systems such as 3-hydroxyflavone,[37] 2-hydroxybenzaldehyde,[38] and 2-(2'-hydroxy-)benzothiazole,[39] and generally involves the formation of an intramolecular hydrogen bond between a hydroxyl or amino hydrogen (donor) and a proton acceptor like a carbonyl or azo group; photo excitation induces the instantaneous enhancement of acidity and basicity within the chromophore, serving as the driving force for ESPT.[40,41] In the latter, ESPT is facilitated by the formation of intermolecular hydrogen bonded donor-acceptor bridges in polar protic solvent environments, or dimerization; proton migration occurs by a series of proton transfer steps along the bridging network.[31,42] Such reactions have been observed with 7-azaindole,[43] 2-(2'-pyridyl)indole,[44] 1H-pyrrolo[3,2-*h*]quinolone,[45] etc.

Therefore, the possibility for ESPT is a critical consideration in the design of fluorescent sensors[46] and light-emitting materials.[26,27,47] Intramolecular tautomerizations are in particular of interest since it can be more readily controlled within a single molecule. Novel systems that exhibit photoinduced taotomerization attract significant attention to investigate. Herein we characterized the excited-state dynamics of a series of 6-amino-8-cyanobenzo[1,2-*b*]indolizine (bi), one of which involves photo-induced [1,3] effective H transfer.

Recently bi compounds with various substituents have been synthesized, and tested as fluorescent indicators, shown in Figure 1.3. We demonstrate that the pH-dependent shift is attributable to C-protonation of the heterocycle, thereby causing a break in conjugation and a blue-shift in emission. Additionally, unlike the increased fluorescence intensity seen for protonated bi with electron withdrawing or mild donating substitutions, titration of methoxylated analogue with trifluoroacetic acid (TFA) resulted in a sharp decrease in the fluorescence intensity with no blue shift. The exceptional observation regarding fluorescence quenching in the methoxylated compound is ascribed to an excited-state [1,3] H shift based on results of TAS and quantum chemical studies. We hypothesis that the substitution group has a non-trivial influence over the excited-state [1,3] H shift barrier, as summarized in a Jablonski diagram (Figure 1.4). Hence, chemical interactions that regulate this H shift could be used to facilitate binding- or surface-specific acid-responsive sensing.

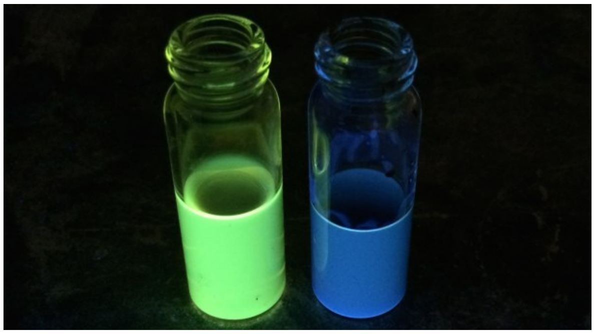

Figure 1.3. Observed blue shift in emission upon protonation of 2-methyl-6-amino-8-cyanobenzo[1,2-b]indolizine

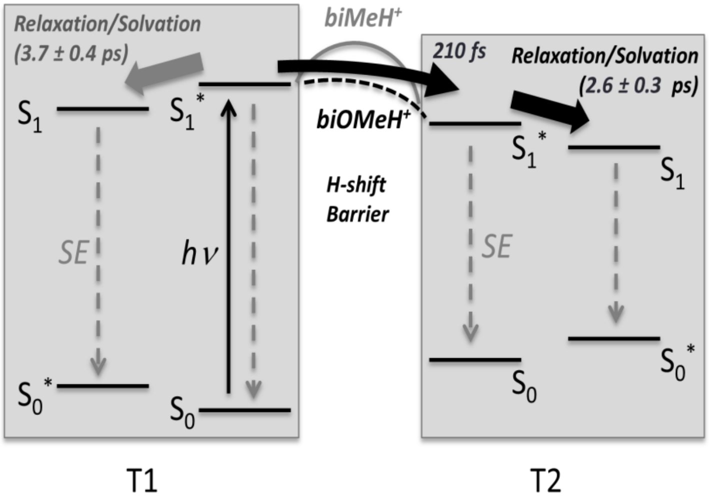
Relaxation/Solvation
(3.7 ± 0.4 ps)
S_1
S_1^*
SE
$h\nu$
S_0^*
S_0
biMeH$^+$
biOMeH$^+$
H-shift Barrier
210 fs
Relaxation/Solvation
(2.6 ± 0.3 ps)
S_1^*
S_1
SE
S_0
S_0^*
T1
T2

Figure 1.4. Jablonski diagram outlining the photophysical relaxation mechanisms of protonated methylated (biMeH$^+$) and methoxylated (biOMeH$^+$) bi compounds

1.2 Femtosecond transient absorption spectroscopy (TAS)

There are three kinds of signal in TAS: ground-state bleach, stimulated emission and excited-state absorption (Figure 1.5). Since the actinic pulse promotes a fraction of ground state molecules to the excited state, the ground state absorption will decrease, leading to a bleach in the ground state absorption region (purple line in Figure 1.5).

Stimulated emission occurs when a photon from the white light induces the emission of another photon from the excited state back to ground state. Its spectral profile has a similar shape to the fluorescence spectrum of the excited chromophore, especially at long time delays when the molecule is entirely relaxed (red line in Figure 1.5). Both the ground-state bleach and stimulated emission increase the light intensity to the camera, resulting in negative change in sample absorbance at relevant wavelengths. For the study of conjugated systems, we are particularly interested in its excited-state absorption signals (blue line in Figure 1.5), which reflect optically allowed transitions from the excited states prepared by the actinic pump, to higher excited states. From ΔA (Δt, λ), we can characterize the excited state lifetime and the relaxation evolution.

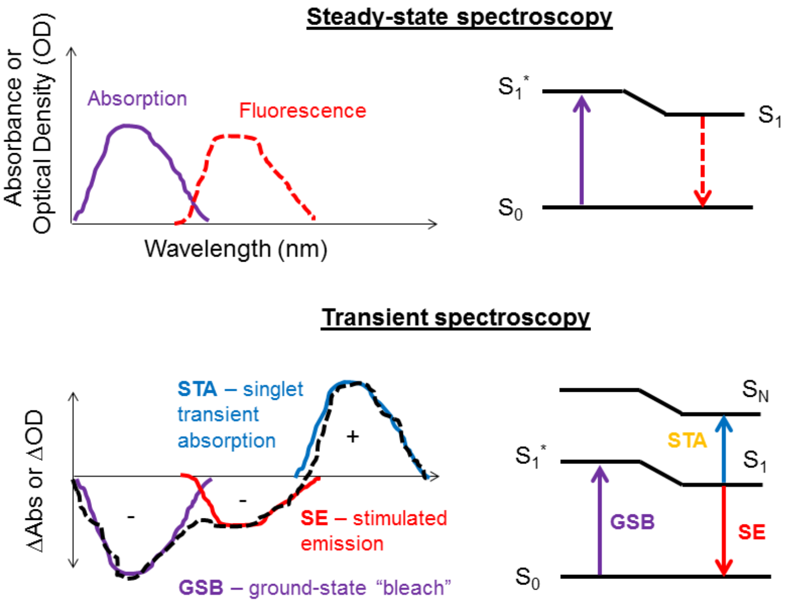
Steady-state spectroscopy
Absorbance or Optical Density (OD)
Absorption
Fluorescence
Wavelength (nm)
S_1^*
S_1
S_0
Transient spectroscopy
ΔAbs or ΔOD
STA – singlet transient absorption
+
-
-
SE – stimulated emission
GSB – ground-state "bleach"
S_N
S_1^*
STA
S_1
GSB
SE
S_0

Figure 1.5. Comparison between steady-state and transient spectroscopies

Fs-TAS requires two pulses, i.e. actinic pump and white light probe, to realize the measurement.[48] Their pulse width is on the order of tens of fs to achieve the fs time resolution. The function of the actinic pump is to promote a fraction of molecules in the sample to an electronically excited state. After a certain time delay Δt, a continuum white light probe pulse, whose intensity is so weak that it will not affect the excited-state population, is sent through the sample and dispersed by a spectrograph onto a CCD camera or photodiode array. Experimentally, these pulses are derived from the fundamental output of an amplified Ti:Sapphire laser. The actinic pump (green line in Figure 1.6) is generated through an optical parameteric amplifier (Coherent OperaSolo). For 400-nm actinic pump we directly double the fundamental pulse by passing it through a barium borate (BBO) crystal. As for white light probe (yellow line in Figure 1.6), roughly 80 μJ of the fundamental pulse (red line in Figure 1.6) was focused into a 2-mm-thick sapphire or CaF_2 crystal. Typically white light generated from CaF_2 can reach wavelengths below 400 nm. Δt can be controlled exactly by changing the difference in optical path length between actinic pump and white light probe. A chopper is used to periodically block the actinic pump and the absorbance difference, ΔA, is calculated by comparing the spectrum of the probe continuum measured with and without the pump present.

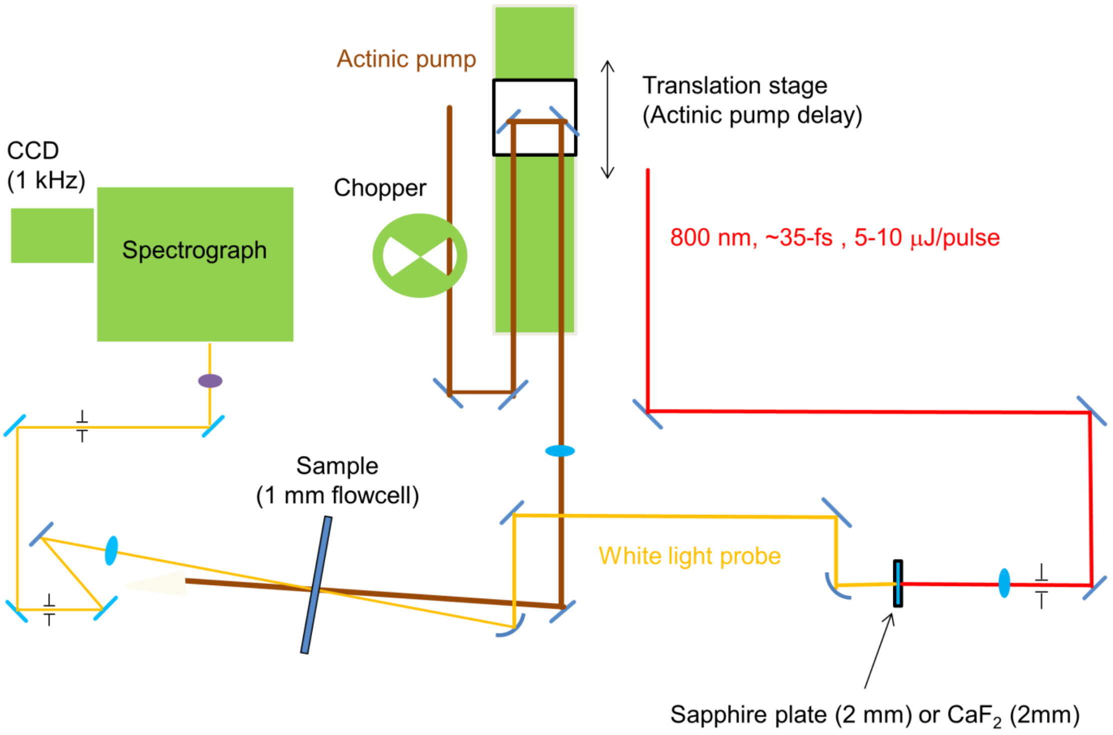
Actinic pump
Translation stage
(Actinic pump delay)
CCD
(1 kHz)
Spectrograph
Chopper
800 nm, ~35-fs , 5-10 μJ/pulse
Sample
(1 mm flowcell)
White light probe
Sapphire plate (2 mm) or CaF$_2$ (2mm)

Figure 1.6. Layout for the transient absorption spectroscopy (TAS) set up

However, it is common that TAS has several broad features that overlap significantly. As a result, it is not straightforward to distinguish and assign these to different excited states. What's more, TAS contains limited explicit information about the structural characteristics of the conjugated molecule, which is essential to interpret nuclear relaxation mechanisms.

1.3 Femtosecond stimulated Raman spectroscopy (FSRS)

Raman spectroscopy has been used routinely to probe the vibrational spectroscopy of molecules since it was discovered in 1920s, and particularly after the advent of lasers.[49,50] Being one of the only two vibrational spectroscopies, Raman can yield complementary information in regard to its counterpart, infrared absorption spectroscopy, and is particularly well-suited for the study of conjugated systems that lack intensely IR-active vibrational modes. Time-resolved resonance Raman spectroscopy has also been developed to reveal the structural characteristics of the excited state evolution ultrafast time scales.[51,52] However, techniques involving *spontaneous* Raman scattering usually suffer from high fluorescence background and low signal-to-noise ratio problems. These challenges can be circumvented by *stimulated* Raman spectroscopy, which is a coherent 4-wave mixing technique.[53-55]

In a pump-probe FSRS experiment three laser pulses are required, i.e. actinic pump and Raman probe, which are the same as used in TAS, and an additional Raman pulse, which is a narrow-bandwidth, temporally broad (about 2-3 ps) pulse (Figure 1.7). For the Raman pump pulse, we use a second-harmonic bandwidth compressor (SHBC, Light Conversion) to generate narrowband (~10 cm^{-1}) pulses with 2-3 ps duration at 400 nm. Specifically, the original 800-nm input pulse is equally split and linearly chirped with opposite temporal direction. Then these two pulses are used together to drive sum-frequency generation (SFG) in a BBO crystal; the complementary counter-chirping of these two pulses results in appropriate time and frequency conditions for generating a picosecond pulse at 400 nm by SFG. The resultant 400-nm pulse is used to pump a white-light-seeded OPA (TOPAS-400, Light Conversion) to obtain the wavelength-tunable Raman pump pulse through a three-stage nonlinear amplification process. Similar to TAS, the sample is first excited by the actinic pump. After a time delay Δt, the Raman pump and probe pulses will drive stimulated Raman transitions (Figure 1.8). This pair of pulses establishes a coherence of Raman-active vibrations on the excited state.[53-55] Since the Raman pump is broad in time, the vibrational coherence interacts with the Raman pump again, which leads to a photon emission with the same direction as the Raman probe. This enables the possibility to substantially increase collection efficiency and reject the fluorescence as well as the laser scatter at the same time.[53-55] The broad bandwidth of the probe pulse can simultaneously sample the Raman activate modes over several hundred to a few thousand cm^{-1}, which decay with the characteristic vibrational dephasing time. Additional experimental advantages of FSRS lies at its compatibility with broadband TAS, thus it is convenient to run both experiments under the same condition simultaneously. By blocking the Raman pump at the half the laser repetition rate, we are able to acquire FSRS spectra by comparing the consecutive detected broadband probe pulses. A experimenetal layout for FSRS is provived in Figure 1.9.

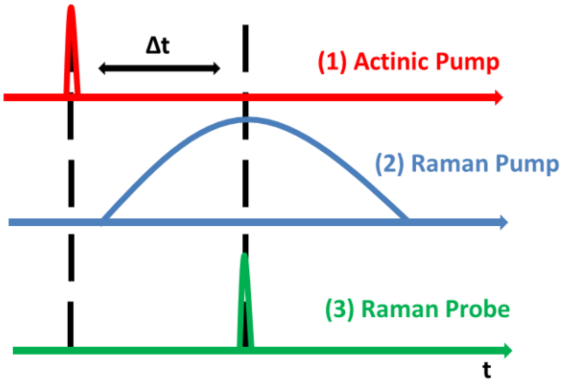

Figure 1.7. Pulse sequence and timing in FSRS

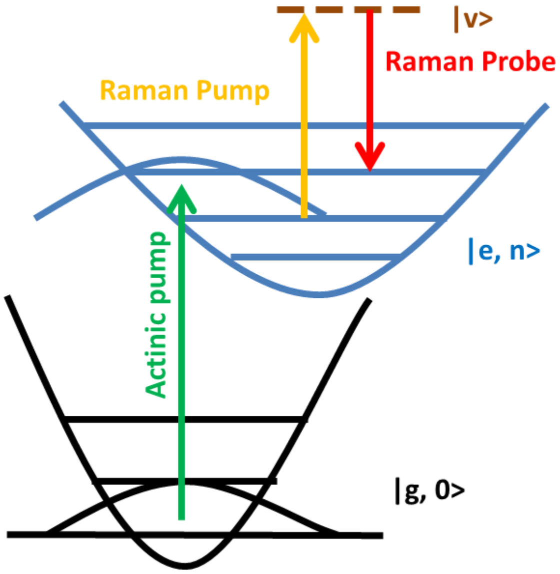
|v>
Raman Probe
Raman Pump
|e, n>
Actinic pump
|g, 0>

Figure 1.8. Schematic representation of the energy diagram for a time-resolved FSRS experiment

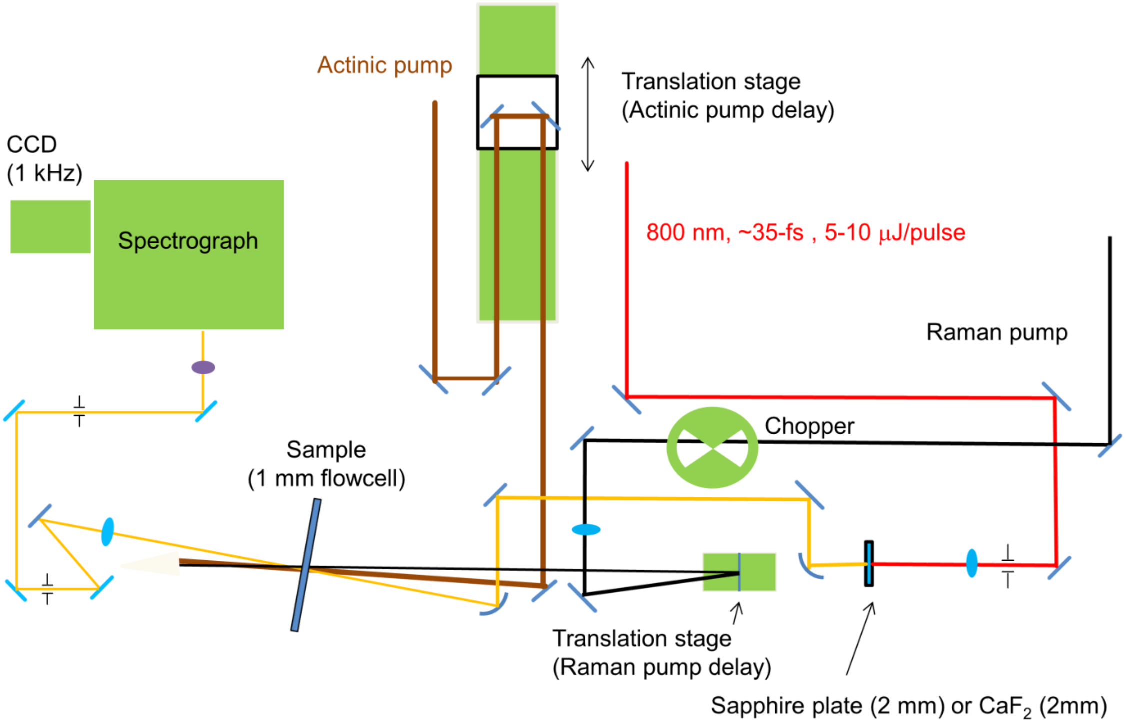
Actinic pump
Translation stage
(Actinic pump delay)
CCD
(1 kHz)
Spectrograph
800 nm, ~35-fs , 5-10 μJ/pulse
Raman pump
Chopper
Sample
(1 mm flowcell)
Translation stage
(Raman pump delay)
Sapphire plate (2 mm) or CaF2 (2mm)

Figure 1.9. Layout for the femtosecond stimulated Raman spectroscopy set up

As for traditional Raman, FSRS signal can be significantly enhanced under resonant conditions. The Raman transition polarizability is governed by the Kramers-Heisenberg- Dirac (KHD) equation:[56]

$$(\alpha_{\rho\sigma})_{\mathrm{if}} = \frac{1}{\hbar}\sum_{n}[\frac{<i|\mu_\rho|n><n|\mu_\sigma|f>}{\omega_0+\omega_{\mathrm{nf}}} - \frac{<i|\mu_\sigma|n><n|\mu_\rho|f>}{\omega_0-\omega_{\mathrm{ni}}}] \tag{1.1}$$

$(\alpha_{\rho\sigma})_{\mathrm{if}}$ is an element of the transition polarizability tensor, where ρ and σ are Cartesian directions. The intensity of the transition $i \to f$ is proportional to the square of the amplitude of$(\alpha_{\rho\sigma})_{\mathrm{if}}$. We can neglect the anti-resonance term when ω_0 is close to the allowed electronic transition ω_{eg}. Keeping the expansion of $< i\left|\mu_\rho\right|n >$ to its first order the Raman transition polarizability can be expressed as Albrecht A and B terms:

$$(\alpha_{\rho\sigma})_{v'v''} = A_{v'v''} + B_{v'v''}$$

The A term dominates $(\alpha_{\rho\sigma})_{v'v''}$ under resonant conditions and comes from the Condon approximation:[56]

$$A_{v'v''} = \frac{1}{\hbar}\sum_v \left(\mu_{ge}^0\right)_\rho \left(\mu_{ge}^0\right)_\sigma \left[\frac{\langle v'|v\rangle\langle v|v''\rangle}{\omega_{ev,gv'}-\omega_0-i\Gamma_{\mathrm{e}}}\right] \tag{1.2}$$

It leads to intensity enhancement when the incident frequencies are close to an allowed transition frequency $\omega_{ev,gv'}$. The enhancement factors relative to off-resonance Raman usually achieve 10^5 to 10^6, but it only applies to the totally symmetric modes, provided that there is no substantial symmetry change to the molecular geometry between the excited states. The transition selection rule is Δv = integer.[56]

Through resonantly enhanced Raman spectroscopy not only can we detect the overall population of transient states, but also we can also observe structural evolution in these excited states from evolution in the in frequencies of vibrational features with time. Furthermore, we can use Raman measurements to track formation of charge-separated states initiated by photoexcitation of donor-acceptor system, since vibrational spectroscopies are sensitive to large changes in charge distribution.[57,58] Therefore, TAS and FSRS are an ideal combination of methods to interrogate the photoresponses of conjugated molecular materials.

1.4. References

(1) Facchetti, A. *Chem. Mater* **2011**, *23*, 733.

(2) Gunes, S.; Neugebauer, H.; Sariciftci, N. S. *Chem. Rev.* **2007**, *107*, 1324.

(3) Beenken, W. J.; Pullerits, T. *J. Phys. Chem. B* **2004**, *108*, 6164.

(4) Yaliraki, S. N.; Silbey, R. J. *J. Chem. Phys.* **1996**, *104*, 1245.

(5) Lanzani, G.; Nisoli, M.; Magni, V.; De Silvestri, S.; Barbarella, G.; Zambianchi, M.; Tubino, R. *Phys. Rev. B* **1995**, *51*, 13770−13773.

(6) Lanzani, G.; Nisoli, M.; Silvestri, S. D.; Tubino, R. *Synth. Met.* **1996**, *76*, 39−41.

(7) Paa, W.; Yang, J. P.; Rentsch, S. *Appl. Phys. B* **2000**, *71*, 443−449.

(8) Kölle, P.; Schnappinger, T.; Vivie-Riedle, R. d. *Phys. Chem. Chem. Phys.* **2016**, *18*, 7903.

(9) Castiglioni, C.; Zoppo, M. D.; Zerbi, G. *J. Raman Spectrosc.* **1993**, *24*, 485.

(10) Hernandez, V.; Castiglioni, C.; Zoppo, M. D.; Zerbi, G. *Phys. Rev. B* **1994**, *50*, 9815.

(11) Kamiya, Y.; Asanuma, H. *Acc. Chem. Res.* **2014**, *47*, 1663.

(12) Szymański, W.; Beierle, J. M.; Kistemaker, H. A. V.; Velema, W. A.; Feringa, B. L. *Chem. Rev.* **2013**, *113*, 6114.

(13) Samanta, S.; Beharry, A. A.; Sadovski, O.; McCormick, T. M.; Babalhavaeji, A.; Tropepe, V.; Woolley, G. A. *J. Am. Chem. Soc.* **2013**, *135*, 9777.

(14) Rau, H. *J. Photochem.* **1984**, *26*, 221.

(15) Klausen, R. S.; Widawsky, J. R.; Steigerwald, M. L.; Venkataraman, L.; Nuckolls, C. *J. Am. Chem. Soc.* **2012**, *134*, 4541−4544.

(16) Su, T. A.; Li, H.; Klausen, R. S.; Widawsky, J. R.; Batra, A.; Steigerwald, M. L.; Venkataraman, L.; Nuckolls, C. *J. Am. Chem. Soc.* **2016**, *138*, 7791.

(17) Su, T. A.; Li, H.; Steigerwald, M. L.; Venkataraman, L.; Nuckolls, C. *Nat. Chem.* **2015**, *7*, 215.

(18) Surampudi, S.; Yeh, M. L.; Hardigree, J. F. M.; Siegler, M. A.; Kasl, T. A.; Katz, H. E.; Klausen, R. S. *Chem. Sci.* **2015**, *6*, 1905−1909.

(19) Sun, Y. P.; Hamada, Y.; Huang, L. M.; Maxka, J.; Hsiao, J. S.; West, R.; Michl, J. *J. Am. Chem. Soc.* **1992**, *114*, 6301.

(20) Sun, Y. P.; Michl, J. *J. Am. Chem. Soc.* **1992**, *114*, 8186.

(21) Sakurai, H.; Kira, M.; Uchida, T. *J. Am. Chem. Soc.* **1973**, *95*, 6826.

(22) Traven, V. F.; West, R. *J. Am. Chem. Soc.* **1973**, *95*, 6824.

(23) Jung, H. S.; Chen, X.; Kim, J. S.; Yoon, J. *Chem. Soc. Rev.* **2013**, *42*, 6019.

(24) Li, H.; Fan, J.; Peng, X. *Chem. Soc. Rev.* **2013**, *42*, 7943.

(25) Guo, Z.; Park, S.; Yoon, J.; Shin, I. *Chem. Soc. Rev.* **2014**, *43*, 16.

(26) Kwon, J. E.; Park, S. Y. *Adv. Mater.* **2011**, *23*, 3615.

(27) Zhao, J.; Ji, S.; Chen, Y.; Guo, H.; Yang, P. *Phys. Chem. Chem. Phys.* **2012**, *14*, 8803.

(28) Wu, J.; Liu, W.; Ge, J.; Zhang, H.; Wang, P. *Chem. Soc. Rev.* **2011**, *40*, 3483.

(29) Corani, A.; Pezzella, A.; Pascher, T.; Gustavsson, T.; Markovitsi, D.; Huijser, A.; d'Ischia, M.; Sundstrom, V. *J. Phys. Chem. Lett.* **2013**, *4*, 1383.

(30) van Oort, B.; ter Veer, M. J.; Groot, M. L.; van Stokkum, I. H. *Phys. Chem. Chem. Phys.* **2012**, *14*, 8852.

(31) Waluk, J. *Acc. Chem. Res.* **2003**, *36*, 832.

(32) Waluk, J. *Acc. Chem. Res.* **2006**, *39*, 945.

(33) Goodman, M. F. *Nature* **1995**, *378*, 237.

(34) Douhal, A.; Kim, S. K.; Zewail, A. H. *Nature* **1995**, *378*, 260.

(35) Demchenko, A. P.; Tang, K. C.; Chou, P. T. *Chem. Soc. Rev.* **2013**, *42*, 1379.

(36) Hsien, C.-C.; Jiang, C.-M.; Chou, P.-T. *Acc. Chem. Res.* **2010**, *43*, 1364.

(37) McMorrow, D.; Kasha, M. *J. Phys. Chem.* **1984**, *88*, 2235.

(38) Nagaoka, S.; Hirota, N.; Sumitani, M.; Yoshihara, K. *J. Am. Chem. Soc.* **1983**, *105*, 4220.

(39) Frey, W.; Laermer, F.; Elsaesser, T. *J. Phys. Chem.* **1991**, *95*, 10391.

(40) Tseng, H.-W.; Lin, T.-C.; Chen, C.-L.; Lin, T.-C.; Chen, Y.-A.; Liu, J.-Q.; Hung, C.-H.; Chao, C.-M.; Liu, K.-M.; Chou, P.-T. *Chem. Commun.* **2015**, *51*, 16099.

(41) Tseng, H. W.; Liu, J. Q.; Chen, Y. A.; Chao, C. M.; Liu, K. M.; Chen, C. L.; Lin, T. C.; Hung, C. H.; Chou, Y. L.; Wang, T. L.; Chou, P. T. *J. Phys. Chem. Lett.* **2015**, *6*, 1477.

(42) Vetokhina, V.; Dobek, K.; Kijak, M.; Kaminska, I. I.; Muller, K.; Thiel, W. R.; Waluk, J.; Herbich, J. *ChemPhysChem* **2012**, *13*, 3661.

(43) InghamC., K.; El-Bayoumi, M. A. *J. Am. Chem. Soc.* **1973**, *96*, 1674.

(44) Nosenko, Y.; Wiosna-Salyga, G.; Kunitski, M.; Petkova, I.; Singh, A.; Buma, W. J.; Thummel, R. P.; Brutschy, B.; Waluk, J. *Angew. Chem. Int. Ed.* **2008**, *47*, 6037.

(45) Nosenko, Y.; Kunitski, M.; Thummel, R. P.; Kyrychenko, A.; Herbich, J.; Waluk, J.; Riehn, C.; Brutschy, B. *J. Am. Chem. Soc.* **2006**, *128*, 10000.

(46) Suzuki, N.; Fukazawa, A.; Nagura, K.; Saito, S.; Kitoh-Nishioka, H.; Yokogawa, D.; Irle, S.; Yamaguchi, S. *Angew. Chem. Int. Ed.* **2014**, *53*, 8231.

(47) Park, S.; Kwon, J. E.; Kim, S. H.; Seo, J.; Chung, K.; Park, S.-Y.; Jang, D.-J.; Medina, B. M.; Gierschner, J.; Park, S. Y. *J. Am. Chem. Soc.* **2009**, 14043.

(48) Ruckebusch, C.; Sliwaa, M.; Pernot, P.; Juanc, A. d.; Tauler, R. *J. Photochem. Photobiol. C* **2012**, *13*, 1.

(49) Friesen, M.; Junker, M.; Zumbusch, A.; Schnöckel, H. *J. Chem. Phys.* **1999**, *111*, 7881.

(50) Edwards, H.; Chalmers, J. M. *Raman Spectroscopy in Archaeology and Art History*; Royal Society of Chemistry, Cambridge, UK, 2005.

(51) Bell, S. E. J. *Analyst* **1996**, *121*, 107R.

(52) K., S. S.; S., U.; W., P. A. *Appl. Spectrosc.* **2011**, *65*, 1087.

(53) Kukura, P.; McCamant, D. W.; Mathies, R. A. *Annu. Rev. Phys. Chem.* **2007**, *58*, 461.

(54) Dietze, D. R.; Mathies, R. A. *Chem. Phys. Chem.* **2016**, *17*, 1224.

(55) Frontiera, R. R.; Mathies, R. A. *Laser Photonics Rev.* **2011**, *5*, 102.

(56) McHale, J. L. *Molecular Spectroscopy*; Prentice-Hall Inc., Upper Saddle River, NJ, 1999.

(57) Rhinehart, J. M.; Mehlenbacher, R. D.; McCamant, D. *J. Phys. Chem. B* **2010**, *114*, 14646.

(58) Brown, K. E.; Veldkamp, B. S.; Co, D. T.; Wasielewski, M. R. *J. Phys. Chem. Lett.* **2012**, *3*, 2362.

Chapter 2: Structural Relaxation of Photoexcited Quaterthiophenes Probed with Vibrational Specificity

This chapter is based on the following publication:

1. Zhou, J.; Yu, W.; Bragg, A. E., "Structural Relaxation of Photoexcited Quaterthiophenes Probed with Vibrational Specificity." *J. Phys. Chem. Lett.* **2015,** *6,* 3496-3502.

2.1. Introduction

There is continuing interest in the photophysical properties of conjugated oligomers and polymers, as there are significant processing advantages for using these materials to manufacture organic optoelectronic devices, including organic photovoltaics and light-emitting diodes.[1,2] The photophysics of conjugated polymers in particular are complicated by the heterogeneities along and between extended π-conjugated structures that control the nature and dynamics of transient states in polymer and material environments. [3-13] Given the significant structural heterogeneity present in conjugated polymers, probing the structural dynamics of oligomers can provide valuable insights on relaxation dynamics relevant to localization and relaxation of excited states of conjugated polymers.[8,14-17] However, spectroscopic signatures capable of revealing explicit detail at the structural level are critical and must be identified. In this work, we demonstrate the use of ultrafast excited-state Raman spectroscopy as a tool for interrogating conformational changes induced by photoexcitation of conjugated oligomers with mode-specific sensitivity.

Numerous studies have interrogated the relaxation dynamics of photoexcited, conjugated oligomers using time-resolved electronic spectroscopies.[8,14-18] This prior work generally relied on dynamic spectral shifts of electronic transitions to deduce relaxation timescales and mechanisms induced by photoexcitation.[14,16,17] An implicit (and reasonable) assumption is that the Stokes shift in the fluorescence and stimulated emission (and also shifts in excited-state absorption) reflects vibrational and torsional relaxation that ultimately yields a planar, quinoidal excited-state geometry. Collectively, this prior work reported that the timescales for vibrational relaxation and structural evolution in photoexcited oligothiophenes occurs on sub-ps to ps timescales.[14-18] However, transient electronic spectroscopies provide limited explicit structural information about evolving excited-state structures.

In contrast, time-resolved spectroscopy at the vibrational level can serve as a highly sensitive probe of evolution in molecular conformation. Time-resolved Raman spectroscopy with resonant enhancement is a highly suitable method for interrogating the conformational dynamics of excited conjugated materials with vibrational sensitivity:[13, 3,19] not only does resonant enhancement increase Raman cross-sections significantly, resonant Raman spectra are dominated by activity along nuclear coordinates that coincide with the primary structural differences between electronic states; for oligothiophenes this involves differences between nominal benzoidal and quinoidal structures.[20,21] Additionally, Raman frequencies of C=C stretches in conjugated oligomers are known to be highly sensitive to the degree of electron delocalization along the conjugated backbone.[20-22] Time-Resolved Resonance Raman spectroscopy (TR^3) has been used previously to study dynamics of conjugated oligomeric systems,[19,23] but notably with coupled time and frequency resolution that obscures observation of critical structural changes on ultrafast (< 2-5ps) timescales.[24] In this work we use resonantly enhanced femtosecond stimulated Raman spectroscopy (FSRS)[25,26] in order to observe ultrafast spectral relaxation of Raman features that is associated with photoinduced conformation dynamics of oligothiophenes.

2.2. Experimental materials

3,3‴-dihexyl-2,2′:5′,2″:5″,2‴–quaterthiophene (DH4T) and chlorobenzene (CB), spectroscopic grade, were purchased from Sigma Aldrich. 2,2′:5′,2″:5″,2‴-quaterthiophene (4T) was purchased from TCI AMERICA. Purities of both samples were checked by mass spectrometry. All materials were used without further purification. CB was deaerated via repeated freeze-pump-thaw cycles prior to preparing sample solutions. 4T and DH4T were dissolved in CB under air-free conditions at a concentration of ~2.0×10^{-3} mol/L, resulting in an optical density of ~1.0 at the peak wavelength of absorption for each sample. Sample solutions were circulated through a 1 mm path-length quartz flow cell via a N_2-purge flow loop for optical measurements.

FSRS and TAS measurements were performed using a set-up described previously.[3,4] Actinic pump pulses at 350 nm, used to prepare molecular excited states, were attenuated to 3 μJ/pulse; Raman excitation pulses at 850 or 880 nm were typically 5-10 μJ/pulse. Both pump pulses were focused to a 500 μm beam diameter on the flow cell. The white-light probe pulse had a diameter of 50 μm in the laser interaction region of the sample. The effective time resolution for these experiments was measured as 190 fs. More detailed description of the experimental setup as well as the data collection and analysis procedures for FSRS measurements can be found in supporting material.

2.3. Computational methods

DFT calculations utilized the 6-31G(d) basis set along with the range-corrected CAM-B3LYP density functional. The range-corrected functional CAM-B3LYP with varying amounts of HF exchange can estimate π-delocalization in oligothiophenes more precisely, and improve descriptions of their molecular polarizabilities, hyperpolarizabilities, and Raman spectroscopy.[22] All excited-state calculations were performed using time-dependent density functional theory (TDDFT). To reduce the computational expense, we evaluated the molecular structure of 3,3‴-diethyl-2,2′:5′,2″:5″,2‴−quaterthiophene (DE4T), since the replacement of hexyl with ethyl groups along the oligothiophene backbone does not lead to a substantial disparity in the geometry of the ground (S_0) state.[22] Geometry optimizations of 4T and DE4T in the S_0 or S_1 states were determined without symmetry constraints in Gaussian 09.[27] Mode assignments of features in the ER spectra were inferred from comparisons to Raman spectra of the ground state and the calculated excited-state Raman spectra of bithiophene (2T). No scaling factors were applied to the excited-state Raman frequencies, since we are predominantly interested in the relative positions and intensities of peaks as a function of molecular geometry.

ER spectra of 2T were calculated using QChem 4.2[28] at various excited-state configurations obtained by scanning the central torsional dihedral angle, θ; the Hessian was computed by numerical differentiation of the TDDFT analytical gradients obtained for each geometry. Calculations were performed as follows: We first obtained a planar 2T geometry through optimization of the first excited state. We then scanned θ between 10 to

40 degrees, while all other geometrical parameters were adopted from planar 2T without further optimizations, due to computational expense.

2.4. Results and discussion

Here we have examined specifically the excited-state spectroscopy of 2,2′:5′,2″:5″,2‴−quaterthiophene (4T) and 3,3‴-dihexyl-2,2′:5′,2″:5″,2‴−quaterthiophene (DH4T) in solutions of chlorobenzene in order to elucidate the structural relaxation dynamics of photoexcited oligothiophenes with sensitivity at the vibrational level. Studies with both 4T and its alkyl-substituted analog enable us to explore how structural modifications that alter the equilibrium molecular geometry and shapes of excited-state potential-energy surfaces impact excited-state spectroscopy and dynamics of oligomers.

The chemical structures of 4T and DH4T are given in Scheme 2.1. The steady-state absorption spectra of DH4T and 4T peak at 382 and 395 nm (Figure 2.1S), respectively, indicating that 4T exhibits greater π-delocalization than DH4T in the ground state.[14 29] Disparities in the ground-state geometries of these two molecules are revealed through DFT computations with 4T and the diethyl analog of DH4T (i.e. DE4T): the central and terminal interring dihedral angles are 24° and 45° in DE4T, 19° and 24° in 4T, respectively (see Figures 2.2S and 2.3S – both oligomers exhibit nonplanar all “S trans” minimum-energy structures). These differences in structure and π-delocalization can be attributed to steric interactions between the pendant hexyl chains and adjacent thiophene monomers that yield a more nonplanar structure for the alkyl-substituted 4T structure.

By contrast, the optimized structures of both DE4T and 4T at the S_1 minimum are planar (see Figures 2.4S and 2.5S), and the fluorescence spectra of the two isomers are highly similar (Figure 2.1S). Hence, we expect that DH4T must undergo a more dramatic structural evolution than 4T in its relaxation from the Franck-Condon region to the minimum of its excited-state potential-energy surface.

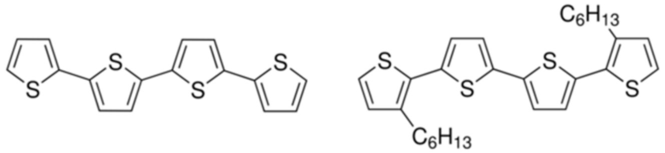

4T **DH4T**

Scheme 2.1. The structures of 2,2′:5′,2″:5″,2‴−quaterthiophene (4T) and 3,3‴-Dihexyl-2,2′:5′,2″:5″,2‴−quaterthiophene (DH4T) .

Transient absorption spectroscopy reveals comparable excited-state spectral features and dynamics for these oligomers following excitation at 350 nm (Figure 2.8S): a negative band below 550 nm can be ascribed to stimulated emission (SE) from the S_1 state, while the broad positive band extending from 550 nm into the near IR is assigned to absorption of the lowest-lying singlet state (singlet transient absorption, or STA). For both molecules, a redshift in the SE region is observed within the first 2 ps after excitation (shift timescales of 0.56 ± 0.16 ps and 1.09 ± 0.17 ps for 4T and DH4T, respectively; see Figure 2.10S), which is consistent with findings from previous studies of the transient electronic absorption spectroscopy of quaterthiophene and its derivatives.[14] Excited-state decay occurs primarily via radiative decay and intersystem crossing into the triplet manifold; the latter is evident from the appearance of triplet transient absorption (TTA) at late delays (~1 ns, Figure 2.8S(b)). The S_1 lifetime is determined to be 350 and 470 ps for DH4T and 4T, respectively.[30] In total, time-resolved

TAS presents rather similar transient spectral features and dynamics for both DH4T and 4T (Figures 2.9S and 2.10S), yet provides little explicit detail regarding the structural evolution of the excited states of either system.

Figures 2.1(a) and 2.1(b) present time-resolved FSRS spectra of 4T and DH4T after excitation at 350 nm. The Raman spectra of 4T and DH4T collected 2 ps after photoexcitation at 350 nm to their S_1 states are plotted in Figure 2.1(c). The Raman-excitation wavelength was chosen as 850 nm for 4T and 880 nm for DH4T, as these are resonant with the red edges of STA features. The FSRS spectrum of each photoexcited molecule exhibits three distinct excited-state features. Nominal feature assignments for the 4T and DH4T spectra can be made through comparisons to ground-state spectra of the oligomers: The feature near 1419 cm^{-1} can be ascribed to the intra-ring C=C in-phase stretching (Я).[3, 4, 29-31] The intra-ring C=C out-of-phase stretching (Z) lies at slightly higher frequency around 1528 cm^{-1}.[3,4,31-33] Finally, the feature at 669-675 cm^{-1} is attributed to the C-S-C ring deformation vibration.[19,32,33] These nominal assignments are supported through agreement with the calculated excited-state spectrum for bithiophene (2T) (see Figure 2.7S(a)). Calculated nuclear displacements of these excited-state Raman-active modes for 2T, 4T, and DE4T reveal that these vibrations involve significant contributions from in-plane CH bending motions (Figure 2.6S); this is also true for the most intense Raman-active modes in the ground state, yet the ground-state modes exhibit greater C=C stretching amplitudes.

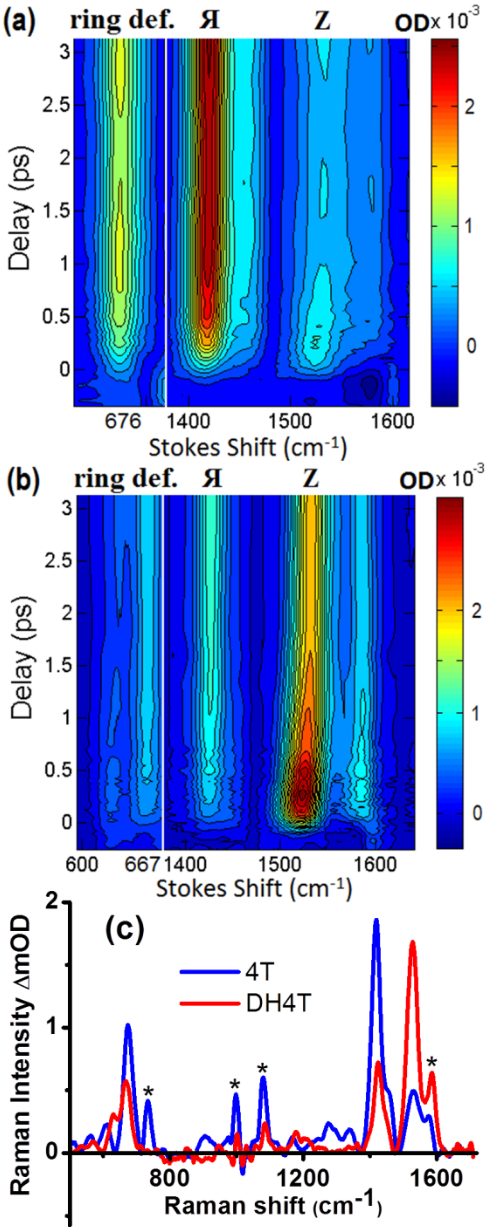

Figure 2.1. Time-dependence of three major FSRS features obtained from (a) 4T and (b) DH4T following photoexcitation at 350 nm. (c) The blue and red lines plot the FSRS spectra of photoexcited 4T and DH4T, respectively, obtained 2 ps after photoexcitation. Residual solvent signals are marked with asterisks.

The most noticeable difference between the excited-state Raman spectroscopy of 4T and DH4T involves the relative intensities of these various features. The relative intensity of the in- and out-of-phase stretching features switches upon substitution, as illustrated in Figure 2.1(c): the Я mode dominates the spectrum of 4T, whereas the Z mode dominates the spectrum of DH4T. However, the time-dependent intensities associated with all three features exhibit qualitatively similar behaviors for both oligomers. Figures 2.2(a) and 2.2(b) plot (normalized) time-dependent feature intensities for the two oligomers. For both oligomers the out-of-phase feature grows in on an instrument-limited timescale followed by a slightly slower rise to a peak intensity by 300fs; subsequently, Z-mode feature intensity decays on a timescale of a couple of picoseconds. In contrast, the appearance of the in-phase stretch and ring deformation features reflects an induction that continues onto the 1-2 picosecond timescale. These opposite time-dependent behaviors observed for these two features are most apparent for DH4T (Figures 2.1(b), 2.2(b)).

We find that one valuable metric for characterizing the progress of excited-state relaxation is the absolute intensity ratio of the intra-ring C=C out-of-phase and in-phase stretching features (ROI = R̲atio of O̲ut to I̲n). Previous studies with oligothiophenes in their ground states [3,22,31] have revealed that the ROI values are closely related to the interring dihedral angle, θ: this ratio is smaller for more planar relative to non-planar structures; correspondingly, oligomers and polymers that have significant interring steric interactions exhibit larger ROI values.[3,22] Figure 2.2(c) compares the ROI values obtained with photoexcited 4T and DH4T and shows that these both decrease with time. A single exponential fit to the ROI gives time constants of 0.40 ± 0.03 ps and 1.73 ± 0.14

ps, for 4T and DH4T, respectively. These constants are well outside of the instrument response of our measurements. Notably, this intensity ratio is always smaller for 4T relative to DH4T.

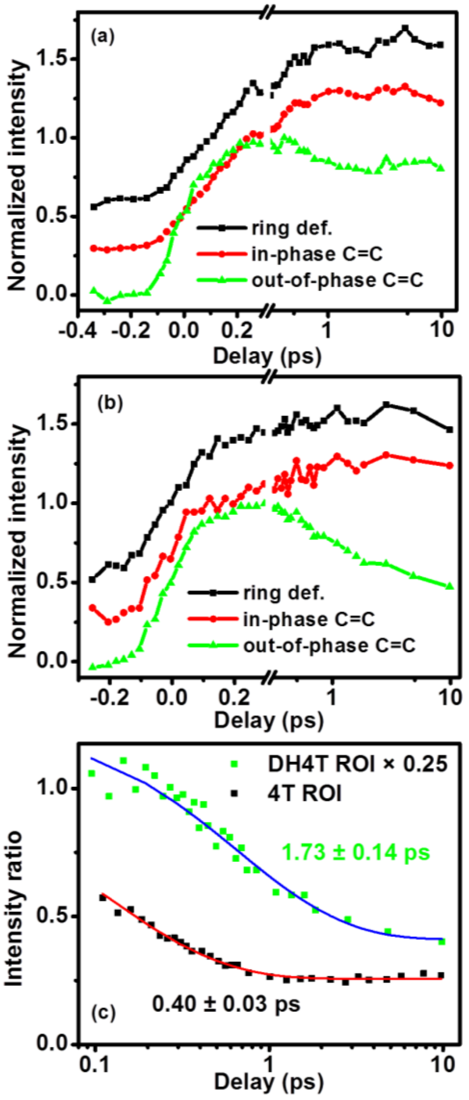

Figure 2.2. Normalized time-resolved intensities for ring deformation, in-phase C=C (Я) and out-of-phase C=C (Z) stretching modes of (a) 4T and (b) DH4T following photoexcitation at 350 nm. The C-S-C deformation and Я intensities are offset to those of Z for clarity. (c) Ratio of out-of-phase to in-phase feature intensities (ROI) for 4T and DH4T. The ROI for DH4T is multiplied by 0.25 for better visual comparison. Both curves are fit well with a single exponential function with timescale of 0.40 and 1.73 ps, for 4T and DH4T, respectively.

Another disparity between the time-resolved Raman spectra obtained with 4T and DH4T involves the degree and timescales of feature frequency shifts. The out-of-phase stretching mode for both 4T and DH4T exhibit noticeable blue shifts within 1-2 ps of photoexcitation (Figure 2.1(b)). A closer examination of the peak positions of all three features for both 4T and DH4T is provided in Figure 2.3. The ultrafast blue-shifting of the Z-mode feature can be fitted well with a single exponential function, yielding shifting time constants of 0.40 ± 0.03 ps and 0.86 ± 0.04 ps, for 4T and DH4T respectively. The net blue-shift of the Z mode is 6.2 cm^{-1} for 4T and 11.5 cm^{-1} for DH4T. The peak shifting and ROI relaxation timescales are in qualitative accord and are comparable to relaxation timescales obtained from shifts in stimulated emission bands[14] (see Figure 2.10S), indicating that all are manifestations of the same excited-state relaxation dynamics. Interestingly, the more twisted structure of DH4T exhibits more significant spectral blue-shifting for the out-of-phase feature. In contrast, peak shifts of the C-S-C deformation and Я features are relatively insignificant (Figure 2.3(b)), indicating that their positions are not strongly affected by photoinduced relaxation of the oligomers.

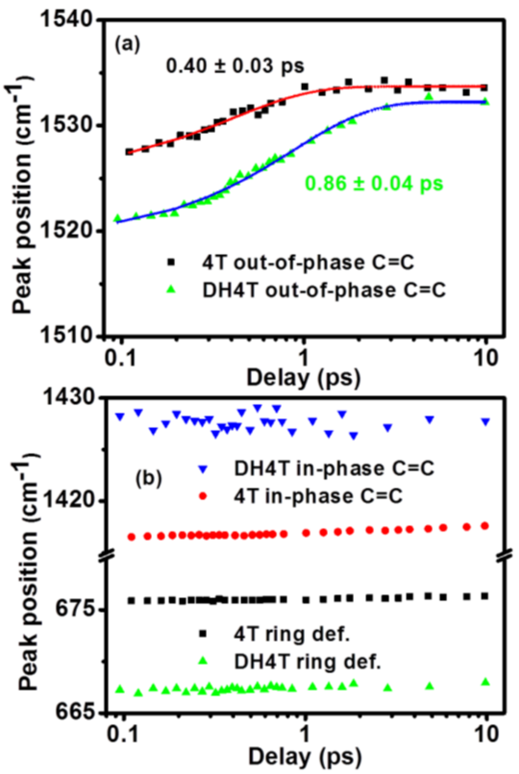

Figure 2.3. Comparisons of weighted peak positions of (a) out-of phase C=C (Z) and (b) in-phase C=C (Я) and ring deformation modes of 4T and DH4T excited at 350 nm. The blue shift of Z mode of both quaterthiophenes can be well fitted with a single exponential function with timescale of 0.40 and 0.86 ps, for 4T and DH4T, respectively.

In order to better understand how the observed variations in feature intensities and frequencies correlate with molecular structure and structural dynamics, we have calculated the vibrational frequencies of S_1 bithiophene (2T) at various configurations obtained by scanning the interring dihedral angle, θ. Raman-active modes were identified both from a calculation of the non-resonant Raman spectrum (Figure 2.7S(a)) and according to relative IR-activities of S_1 optimized 2T (Figure 2.6S). Our excited-state frequency calculations use 2T as a model for computational convenience; however, modes with similar character and negligible IR activity (and therefore high Raman activity) are found at similar frequencies for the optimized S_1 4T and DE4T structures

(Figure 2.6S). We note that calculations of accurate Raman intensities in excited states are not straightforward (both for non-resonant and resonant spectra) and push the limits of packaged computational resources even for a molecule such as 2T. We therefore focus here on the vibrational frequencies of relevant Raman active modes of excited states. Figure 2.4 illustrates the dependence of the Я and Z mode frequencies of S_1 2T with interring dihedral angles spanning 0 to 40° and shows that the Z-mode frequency is much more sensitive to structural changes than that of the Я mode: As θ is reduced from 40 to 0° there is a 16 cm^{-1} blue shift of the Z mode, but only a 3 cm^{-1} blue shift for the Я mode. These calculations therefore illustrate the correlation between the planarity of the conjugated backbone (as determined by the interring dihedral angle) and the frequencies of the Z and Я features.

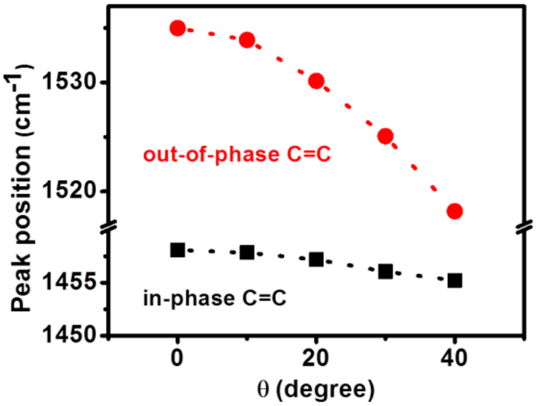

Figure 2.4. Calculated frequencies of the in-phase and out-of-phase C=C stretching modes of 2T as a function of torsional dihedral angle, θ.

The parametric dependence of the frequencies of these modes on the torsional dihedral reflects that evolution of these features provides a mode-specific probe of conformational relaxation of excited oligothiophenes. Thus, we ascribe the time-dependent evolution in the spectral dynamics and ROI observed for 4T and DH4T with evolution in the interring torsional dihedral that results from relaxation towards a planar excited-state conformation. As the inter-ring torsional dihedral is expected to be a highly fluxional in the ground state, we note that the excited-state structural evolution observed spectroscopically should be interpreted as an ensemble average with respect to the ground-state distribution of this coordinate.

We note that computation of the non-resonant Raman spectra in the same set of configurations exhibit trends in feature intensities with dihedral angle that are in qualitative accord with experimental observations: significant drop and slight increase in the Z and Я mode intensities with decreasing dihedral angle, respectively (Figure 2.7S(b)). This similarity is compelling, and warrants further careful computational characterization of the excited-state Raman spectroscopy of these systems. Accurate comparisons with experiment will also have to account for resonant enhancement.

The magnitude of the blue shift and evolution in the ROI associated with excited-state relaxation are more dramatic for DH4T relative to 4T; the corresponding timescales of these processes are likewise longer for DH4T. These differences are consistent with larger average torsional twists in the ground state and, therefore, Franck-Condon region of the excited state that is induced by the presence of the hexyl groups in DH4T. The slower rate for DH4T is also consistent with the anticipated impact of bulky, heavy hexyl groups on interring torsional twisting. Naturally, the absolute Raman frequencies and ROIs should differ between these two systems as a result of mechanical coupling to pendant hexyl groups. Given that both oligomers are predicted to have planar minimum energy structures in the excited state, the impact of coupling with the hexyl side-chains on the frequencies of these Raman-active modes is readily apparent at the latest delays plotted in Figure 2.3.

We note that an alternate explanation for the observed Z-mode blueshift would be a vibrational relaxation of this mode on an anharmonic potential. However, the fact that the blueshift of the Z feature is accompanied by negatively correlated changes in the Z and Я mode intensities strongly supports that these spectral dynamics reflect parametric variations in the character of these modes with interring torsional dihedral. We also presume that the presence of the hexyl substituents would enhance intramolecular vibrational energy transfer out of the intra-ring stretches, and thereby increase the rate of spectral relaxation in DH4T relative to 4T,[34] contrary to what we have observed experimentally. Thus, comparisons between 4T, DH4T and computations with 2T are supportive of assignment of these frequency shifts to an ultrafast relaxation of the torsional conformation. We note that the frequencies corresponding with these spectral relaxation timescales fall in the range of 50-100 cm^{-1}, and are quite close to previous estimates of torsional frequencies for related thiophene systems.[6,35] In fact, from our excited-state calculations we find that vibrations with significant torsional twisting character occur at 36.2 and 81.8 cm^{-1} for 4T and 26.5 and 72.3 cm^{-1} for DE4T; these are consistent qualitatively with both the values and trends in relaxation timescales measured experimentally with 4T and DH4T.

In contrast to what we observe for the excited state, the intensities and frequencies for both the Я and Z modes are predicted to exhibit significant sensitivity to the structural and morphological order of conjugated polymers and oligomers in their ground states.[20-22,36] For example, DFT calculations of ground-state Raman spectra of sexithiophene (6T) conducted with a range-corrected functional predict a red shift (~ 13 cm^{-1} with CAM-B3LYP/6-31g) with a substantial intensity increase when the central dihedral angle decreases from 90° to 0°;[22] at the same time, the red shift of the Z mode is 9 cm^{-1}. These differences in the torsional dependence of modes in the excited and ground states are likely a reflection of significant differences in the mode character between electronic states. Detailed theoretical analysis will be required for a complete understanding of intensity and frequency trends observed here for the excited states and why they differ from the predicted trends in the ground state.

The spectral dynamics observed here are unlike structural dynamics we have observed previously in polythiophene systems using similar methods. Previously we reported on the ultrafast photo-induced nuclear relaxation of poly(3-cyclohexyl,4-methylthiophene) (PCMT), which induces a red-shift in the Я mode on a ~100 fs timescale.[3] This shift is a reflection of the self-trapping or localization of a nascent exciton along the polymer backbone.[6,12,13] In contrast, the excited-state of 4T and DH4T extends across the entire molecule, such that structural deformations that enable exciton localization are not necessary; thus, results of this work reflect the relaxation of a de facto localized excited-state distribution. In conjugated polymers, subsequent relaxation is thought to involve resonant excitonic energy transfer or long-range torsional relaxation, both of which should yield more planar structural motifs, however the role of charge-separated states in the photophysics of excited states of amorphous polymers has also been recognized.[37] Thus, our findings provide insights on what spectral markers at the vibrational level will be most appropriate for probing torsional relaxation of localized excitons on a polymer chain.

In conclusion, we have employed FSRS to interrogate the ultrafast structural dynamics of two quaterthiophenes with structures that differ somewhat due to the absence (4T) or presence (DH4T) of bulky alkyl substituents. The intensities and frequencies of out-of-phase and in-phase mode intensities are found to be correlated with the interring torsional dihedral, as supported with quantum chemical computations with the model system bithiophene. Torsional relaxation timescales obtained from the Z mode shift are 0.40 and 0.86 ps, respectively, which are qualitatively similar to timescales obtained previously via transient electronic spectroscopies.[14,15,18,19] An important finding of this work is that FSRS can directly probe the dynamics of specific modes, providing a distinct observation of structural evolution, therefore facilitating greater understanding of the nuclear conformational dynamics in photoexcited conjugated molecules than can be gleaned from electronic spectroscopy alone. For example, previous studies of relaxation in 4T and quaterthiophene derivatives could only vaguely ascribe spectral shifts in stimulated emission bands to a combination of vibrational and torsional relaxation dynamics on sub-ps and ps timescales,[14] respectively, whereas the present study directly demonstrates via a mode-specific structural probe that torsional relaxation occurs on sub-ps timescales. Such insights are valuable for further interrogation and assessment of the structural evolution that accompanies initial exciton localization and subsequent localized conformational ordering or exciton diffusion in conjugated polymers.[3-12]

2.5. Supporting material

2.5.1. Steady-state UV-Vis and fluorescence spectroscopy of 4T and DH4T

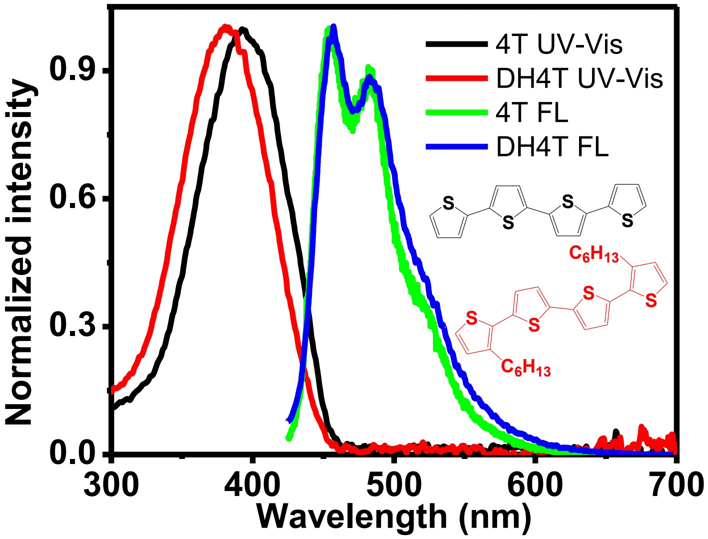

Figure 2.1S. Normalized steady-state UV-Vis absorption and fluorescence spectra of 4T and DH4T dissolved in chlorobenzene (CB) (2.0×10^{-3} M). The structures of 4T and DH4T are shown in the inset. The relative UV-Vis peak position for DH4T (compared to 4T) can be attributed to the effect of the alkyl substituents on the structure (vide infra) and, therefore, π conjugation of the oligothiophene chromophore in its ground state.

2.5.2. Quantum-chemical calculations

All computational geometry optimizations were performed at the CAM-B3LYP/6-31G* level using the Gaussian 09 package.[38] Calculations of excited-state Raman spectra of 2T through a scan of the central dihedral angle θ were carried out with QChem 4.2.[28]

2.5.2.1 Ground-state optimization of S_0 4T and DE4T structures and frequencies

S_0 geometry optimization of 4T and DE4T (a computationally tractable substitute for DH4T) were performed without symmetry constraints. No imaginary frequencies were found at the optimized structures for both molecules.

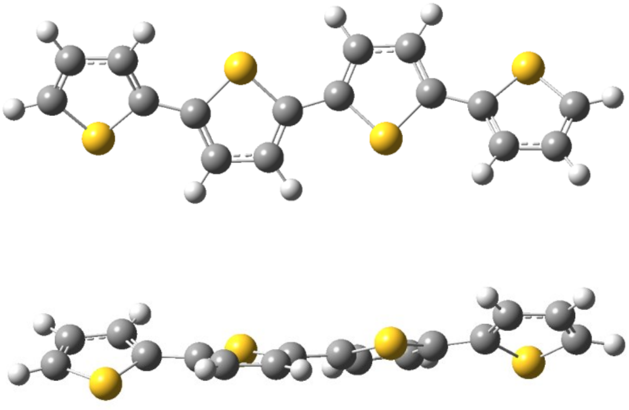

Figure 2.2S. S_0 optimized structure of 4T viewed from top (above) and side (bottom).

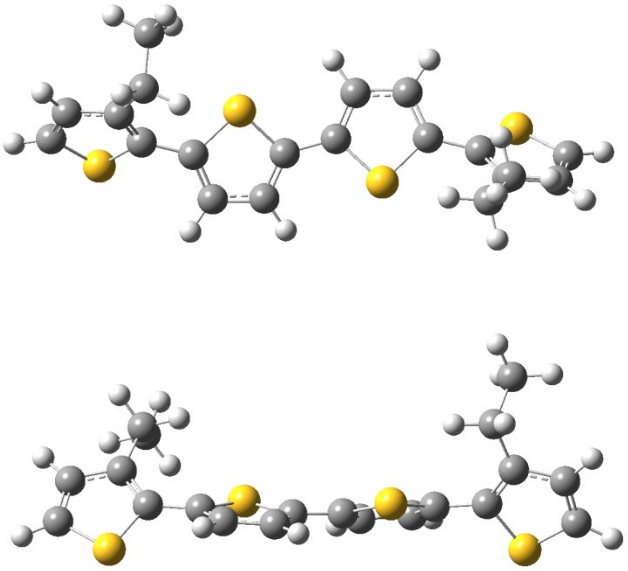

Figure 2.3S. S_0 optimized structure of DE4T viewed from top (above) and side (bottom).

2.5.2.2 Time-dependent density functional theory (TD-DFT) optimization of S_1 4T and DE4T structures and frequencies

S_1 geometry optimization of 4T and DE4T was performed without symmetry constraints. No imaginary frequencies were found at the optimized structures for both isomers.

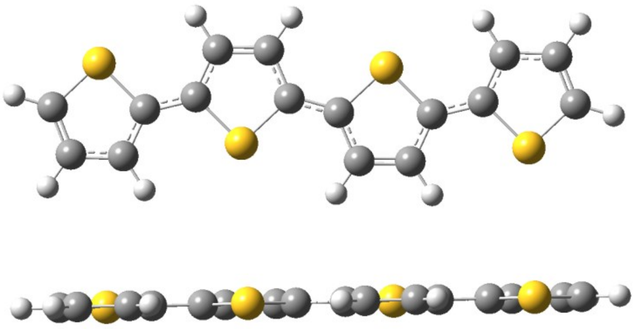

Figure 2.4S. S_1 optimized structure of 4T viewed from top (above) and side (below).

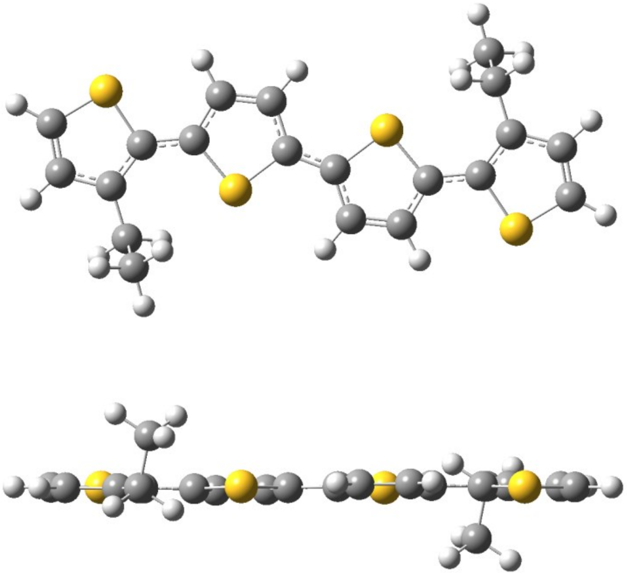

Figure 2.5S. S_1 optimized structure of DE4T viewed from top (above) and side (below).

2.5.2.3 Visualizing the nominal ring deformation, in-phase C=C and out-of-phase C=C stretch modes in 2T, 4T and DE4T

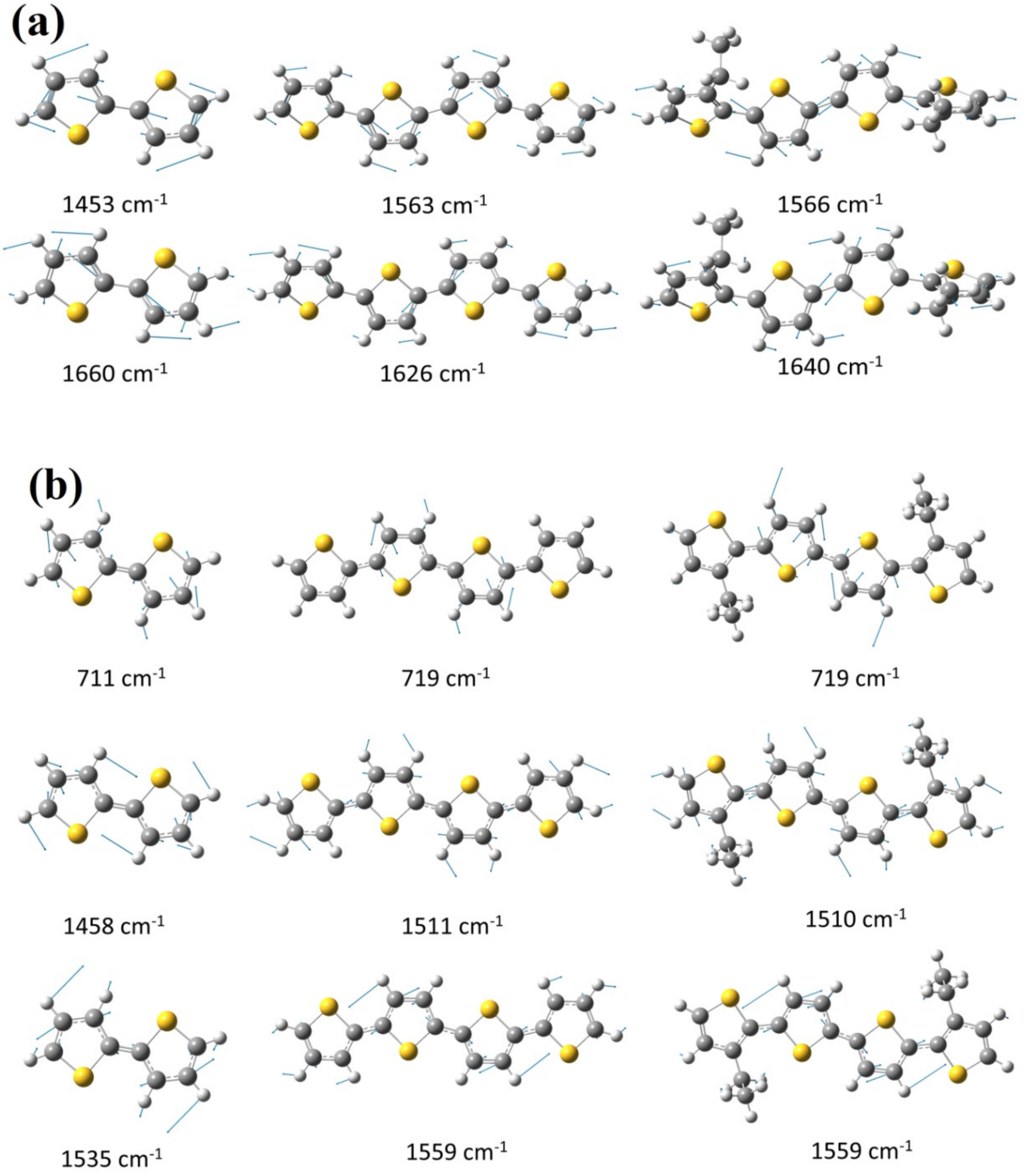
(a)
1453 cm^{-1}
1563 cm^{-1}
1566 cm^{-1}
1660 cm^{-1}
1626 cm^{-1}
1640 cm^{-1}
(b)
711 cm^{-1}
719 cm^{-1}
719 cm^{-1}
1458 cm^{-1}
1511 cm^{-1}
1510 cm^{-1}
1535 cm^{-1}
1559 cm^{-1}
1559 cm^{-1}

Figure 2.6S. Visualization of the (a) in-phase C=C stretch mode (above) and out-of-phase C=C stretch mode (below) in S$_0$ 2T, 4T and DH4T and (b) ring deformation mode (above), in-phase C=C stretch mode (middle) and out-of-phase C=C stretch mode (below) in S$_1$ 2T, 4T and DH4T. All the calculated frequencies from 4T and DH4T are consistently higher than those measured experimentally and presented in the main text, as no frequency scaling factors have been applied. Figures were prepared using GaussView 5.0.

2.5.2.4 Comparison between experimental (4T and DH4T) and theoretical (2T) excited-state Raman spectra, and dependence of the Я and Z mode frequencies and intensities with interring dihedral angles spanning 0 to 40°

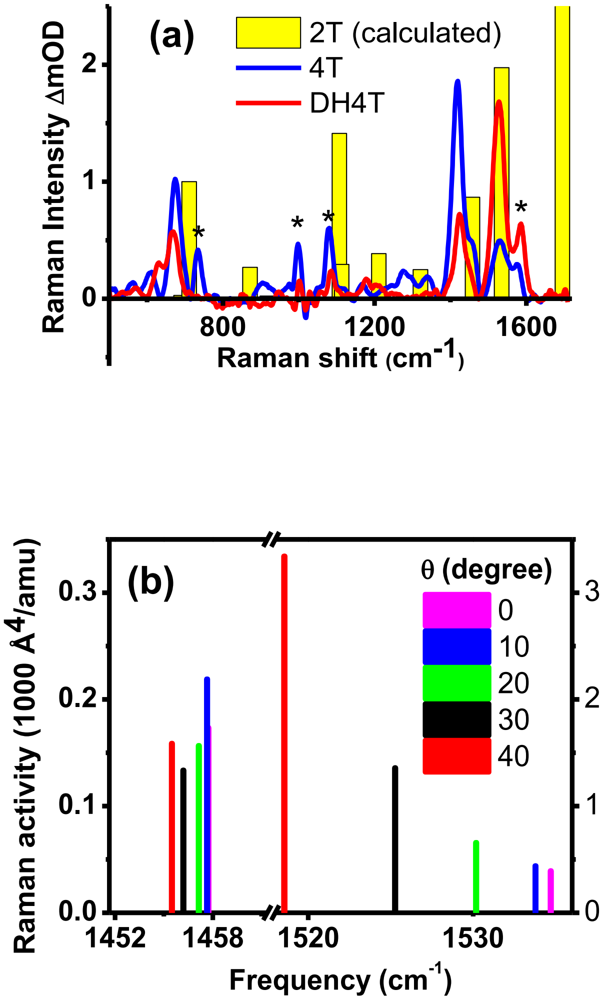

Figure 2.7S. (a) Calculated ER of 2T compared with the FSRS spectra of photoexcited 4T and DH4T obtained 2 ps after photoexcitation. Although an intense H bending mode and a C-C interring stretching mode predicted at 1107 cm^{-1} and 1695 cm^{-1} do not appear in the experimental spectra, the positions of the three main excited-state Raman bands observed are identified and are in qualitative accord with the results of the Raman intensity calculation. (b) Frequencies and intensities of the in-phase and out-of-phase C=C stretching modes of 2T as a function of torsional dihedral angle, θ, plotted at the left and right side of the break, respectively. When θ varies from 40 to 0 degree, the Я mode shows only a 3-cm^{-1} blue shift and modest intensity increase, whereas the Z mode exhibits a 16-cm^{-1} blue shift and an 8.5 fold intensity decrease.

2.5.3. Transient absorption spectroscopy (TAS) of 4T

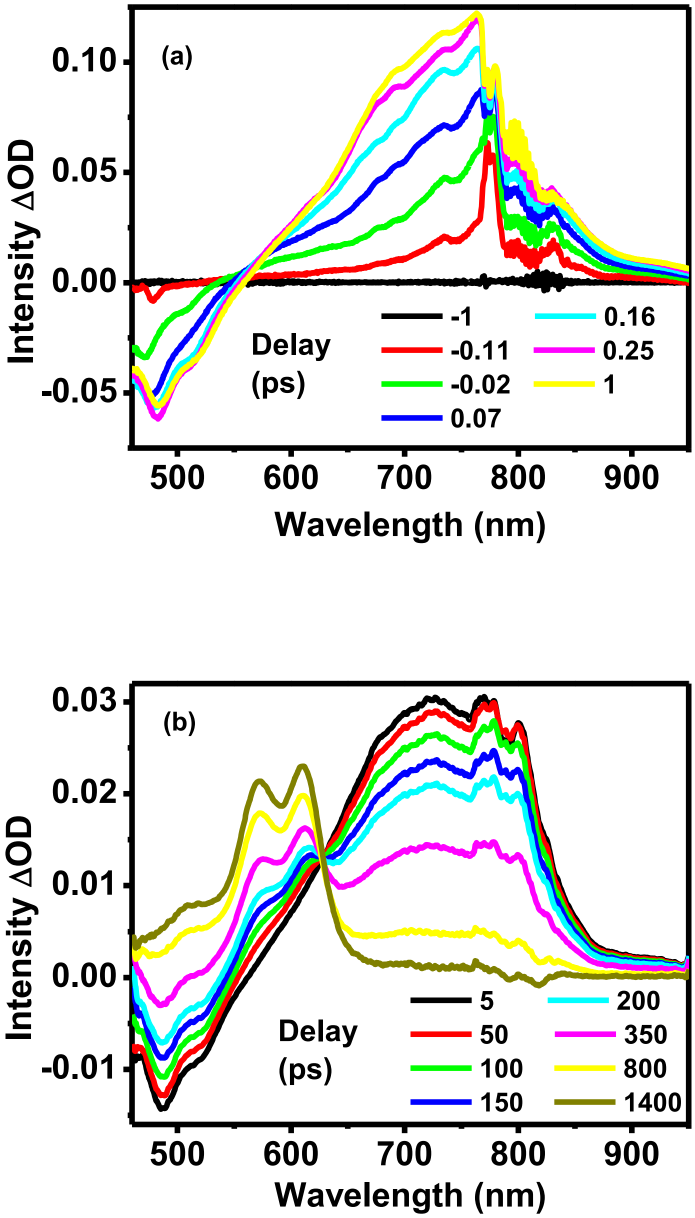

Figure 2.8S. TAS spectra of 4T at (a) early and (b) late delays following photoexcitation at 420 nm in CB. (The uneven spectral shapes occur near the driving wavelength for white-light generation between 720 and 840 nm.) Early delays illustrate the appearance and relaxation of the S_1 state; the latter is most apparent from the time-dependent position of the stimulated emission (described further below). Data collected on later delays illustrate that S_1 4T decays in part via ISC to the triplet manifold, with characteristic triplet features near 600 nm.

2.5.4. TAS of relaxed S$_1$ 4T and DH4T (2 ps pump-probe delay)

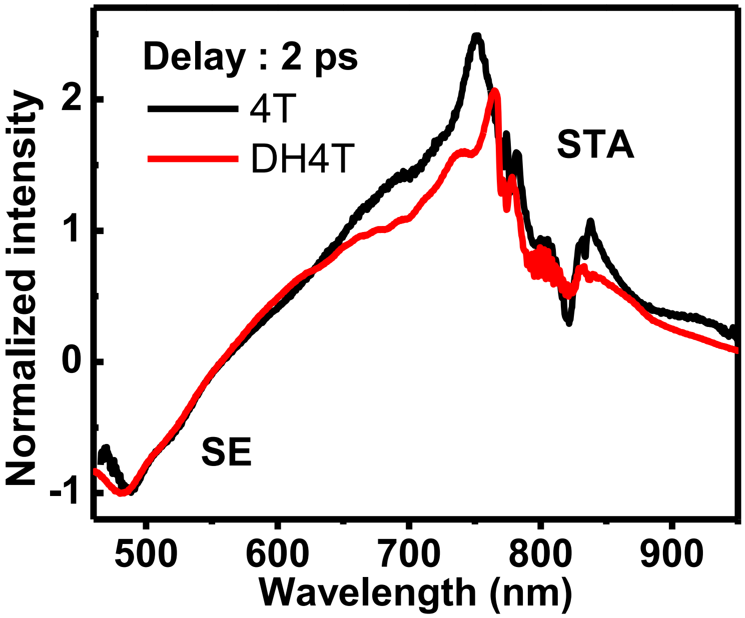

Figure 2.9S. Comparison of normalized TAS spectra of 4T and DH4T at a 2 ps time delay following photoexcitation at 420 nm in chlorobenzene (CB). (The uneven spectral shapes occur near the driving wavelength for white-light generation between 720 and 840 nm.) Transient spectra of the two species are highly similar. Raman–excitation wavelengths used in our experiments were chosen to be resonant with the red edge of the S$_1$ absorption band (850 and 880 nm for 4T and DH4T, respectively).

2.5.5. Fitting of weighted average wavelength of 4T and DH4T stimulated emission

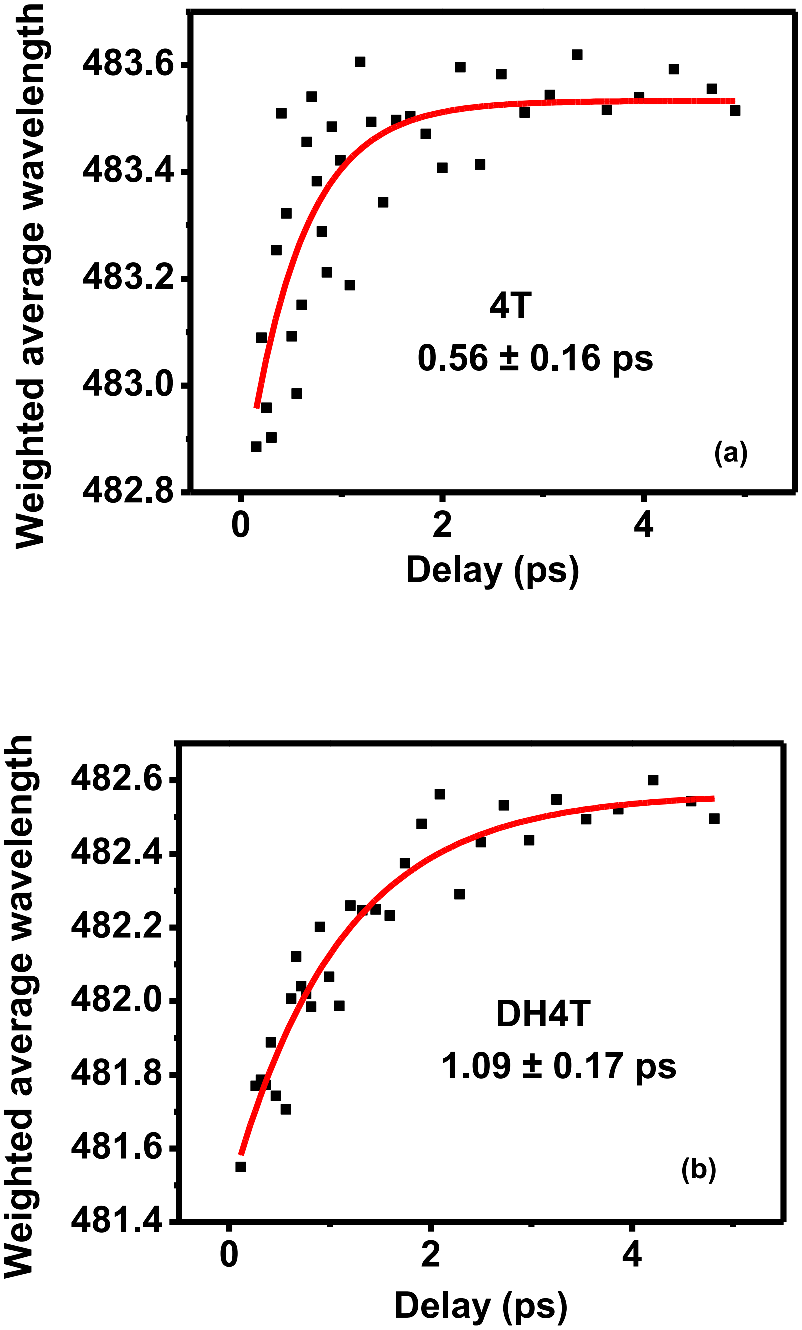

Figure 2.10S. Weighted average wavelength of the simulated emission of (a) 4T and (b) DH4T. Weighted average wavelengths were determined between 460 and 505 nm. Shifting timescales are similar to the relaxation time-scales obtained from Raman spectra (main text) and are similar to relaxation timescales obtained for 4T analogs via TAS previously.[14]

2.5.6. Additional details of experimental setup

The experimental setup has been described in detail previously.[3,4] Here we emphasize experimental details particularly relevant to this work. Ultrafast laser pulses for all measurements were obtained from the fundamental output of an amplified Ti:Sapphire laser (Coherent Legend Elite, 4.5 mJ/pulse, 1 kHZ repetition rate, 35-fs pulse duration, 800-nm peak wavelength). The 350 nm actinic pump was generated with an optical parametric amplifier (Coherent OperaSolo) through fourth harmonic generation of the OPA signal at 1440 nm. Raman pump light at either 850 or 880 nm was obtained from a white-light-seeded OPA (TOPAS-400, Light Conversion) pumped with the 400-nm output of a second-harmonic bandwidth compressor (SHBC, Light Conversion). Weak broadband probe pulses (850 – 1100 nm) were generated in a 2-mm-thick sapphire crystal. Parallel polarizations of all three pulses (actinic pump, Raman pump and whitelight probe) were adopted for FSRS measurement.

2.5.7. FSRS signal analysis procedures

FSRS data acquisition algorithms can be found in our previous publications.[3,4] Here, pure excited-state Raman spectra (ER) were obtained using the Raman-excitation chopped (RC) and ground-state Raman (GR) spectra; pulse combinations used for these measurements are indicated with subscripts in Equation 2.1:

$$RC = \log(I_{pu+r+pr}/I_{pu+pr}) \tag{2.1a}$$

$$GR = \log(I_{r+pr}/I_{pr}) \tag{2.1b}$$

The subscripts in Eqn. 2.1 refer to the actinic photoexcitation (pu), Raman excitation (r) and white light probe (pr) pulses, respectively.

Because the Raman pump wavelength is rather far from the ground-state absorption band of either 4T or DH4T, the non-resonant Raman signals from the solute are negligible. Therefore, the RC spectrum only contains the solute ER, solvent (chlorobenzene, CB) GR, Raman-pump induced modulations in transient absorption (TA) and other signals from nonlinear processes. Firstly, we use the pure GR signal measured experimentally (Eqn. 2.1Sb) to remove contributions to RC from the solvent as follows: Because the Raman pump is pre-resonant with an S_1 to S_n transition, the Raman pump can depopulate the S_1 state through absorption to higher excited states; this is known to affect the magnitude of the excited-state Raman signal. To account for this, we introduce a scaling factor, *m*, to fully subtract the chlorobenzene solvent peaks between 950 and 1200 cm^{-1}. A typical value for *m* is 0.70 – 0.75 before 0.25 ps and 0.66 – 0.68 between 0.30 and 10 ps for both quaterthiophenes. The variation in *m* with time delay reflects that the Raman-pump intensity varies with time delays on account of the sample absorption that depletes the S_1 population. Thus, the *m* value was employed to correct time-resolved FSRS intensities for this population depletion effect. Because the excited-state Raman features observed are quite narrow, the residual baseline from the RC – *m**GR can be accurately estimated by a spline fit. In total, excited-state Raman spectra were determined by the following formula:

$$\mathrm{ER} = (\mathrm{RC} - m^{*}\mathrm{GR}) / m - \mathrm{Fit} \qquad (2.2)$$

A graphical example of our data work-up is given in Figure S2.11.

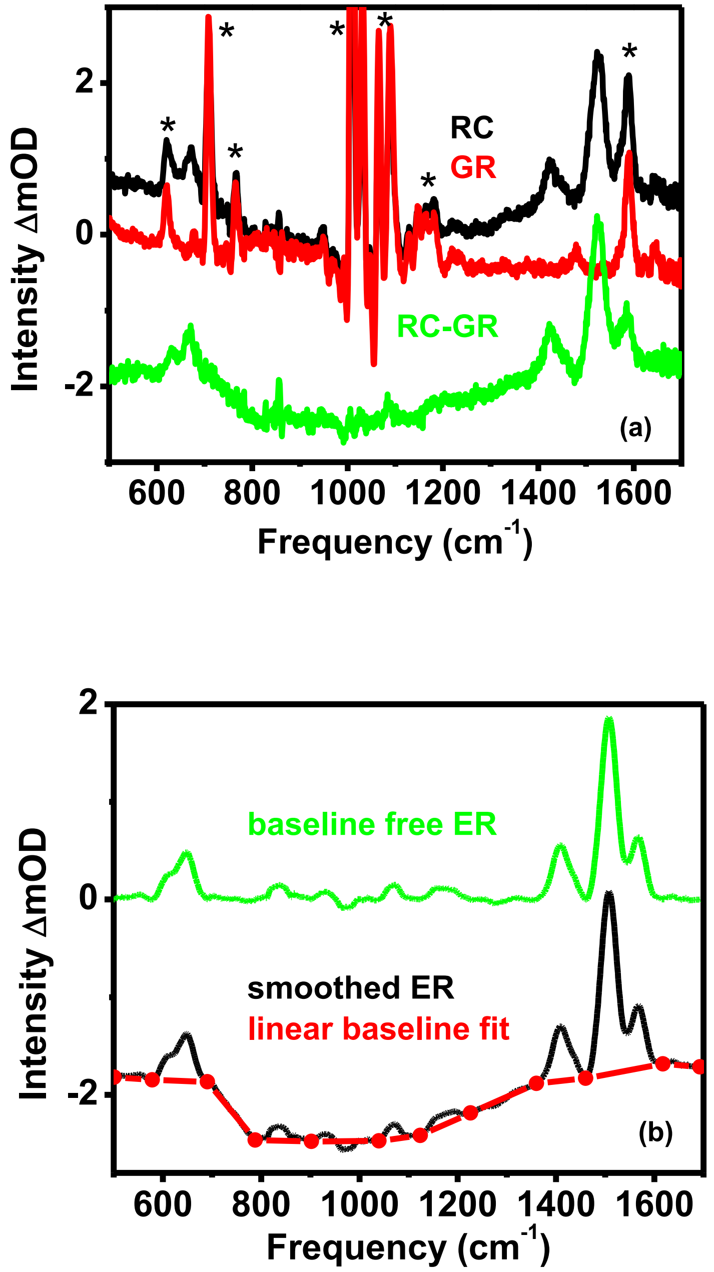

Figure S2.11. (a) Raw FSRS data of DH4T at 0.6 ps time delay and solvent subtraction routine. GR was multiplied by a factor m = 0.66 and employed to fully subtract the solvent and any non-resonant solute features from RC. Residual solvent signals are marked with asterisks. The RC – GR (i.e. ER) spectrum is offset vertically for clarity. (b) Removal of residual baseline. The ER spectrum was first smoothed in a Labview Program (Savitzky-Golay filter, polynomial order = 3, side points = 16). The baseline shape was determined with a linear spline. Finally the estimated baseline was subtracted from the smoothed ER spectrum to generate the baseline free ER.

2.6. References

(1) Facchetti, A. *Chem. Mater.* **2011**, *23*, 733.

(2) Günes, S.; Neugebauer, H.; Sariciftci, N. S. *Chem. Rev.* **2007**, 1324.

(3) Yu, W.; Donohoo-Vallett, P. J.; Zhou, J.; Bragg, A. E. *J. Chem. Phys.* **2014**, *141*, 044201.

(4) Yu, W.; Zhou, J.; Bragg, A. E. *J. Phys. Chem. Lett.* **2012**, *3*, 1321.

(5) Wells, N. P.; Boudouris, B. W.; Hillmyer, M. A.; Blank, D. A. *J. Phys. Chem. C* **2007**, *111*, 15404.

(6) Wells, N. P.; Blank, D. A. *Phys. Rev. Lett.* **2008**, *100*, 086403.

(7) Busby, E.; Carroll, E. C.; Chinn, E. M.; Chang, L.; Moulé, A. J.; Larsen, D. S. *J. Phys. Chem. Lett.* **2011**, *2*, 2764.

(8) Clark, J.; Nelson, T.; Tretiak, S.; Cirmi, G.; Lanzani, G. *Nat. Phys.* **2012**, *8*, 225.

(9) Scholes, G. D. *Annu. Rev. Phys. Chem.* **2003**, *54*, 57.

(10) Collini, E.; Scholes, G. D. *Science* **2009**, *323*, 369.

(11) Westenhoff, S.; Beenken, W. J. D.; Friend, R. H.; Greenham, N. C.; Yartsev, A.; Sundström, V. *Phys. Rev. Lett.* **2006**, *97*, 166804.

(12) Banerji, N.; Cowan, S.; Vauthey, E.; Heeger, A. J. *J. Phys. Chem. C* **2011**, *115*, 9726.

(13) Hwang, I.; Scholes, G. D. *Chem. Mater.* **2011**, *23*, 610.

(14) Lanzani, G.; Nisoli, M.; Silvestri, S. D.; Tubino, R. *Chem. Phys. Lett.* **1996**, *251*, 339.

(15) Kim, P.; Park, K. H.; Kim, W.; Tamachi, T.; Iyoda, M.; Kim, D. *J. Phys. Chem. Lett.* **2015**, *6*, 451.

(16) Lanzani, G.; Nisoli, M.; Magni, V.; De Silvestri, S.; Barbarella, G.; Zambianchi, M.; Tubino, R. *Phys. Rev. B* **1995**, *51*, 13770.

(17) Lanzani, G.; M, N.; Silvestri, S. D.; Tubino, R. *Synt. Met.* **1996**, *76*, 39.

(18) Paa, W.; Yang, J. P.; Rentsch, S. *Appl. Phys. B* **2000**, *71*, 443.

(19) Yamaguchi, S.; Hamaguchi, H.-o. *Chem. Phys. Lett.* **1994**, *227*, 255.

(20) Castiglioni, C.; Zoppo, M. D.; Zerbi, G. *J. Raman Spectrosc.* **1993**, *24*, 485.

(21) Hernandez, V.; Castiglioni, C.; Del Zoppo, M.; Zerbi, G. *Phys. Rev. B* **1994**, *50*, 9815.

(22) Donohoo-Vallett, P. J.; Bragg, A. E. *J. Phys. Chem. B* **2015**, *119*, 3583.

(23) Iwata, K.; Hamaguchi, H.-o. *J. Raman Spectrosc.* **1994**, *25*, 615.

(24) Hamaguchi, H.-o.; Gustafson, T. L. *Annu. Rev. Phys. Chem.* **1994**, *45*, 593.

(25) Kukura, P.; McCamant, D. W.; Mathies, R. A. *Annu. Rev. Phys. Chem.* **2007**, *58*, 461.

(26) Frontiera, R. R.; Mathies, R. A. *Laser Photon. Rev.* **2011**, *5*, 102.

(27) Gaussian09, RevisionA.1: M. J. Frisch, et al. Gaussian, Inc., Wallingford CT, 2009.

(28) Shao, Y.; Molnar, L. F.; Jung, Y.; Kussmann, J.; Ochsenfeld, C.; Brown, S. T.; Gilbert, A. T.; Slipchenko, L. V.; Levchenko, S. V.; O'Neill, D. P.; DiStasio, R. A., Jr.; Lochan, R. C.; Wang, T.; Beran, G. J.; Besley, N. A.; Herbert, J. M.; Lin, C. Y.; Van Voorhis, T.; Chien, S. H.; Sodt, A.; Steele, R. P.; Rassolov, V. A.; Maslen, P. E.; Korambath, P. P.; Adamson, R. D.; Austin, B.; Baker, J.; Byrd, E. F.; Dachsel, H.; Doerksen, R. J.; Dreuw, A.; Dunietz, B. D.; Dutoi, A. D.; Furlani, T. R.; Gwaltney, S. R.; Heyden, A.; Hirata, S.; Hsu, C. P.; Kedziora, G.; Khalliulin, R. Z.; Klunzinger, P.; Lee, A. M.; Lee, M. S.; Liang, W.; Lotan, I.; Nair, N.; Peters, B.; Proynov, E. I.; Pieniazek, P. A.; Rhee, Y. M.; Ritchie, J.; Rosta, E.; Sherrill, C. D.; Simmonett, A. C.; Subotnik, J. E.; Woodcock, H. L., 3rd; Zhang, W.; Bell, A. T.; Chakraborty, A. K.; Chipman, D. M.; Keil, F. J.; Warshel, A.; Hehre, W. J.; Schaefer, H. F., 3rd; Kong, J.; Krylov, A. I.; Gill, P. M.; Head-Gordon, M. *Phys. Chem. Chem. Phys.* **2006**, *8*, 3172.

(29) Kuhn, H. *J. Chem. Phys.* **1949**, *17*, 1198.

(30) Benincori, T.; Bongiovanni, G.; Botta, C.; Cerullo, G.; Lanzani, G.; Mura, A.; Rossi, L.; Sannicolo, F.; Tubino, R. *Phys. Rev. B* **1998**, *58*, 9082.

(31) Tsoi, W. C.; James, D. T.; Kim, J. S.; Nicholson, P. G.; Murphy, C. E.; Bradley, D. D.; Nelson, J. *J. Am. Chem. Soc.* **2011**, *133*, 9834.

(32) Zerbi, G.; Chierichetti, B.; Ingänas, O. *J. Chem. Phys.* **1991**, *94*, 4637.

(33) Lopez Navarrete, J. T.; Zerbi, G. *J. Chem. Phys.* **1991**, *94*, 957.

(34) Benten, R. S. v.; Liu, Y.; Abel, B. *J. Phys. Chem. A* **2010**, *114*, 11522.

(35) Filho, D. A.; Coropceanu, V.; Fichou, D.; Gruhn, N. E.; Bill, T. G.; Gierschner, J.; Cornil, J.; Bredas, J. L. *Phil. Trans. R. Soc. A* **2007**, *365*, 1435.

(36) Milani, A.; Brambilla, L.; Zoppo, M. D.; Zerbi, G. *J. Phys. Chem. B* **2007**, *111*, 1271.

(37) Tapping, P. C.; Kee, T. W. *The Journal of Physical Chemistry Letters* **2014**, *5*, 1040.

(38) Gaussian 09, Revision A.01, M. J. Frisch, G. W. Trucks, H. B. Schlegel, G. E. Scuseria, M. A. Robb, J. R. Cheeseman, G. Scalmani, V. Barone, B. Mennucci, G. A. Petersson, H. Nakatsuji, M. Caricato, X. Li, H. P. Hratchian, A. F. Izmaylov, J. Bloino, G. Zheng, J. L. Sonnenberg, M. Hada, M. Ehara, K. Toyota, R. Fukuda, J. Hasegawa, M. Ishida, T. Nakajima, Y. Honda, O. Kitao, H. Nakai, T. Vreven, J. A. Montgomery, Jr., J. E. Peralta, F. Ogliaro, M. Bearpark, J. J. Heyd, E. Brothers, K. N. Kudin, V. N. Staroverov, R. Kobayashi, J. Normand, K. Raghavachari, A. Rendell, J. C. Burant, S. S. Iyengar, J. Tomasi, M. Cossi, N. Rega, M. J. Millam, M. Klene, J. E. Knox, J. B. Cross, V. Bakken, C. Adamo, J. Jaramillo, R. Gomperts, R. E. Stratmann, O. Yazyev, A. J. Austin, R. Cammi, C. Pomelli, J. W. Ochterski, R. L. Martin, K. Morokuma, V. G. Zakrzewski, G. A. Voth, P. Salvador, J. J. Dannenberg, S. Dapprich, A. D. Daniels, Ö. Farkas, J. B. Foresman, J. V. Ortiz, J. Cioslowski, D. J. Fox, Gaussian, Inc., Wallingford CT, 2009.

Chapter 3: Visible-Light-Induced E/Z Isomerization of a 1,2-Dicyanoethene Derivative via Multiplicity-Exclusive Photoisomerization Pathways

In part a compilation of two publications:

1. Guo, X.; Zhou, J.; Siegler, M. A.; Bragg, A. E.; Katz, H. E. *Angew. Chem., Int. Ed.* **2015,** *54*, 4782-4786.

2. Zhou, J.; Guo, X.; Katz, H. E.; Bragg, A. E. *J. Am. Chem. Soc.* **2015,** *17*, 10841-10850.

This work was collaborative in conjunction with Xin Guo[†] and Howard E. Katz[†].

[†]Department of Materials Science and Engineering, Johns Hopkins University, Baltimore, MD 21218, USA

3.1. Introduction

Photoswitchable molecules and materials that exhibit substantial changes in structure or functional properties upon wavelength-selective excitation are of considerable interest for numerous applications,[1-3] including photochromism,[4] memory storage,[5] logic devices,[6] molecular motors,[7,8] mechanical manipulation,[9-13] and light-triggered chemical sensitization[14] and conductivity.[15] Photoswitches that operate via large-scale structural changes, such as E/Z isomerization, are particularly attractive for manipulating the distance between chemical or biochemical moieties to interrogate the nature of their interactions.[9-13,16-19] Photoswitching also has potential for controlling or patterning morphologies of aggregated organic materials.[20,21] Desirable photoswitch characteristics include high conversion efficiency,[22,23] robust fatigue resistance,[24] and the feasibility for isomerization at red excitation wavelengths[25-27] that can transmit through materials such as biological tissue.[9] In addition, mutual exclusivity in the nature of the excited-state relaxation pathways that drive forward and reserve isomerization reactions can provide a handle for controlling the reversibility of a switch as desired for a particular application.[28,29] On all counts, an understanding of photophysical dynamics and how they may be manipulated with structure are of prime importance for the synthetic design of photoresponsive materials.

Conventional photochromic molecules, like azobenzene (AB) and its derivatives, have attracted numerous attentions, and have been studied in depth for decades. However, AB suffers from a drawback that limits its practical use in biological and materials sciences, since the utilization of UV light, necessary to induce the Z → E isomerization via $\pi \rightarrow \pi^*$ excitation, may potentially lead to photodamage to other moieties attached to the AB unit.[23,30,31] In contrast, conjugated oligo-thiophenes, like 1,2-dithienyl-1,2-dicyanoethene (4TCE), can circumvent this limitation, because the very transition band associated with the Z → E isomerization has a substantial red shift. Moreover, the visible absorption bands of both isomers are well separated, with a fairly large disparity of the oscillator strength, which gives rise to a strong wavelength selectivity over different isomers in the visible region.

Herein we report a thorough ground- and excited-state characterization of 4TCE, which can be induced to isomerize via excitation at visible wavelengths and that exhibits relatively high photostationary yields for photochromic conversion upon irradiation. The UV-Vis spectra and structures for both *cis* and *trans* isomers are shown in Figure 3.1 (a). The *trans* isomer of 4TCE is most stable energetically when dissolved in solution at room temperature, but is readily converted to the more photostable *cis* isomer in 100% yield upon exposure to room lights, as demonstrated in Figure 3.1 (b). In contrast, the reverse process can be accomplished either through illumination with blue light (<440 nm, ~60% photostationary conversion in toluene, Figure 3.1 (c)) or by heating (>80 ^{o}C, 100% conversion, Figure 3.1 (d)). Importantly, the low reactivity of the β carbon sites on the thiophene rings eliminates the possibility of a competing cyclization pathway at low energies, such that 4TCE is a two-state E/Z switch when used in conjunction with visible light. Additionally, 4TCE possesses high photostability, with no detectable photodegradation after several isomerization cycles. A particularly attractive feature of the 4TCE switch design is that oligothienyl groups could be lengthened, affecting both photoswitchable mechanical separation of its two ends and the spectral properties of the switch; notably, longer pendant oligothienyl groups would give rise to increased molecular conjugation and a redder absorption spectrum.

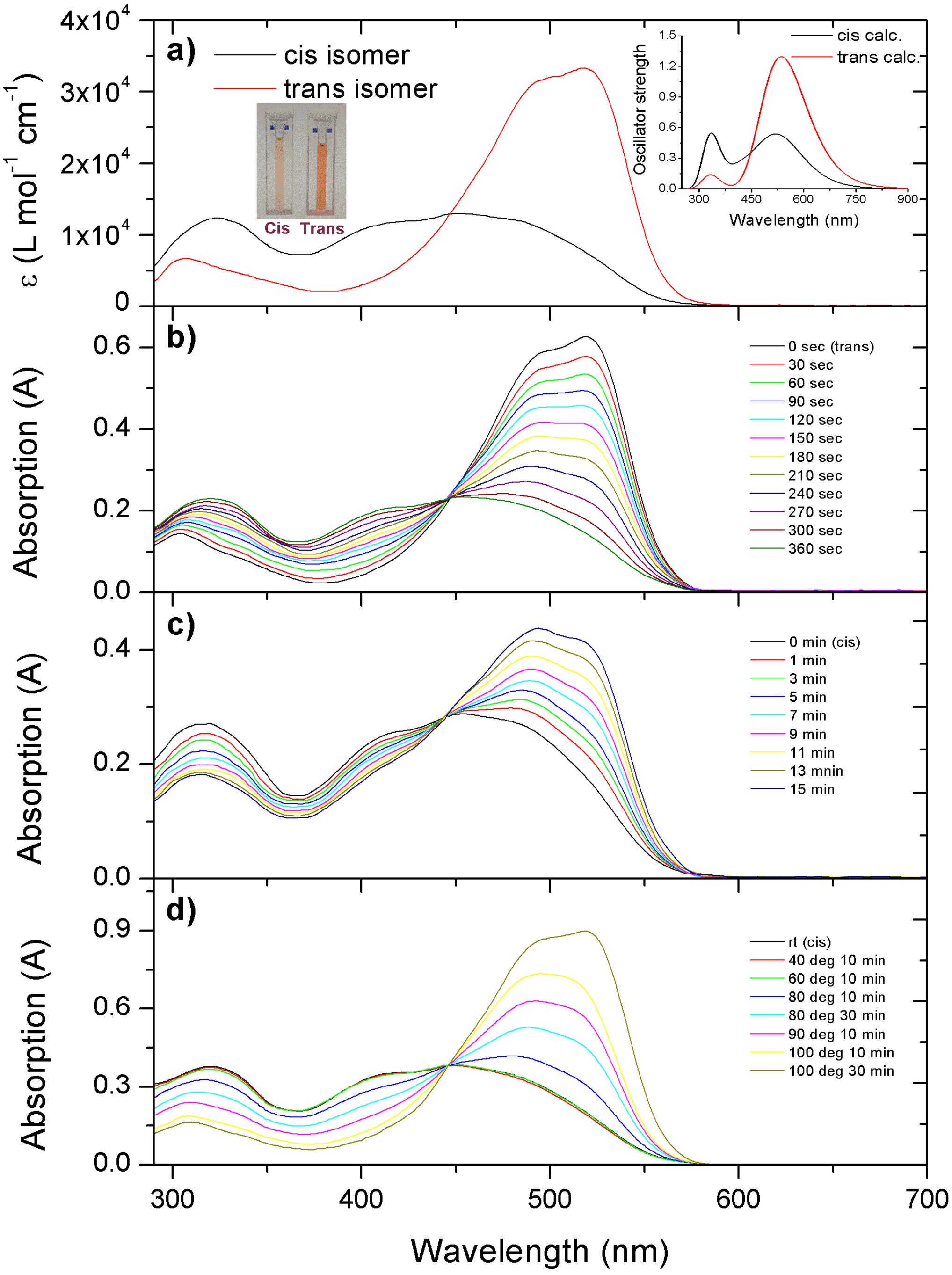

Figure 3.1. (a) UV-vis absorption spectra of pure *cis* and *trans* isomers of 4TCE in toluene solution (the same below) at room temperature. Insets: calculated UV-vis spectra (top right) and a picture showing the obviously different color of two isomers in solution. (b) E→Z photoisomerization of the 4TCE, irradiated by white light. (c) Z→E photoisomerization of the 4TCE, irradiated by blue light at 420 nm. (d) Thermal Z→E isomerization of the 4TCE. All these experiments are carried out in 10^{-5} M solutions.

We ascribed the photoswitching characteristics of 4TCE to the large separation in maximum absorption wavelength (λ_{max}) and differences in molar extinction coefficient (ε) between the *trans* and *cis* isomers (Figure 3.1 (a)): λ_{max} for the *trans* and *cis* isomers are located at 520 and 470 nm in toluene, and the ε of *trans* is 2.5 times larger than that of *cis* at their respective λ_{max}. However, a complete characterization of the relative photoselectivity for each of these pathways and their corresponding photostationary yields must also take into consideration the energy-dependent quantum yields for isomerization, which are determined by the nature of underlying photophysical processes. As small thiophene-based systems are known to exhibit large spin-orbit couplings (SOCs) and efficient intersystem crossing (ISC) rates in their excited states due to the presence of sulfur atoms,[32-37] the E-Z and Z-E isomerization reactions of 4TCE also might be expected to occur via electronic relaxation through either or both of the singlet and triplet manifolds; in contrast, E/Z switches such as stilbenes and azobenzenes only occur by way of singlet relaxation pathways upon direct photoexcitation.[12,38,39] Manifold-exclusive relaxation pathways could enable control of the relative significance of one pathway over the other by tailored molecular design, energy-transfer sensitization, or the application of external stimuli (e.g. electric fields). Thus, an understanding of photoswitching behavior and how to manipulate switch properties for improved performance or extended spectral utilization requires greater understanding of how molecular structure impacts the course of excited-state dynamics in either direction.

Towards this end, we have used ultrafast transient absorption (TA) spectroscopy to interrogate the relaxation pathways associated with the energy-dependent isomerization of 4TCE. We find that *trans*-to-*cis* isomerization occurs via relaxation only through singlet electronic states following low-energy excitation (530 nm); low-energy excitation of the *cis* isomer likewise results in electronic relaxation only via singlets, but with negligible isomerization. In contrast, transient spectral dynamics measured at higher excitation energies (420 nm) reveal that excited-state relaxation of both species and isomerization of the *cis* isomer, in particular, involves ISC into and out of the triplet manifold. As *cis* relaxation is driven by fast (~2 ps) and efficient ISC from the optically active singlet level, we hypothesize that structural modifications that enhance or disrupt spin-orbit couplings between manifolds could be used to manipulate *cis*-to-*trans* photostationary yields. We further demonstrate that triplet sensitization may provide an alternate method for highly pathway-selective E/Z isomerization of 4TCE and its derivatives at red wavelengths with high photostationary yield.

3.2. Experimental and computational methods

3.2.1. Sample preparation and characterization.

The synthesis of 4TCE has been described previously.[27] Solutions of 4TCE in chlorobenzene (CB, Fisher Scientific, >99% purity) were prepared at concentrations of ~2.4×10^{-5} mol/L. Sample solutions were circulated through a 1 mm path-length quartz flow cell for optical measurements. The optical density of the sample solutions were ~0.8 and ~0.3 for *trans* and *cis* at their peak absorption wavelengths, respectively. All components of the flow circuit are chemically resistant to sample solutions.

Exposure to room light can drive the isomerization from *trans* to *cis* in solution to completion, and therefore spectroscopic measurements of *trans*-to-*cis* isomerization were conducted in the absence of room light. In contrast, the pure *trans* form of 4TCE can be prepared by heating a *cis* or mixed *cis*/*trans* sample to 80 ^{O}C and then cooling it to room temperature in the dark. These processes were used to purify samples before laser experiments.

A diode-array spectrometer fiber-optically coupled to tungsten and incandescent deuterium light sources (Stellarnet) was used to measure steady-state UV-Vis spectra of sample solutions before and after time-resolved measurements. For measurements of *trans* to *cis* isomerization, no noticeable change of the *trans* ground state absorption was observed, indicating that the amount of *cis* generated from photoinduced isomerization during a course of two hours of experiments was negligible. Identical steady-state spectra of both *trans* and *cis* were measured with samples before and after experiments, implying that photoexcitation of 4TCE did not produce any additional photoproducts.

3.2.2. Transient absorption (TA).

Our experimental set-up has been described in detail elsewhere;[40,41] here we briefly note important features of the set-up that are critical for the experiments described in this work. Ultrafast light pulses used in these measurements were generated with a regeneratively amplified Ti:sapphire laser system (Coherent Legend Elite, 1 kHz rep. rate, 35-fs pulse duration, 4.0 mJ/pulse). Tunable excitation pulses were generated with an optical parametric amplifier (OPA, Coherent Operasolo), either through fourth-harmonic generation of the OPA signal (350-380 nm), fourth harmonic generation of the idler (420-460 nm) or sum-frequency of the signal (470-530 nm); 400-nm excitation pulses were generated via second-harmonic generation of the laser fundamental. Broadband probing continua (400-740 nm) were obtained by white-light generation in a 2-mm calcium fluoride (CaF_2) plate. Pulse energies for all actinic pump wavelengths were attenuated to about 1 μJ/pulse for all data presented. In order to eliminate signatures of time-dependent polarization anisotropy from the measured dynamics, the polarization of the white-light probe was set at the magic angle relative to the polarization of the actinic pump using a thin broadband wire-grid polarizer (Thorlabs) placed immediately before the sample. Probe pulses were focused to a spot size at the sample of 50 microns using an off-axis parabolic reflector; the pump beam was focused to a size of <100 μm and was overlapped with the probe beam at a small angle at the sample. The pump pulse delay relative to the probe pulse was controlled with a motorized translation stage (Newport), outfitted with a corner-cube mirror. Probe light transmitted through the sample was filtered and dispersed onto a multichannel array, and transient spectra were calculated using an acquisition algorithm described in the supporting material.

3.2.3. Computational.

Calculations using the Gaussian 09 package[42] were performed at the CAM-B3LYP/6-31G* level and utilized Polarizable Continuum Model (PCM) to incorporate the effect of solvent (chlorobenzene). All geometry optimizations were carried out without symmetry constraints. Vibrational analysis at the optimized geometries returned no imaginary frequencies. Relaxed potential-energy surfaces (PES) for the S_0 and T_1 states were performed by scanning the central ethylene dihedral angle between 0 and 180 degrees in 10 degrees per step and optimizing the structure at each step. Time-dependent density functional theory (TD-DFT) was used to determine the energies of geometry-relaxed S_1 states and vertical electronic transition energies from the S_0 and T_1 states.

Natural transition orbital (NTO) analysis was employed to assign the transition type. Spin-orbital constants (SOC) were calculated using the Breit-Pauli operator[43] in QChem 4.2.

3.3. Experimental results

3.3.1. Photoinduced dynamics of *trans*-4TCE.

3.3.1.1 Low-energy excitation of *trans*-4TCE (530 nm).

Figure 3.2(a) shows time-resolved TA spectra of *trans*-4TCE following its excitation at 530 nm. At early time delays the spectra consist of negative and positive intensities below and above 655 nm, respectively. Transient features are observed to decay over the few hundred picoseconds that follow excitation. In addition, the negative spectral intensity below 650 nm is observed to bifurcate on a timescale of ~10 ps. The bluer region of the negative features can be assigned to ground-state bleach (GSB) of *trans*-4TCE because it overlaps with the intense, lowest-energy band in the steady-state absorption spectrum of this isomer. Negative spectral intensity appearing at lower energies (~600 nm) therefore correspond with stimulated emission (SE) from the lowest-lying singlet excited state, as it matches the position of the steady-state fluorescence spectrum. The SE band and the positive signal above 655 nm share similar decay dynamics, and we can therefore attribute the latter to the excited-state transient absorption of the excited state (singlet transient absorption, or STA). At relatively long time delays (e.g. 464 ps in Figure 3.2(a)) only a permanent bleach remains between 475 and 550 nm, the shape of which matches the UV-Vis difference spectrum between *cis*- and *trans*-4TCE.

Single-wavelength traces at 510, 600 and 740 nm reflect the time-dependence of the GSB, SE and STA, respectively, and were used to characterize quantitatively the relaxation kinetics that follow excitation of *trans*-4TCE at 530 nm; these transients are plotted in Figure 3.2S, with fitting parameters tabulated in Table 3.1. The 510 nm transient is fit well by a single-exponential decay with a 39.2 ps lifetime. In contrast the SE and STA intensities both exhibit an additional fast decay component, such that a bi-exponential kinetic model is necessary to fit these traces accurately, with decay timescales of $\tau_1 \approx$ 2-3 ps and $\tau_2 \approx$ 38 ps. As GSB recovery only occurs on the longer of these timescales, the spectral dynamics of both the SE and STA bands must reflect ultrafast relaxation in the excited state. This assignment is corroborated by the observation of a fast shift in the SE band position, which reflects evolution in S_0-S_1 vertical energy gap between the Franck-Condon region and the excited-state minimum; characterization of this shift in SE is described in the supporting material. A global fit of spectral dynamics starting from 10 ps (after excited-state relaxation is complete) returns a 40.0 ps lifetime for the first excited state.

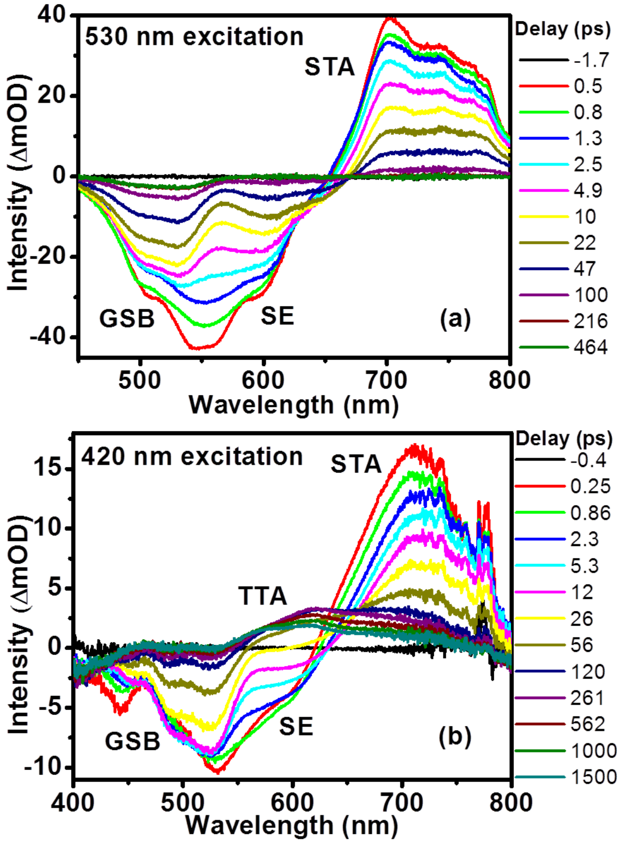

Figure 3.2. Transient absorption (TA) spectra of *trans*-4TCE in chlorobenzene excited at (a) 530 nm and (b) 420 nm. (a) Spectral evolution is characterized by decay of all three signals (GSB, SE, and STA) within 500 ps. A permanent GSB signal persists on longer timescales, reflecting that a fraction (11.6 %) of the excited state population isomerizes. (b) Spectral evolution is similar to that observed after 530-nm excitation at delays earlier than 20 ps, but exhibits signatures of triplet absorption on longer timescales.

The transient data shown in Figures 3.2(a) and 3.3S can be used to assess directly the quantum yield for *trans*-to-*cis* isomerization of *trans*-4TCE excited at 530 nm: Based on the decay and offset amplitudes of the exponential fit applied to the bleach data (Figure 2S), we find that 88.4% of the excited population of *trans*-4TCE returns to its ground state. This indicates an 11.6 ± 1.4% *trans*-to-*cis* isomerization yield at 530 nm, assuming that there are no additional excited-state deactivation/isomerization pathways. A distinct *cis* STA is either absent or not resolved in the TA spectral progression, reflecting that isomerization involves a direct nonradiative transition (S_1-to-S_0) from *trans* to *cis* or that both isomers have similar STA bands after 10 ps (vide infra).

3.3.1.2 High-energy excitation of *trans*-4TCE (420 nm).

TA spectra of *trans*-4TCE excited at 420 nm are displayed in Figure 3.2(b). At early time delays (<10 ps) there is strong resemblance to the spectral evolution observed upon excitation at 530 nm: Delays earlier than 10 ps exhibit fast spectral dynamics associated with the nuclear relaxation of the singlet excited state. An analysis similar to that described above was used to isolate SE spectral dynamics, and the ultrafast red shift and intensity decay of the SE region were found to occur with lifetimes of 4.5 (Figure 3.4S(b)) and 4.3 ps (Figure 3.4S(c)), respectively.

Despite similarities with the dynamics observed with lower excitation energies, a new, broad feature centered near 620 nm emerges concurrently with the decay of the STA signal on longer timescales when *trans*-4TCE is excited at 420 nm. Based on similarity to the photoinduced absorption spectra of related oligothiophenes at similar time delays following photoexcitation,[32,44,45] we ascribe this broad feature to a triplet transient absorption (TTA, $T_1 \rightarrow T_N$) of 4TCE. Excited-state decay by way of ISC therefore is apparent from an isosbestic point at 665 nm that appears between 10 and 215 ps. A global kinetic analysis of spectra collected between these delays reveals that the relaxed singlet excited state has a 40.0 ps lifetime (Figure 3.5S) as a result of competing ISC and partial GSB recovery (i.e. internal conversion, IC). After 215 ps the TTA signal decays slightly and by 1500 ps the long-lived signal is a combination of TTA and GSB.

On even longer timescales (up to 5.5 ns) the TTA intensity and the GSB intensity do not change noticeably (Figure 3.9S(a)).

Spectral dynamics observed following 530 and 420 nm excitation of *trans*-4TCE are representative of two distinct excited-state relaxation behaviors; a transition between these two behaviors is observed as the pump pulse is tuned from the visible to the near UV, as illustrated in Figure 3.10S.

Table 3.1. Lifetimes from best-fit decay models for 4TCE excited at 420 and 530 nm

Isomer	Excitation λ (nm)	Fitting Content[a]	τ_1 (ps)	τ_2 (ps)
trans	530	510 nm (GSB)		39.2
		600 nm (SE)	2.3	37.0
		740 nm (STA)	2.9	38.6
		Red shift of SE	7.0	
		Global fit to decay of all species[b]		40.0
	420	Red shift of SE	4.5	
		SE intensity decease	4.3	
		Global fit of STA to TTA conversion[c]		40.0
cis	530	452 nm (STA 2)	4.8	
		700 nm (STA 1)	0.38	17.1
	420	472 nm (STA 2)	3.6	
		Global fit of TTA to *trans* S_0 conversion[d]		396

a. Wavelengths designate specific time-dependent cuts through transients.
b. Global fitting was applied to all transients at times > 10 ps.
c. Global fitting was applied to all transients between 10 and 215 ps.
d. Global fitting was applied to all transients between 316 and 1500 ps.

3.3.2. Photoinduced dynamics of *cis*-4TCE.

3.3.2.1 Low-energy excitation of *cis*-4TCE (530 nm).

Figure 3.3(a) shows the TA spectra of *cis*-4TCE following 530-nm excitation. The position of most spectral features are similar to those observed for the *trans* isomer, with evidence for ground-state bleaching below 575 nm, stimulated emission near 600 nm, and excited-state absorption above 650 nm. In addition, a second intense excited-state absorption band appears below 475 nm (STA 2), and overlaps significantly with the region where we anticipate the appearance of *cis*-4TCE GSB.

Spectra collected at early delays (t = 0.8 to 5.0 ps) reveal a blue shift as well as a rapid decay of STA 2. Additionally, the STA1 and GSB/SE features are observed to decay much more significantly during the first 10 ps than what is observed for *trans*-4TCE. All transient features decay within 300 ps. Fitting the intensity decay of STA1 at a single wavelength (700 nm) to a biexponential model gives two timescales: 0.38 and 17.1 ps (Figure 3.7S). A single exponential fit of the 452 nm trace gives a 4.8 ps decay constant (Figure 3.6S); the SE band, which is partially overlapped with the lower-energy absorption band, STA 1, undergoes a red shift from 580 to 620 nm on a similar timescale. In total, the ultrafast spectral relaxation of *cis*-4TCE occurs on somewhat faster timescales than observed for relaxation of the *trans* isomer at the same pump wavelength. However, only a very small permanent bleach (<~2% compared to the initial GSB intensity) persists at long time delays for the *cis* isomer, meaning that photoinduced isomerization is considerably less favored at 530 nm excitation relative to the *trans* isomer.

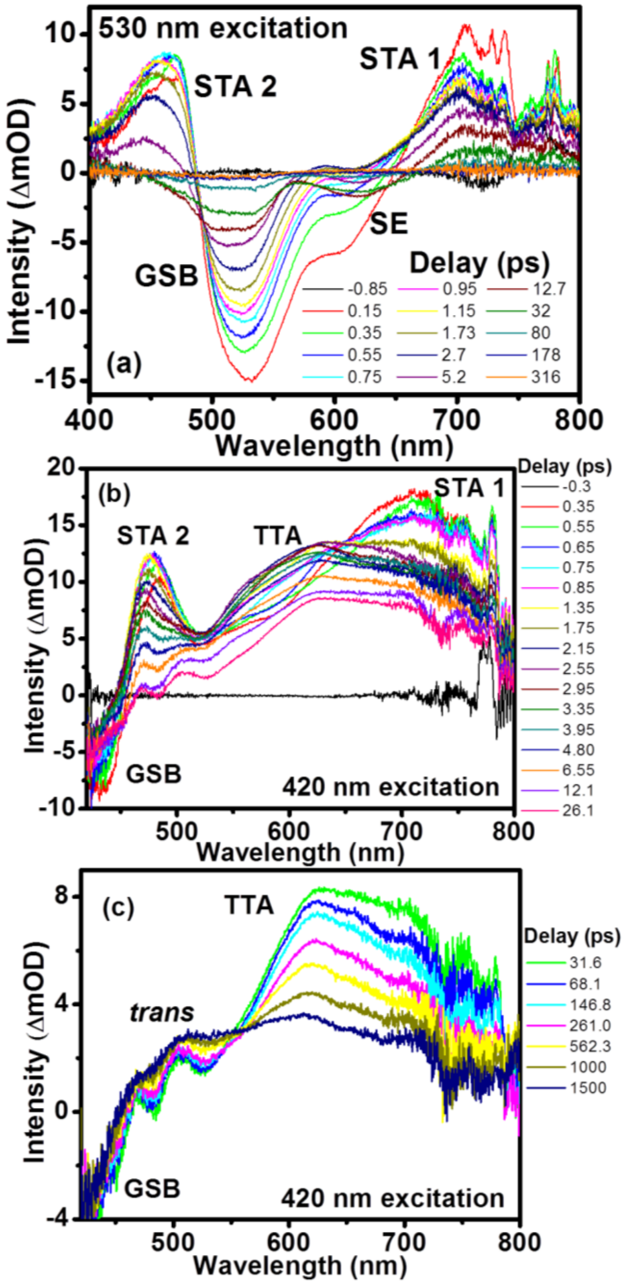

Figure 3.3. (a) TA spectra of *cis*-4TCE in chlorobenzene following 530-nm excitation: Spectral dynamics are similar to those observed for the *trans* isomer, but exhibit negligible signatures of isomerization. TA spectra of *cis*-4TCE in chlorobenzene excited at 420 nm (b) ~0-30 ps and (c) after 30-1500 ps. (b) Ultrafast ISC occurs in the first 2 ps, with a decay of STA 1 at 720 nm and an appearance of TTA at 620 nm. (c) From 30 to 1500 ps the intensity of TTA is substantially reduced, while absorption of the S_0 *trans* isomer concurrently appears between 450 and 560 nm. This *cis*-to-*trans* ISC is evidenced by the isosbestic point at 556 nm.

3.3.2.2 High-energy excitation (420 nm).

TA spectra of *cis*-4TCE excited at 420 nm are presented in Figures 3.3(b) and 3.3(c). Transient spectra collected at early time delays (Figure 3.3(b)) are characterized by a broad, intense excited-state absorption (STA 1) peaking at 720 nm and a narrow positive feature at higher energies (475 nm, STA 2); these features are similar to those observed with 530-nm excitation, but obscure the negative GSB and SE signals anticipated between 500 and 600 nm (although GSB can be seen below 450 nm).

Spectral dynamics during the first 26 ps can be explained as follows: Absorption around 720 nm (STA 1) undergoes a fast decay with concomitant appearance of a feature centered at 620 nm within the first 2 ps. The shape and peak position of the resultant spectrum is similar to what is observed following ISC of excited *trans*-4TCE and small oligothiophenes, indicating that high-energy excitation of *cis*-4TCE likewise leads to ISC, but on a considerably faster timescale. The assignment of this dynamic to ultrafast ISC is supported by the appearance of a quasi-isosbestic point near 665 nm. Meanwhile, STA 2 exhibits a rapid decay, similar to what is observed following excitation at 530 nm, with the peak position of STA 2 red shifting to 472 nm in the first few hundred femtoseconds. By fitting the 472 nm trace intensity with a single exponential decay function, we obtain a decay lifetime of 3.6 ps (Figure 3.6S). By 12 ps STA 2 has vanished, leaving the broad absorption above and a negative GSB below 450 nm. On a similar timescale the absorption between 460 and 800 nm exhibits a slight decay in intensity.

Over the next nanosecond (Figure 3.3(c)) the absorption band peaking at 620 nm decays significantly, while the spectral intensity between 466 and 556 nm increases. An isosbestic point appears at 556 nm during this time regime, implying that the nascent triplet relaxes to yet another state. As the spectrum of *trans*-4TCE (Figure 3.1) and its difference spectrum with the *cis* isomer (Figure 3.10S) peak between 450 and 560 nm, the intensity increase below the isosbestic point indicates the formation of the ground-state *trans* isomer through ISC from the T_1 state. A global fit with a sequential two-state kinetic model from 30 to 1500 ps reveals a 0.4 ns timescale for this process (Figure 3.8S). By 1500 ps the transient spectrum includes TTA absorption overlapped with the residual GSB below 450 nm and the absorption from the newly-formed S_0 *trans*-4TCE. Nanosecond measurements up to 5.5 ns (Figure 3.9S(b)) reveal similar evolution as observed with *trans*-4TCE and no GSB recovery on this longer timescale.

Spectral dynamics observed following excitation at intermediate wavelengths exhibit a combination of the spectral dynamics observed with 420 and 530 nm, as illustrated in Figure 3.11S. Only excitation wavelengths shorter than 440 nm produce the long-lived TTA and GSB signals apparent in Figure 3.3, indicating that some portion of the excited *cis* molecules have transferred into the triplet manifold at this energy and are unable to internally convert to the *cis* ground-state. This roughly matches the onset wavelength we previously observed for *cis*-to-*trans* photoconversion to a photostationary state.

3.3.3. Triplet-sensitized energy transfer.

In order to verify that *cis*-to-*trans* isomerization occurs via the triplet manifold, we used methylene blue (MB, $\Phi_{ISC}= 0.52$)[46] as a sensitizer to prepare T_1 4TCE. These measurements were conducted with 4TCE in acetonitrile, as MB has poor solubility in

CB. The steady-state UV-Vis absorption of MB is most intense at 650 nm, which lies at significantly lower energy than the lowest-energy absorption band of either *trans*- or *cis*-4TCE. Furthermore, the T_1-S_0 energy gap of both 4TCE isomers is calculated to be lower than that of MB (Table 3.2). Therefore, we expect that effective triplet energy transfer from MB to 4TCE is possible for both isomers.

Table 3.2. Experimental and calculated energies of S_0-S_1 and S_0-T_1 energy gaps for 4TCE and MB (unit: eV).

	S_0-S_1 (exp.)	S_0-S_1 (calc.)[a]	S_0-T_1 (exp.)	S_0-T_1 (calc.)[a]
cis-4TCE[b]	2.64	2.86		1.27
trans-4TCE[b]	2.38	2.60		1.11
MB	1.89[b] / 1.86[c]		1.43[c]	

a Vertical excitation energy calculation (TD-DFT/CAM-B3LYP/6-31G*/PCM)

b from UV-vis spectrum in acetonitrile

c "in polar solvent," taken from ref. 46

Experimentally, a mixture of *cis*-4TCE and MB in acetonitrile (not deoxygenated) was exposed to 650-nm light. Within 8 minutes isomerization from *cis* to *trans* was clearly observed via steady-state UV-Vis spectroscopy, as evidenced by the appearance of an isosbestic point at 435 nm (Figure 3.4(a)). The intensity of MB absorption centered at 650 nm was also observed to decrease, most likely the result of some oxidation of MB in solution. Triplet sensitization of the isomerization of *trans*-4TCE was attempted in the same way, but no spectral change associated with *trans*-to-*cis* isomerization was observed upon 650-nm radiation (Figure 3.4(b)).

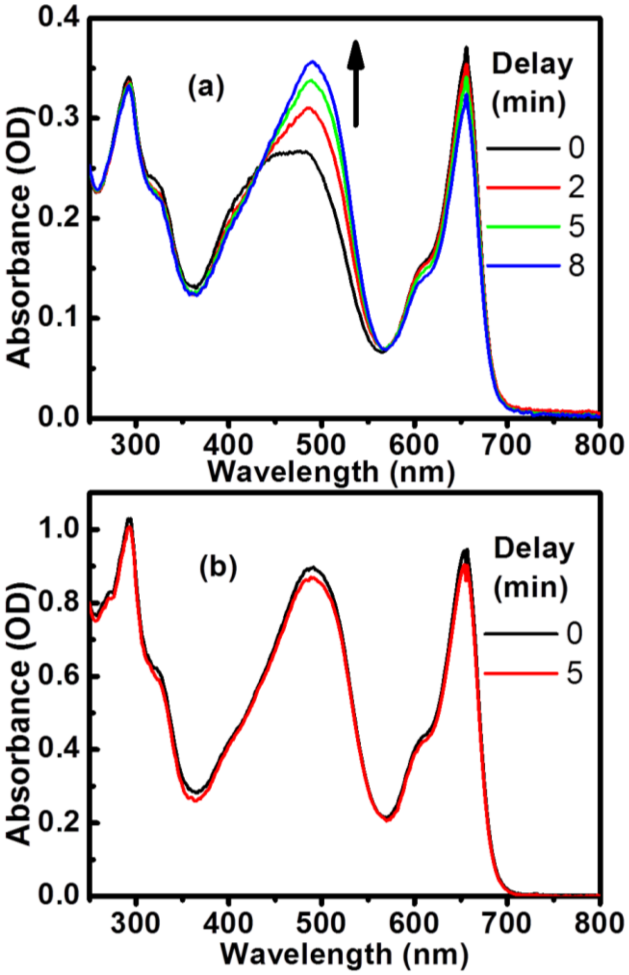

Figure 3.4. Evolution of UV-vis spectra recorded during 650 nm light illumination (I = 2.6 mW) of (a) *cis*-4TCE (c = 2.2×10^{-5} M) and methylene blue (MB, c = 4.6×10^{-6} M) and (b) trans-4TCE (c = 3.2×10^{-5} M) and MB (c = 1.2×10^{-5} M) in acetonitrile. Neither solution was degased.

3.3.4. Computational results.

The *trans* isomer is ca. 4 kcal/mol more energetically stable than *cis*-4TCE; the relative stability of *cis* over *trans* under room-light illumination is related to the relative intensities and positions of their respective steady-state absorption features, as well as the relative quantum yields for photoisomerization with visible light. The calculated vertical transition to the S_1 state is 2.60 eV (oscillator strength f = 1.43) for *trans* and 2.86 eV (f =

0.67) for *cis*. The difference in calculated transition energies for the two isomers (0.26 eV) matches the differences measured experimentally (also 0.26 eV). Furthermore, the ratio of calculated oscillator strengths (2.13) is also in reasonable accord with experiment (2.4 based on peak intensities). This disparity in oscillator strength means that *trans* can more effectively absorb visible light.

In the TA spectra for both *trans* and *cis* the SE peaks near 600 nm. The SE peak reflects the vertical energy gap from the first excited state back to the ground state. Stationary minima were located for the S_1 state of both isomers and calculated energies are collected in Table 3.1S. During the relaxation of the *trans* isomer in the first excited state, elongation of the ethylene bond length from 1.373 to 1.447 Å and increase of the central dihedral angle θ (C(cyano)-C(et) -C(et)- C(cyano)) to 36^o render an energy decrease by 0.44 eV. Similarly in *cis*, the ethylene bond length alters from 1.366 to 1.452 Å and θ changes from 175^o to 139^o with a 0.77 eV energy decrease during the relaxation. Accordingly, the S_0-S_1 gap shrinks, giving rise to the red shift of SE observed in the TA spectra. This relaxation may also alter the S_1-S_n gaps as well, and likely explains the time-dependence in the STA2 position for *cis*-4TCE. The calculated energy gap between the Franck-Condon region (S_1^*) and S_1 minimum is in qualitative accord with the observation of spectral relaxation of SE observed for both isomers.

TD-DFT calculations were used to predict the higher-lying bright states in the singlet manifold: S_6 (f = 0.43) for *trans*, S_2 (f = 0.50) and S_4 (f = 0.17) for *cis* (Figure 3.5). TD-DFT calculations also predict the relative position and intensity of TTA signals: For the *trans* isomer the strongest absorption is $T_1 \rightarrow T_3$ at 578 nm (f = 1.19), and in *cis* it is $T_1 \rightarrow T_3$ at 571 nm (f = 0.43); these are in close agreement the features assigned to TTA from experimental measurements. In order to explore the density of triplet levels relevant at various excitation energies, the energies of various triplet states were calculated at the S_1 equilibrium geometry; 8 and 7 triplet excited states were found to lay between S_1/S_6 for *trans*- and S_1/S_4 for *cis*-4TCE, respectively.

In order to better understand why isomerization might proceed via the T_1 level, we also carried out relaxed PES scans of the S_0 and T_1 states; the results are plotted in Figure 3.5. Most importantly, these two potential curves intersect near θ = 90°. The PES of S_0 exhibits a 1.2 eV barrier at the perpendicular geometry, while the T_1 surface is found to be barrierless from the Franck-Condon region to the S_0/T_1 crossing along this particular coordinate. Notably, the relaxed T_1 PES slightly favors (is flatter towards) smaller dihedral angles, closer to the *trans* well of the S_0 surface.

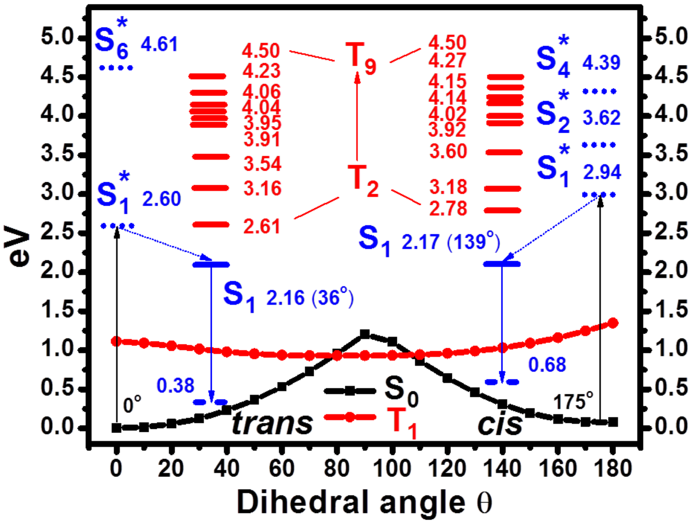

Figure 3.5. Diagram of calculated state energies for 4TCE. Energies of singlet excited states are evaluated at the optimized ground-state geometry. The S_1 geometries of both isomers were also optimized; high-lying triplet levels were calculated from the S_1 minimum geometries. Although isomerization likely involves multiple coordinates, the dihedral angle of the central ethylene is anticipated to be significant. Relaxed PES scans of S_0 and T_1 were performed in steps of 10 deg. These two potential curves intersect near θ = 90°.

3.4. Discussion

3.4.1 Energy-dependent relaxation pathways and photoswitching mechanisms.

Based on the spectral dynamics presented above, we summarize the excited-state relaxation following 530-nm photoexcitation as shown in Figure 3.6(a): Excitation of *trans*-4TCE to its S_1 state at this wavelength results in excited-state relaxation on a timescale of 3-7 ps; this is followed by S_1 decay on a timescale of 40 ps that returns 88% of the excited-state population to S_0 *trans*-4TCE while the remaining 12% isomerizes to S_0 *cis*-4TCE.

Excitation of *cis*-4TCE at 530 nm is likewise followed by excited-state relaxation on a timescale of a few picoseconds. The rapid decrease of the ground-state bleach on the timescale associated with nuclear relaxation of the excited state indicates that internal conversion back to the ground state is highly structure dependent. In total, S_1 *cis*-4TCE decays via internal conversion to the *cis* ground state, with virtually no isomerization to *trans*-4TCE (<2%).

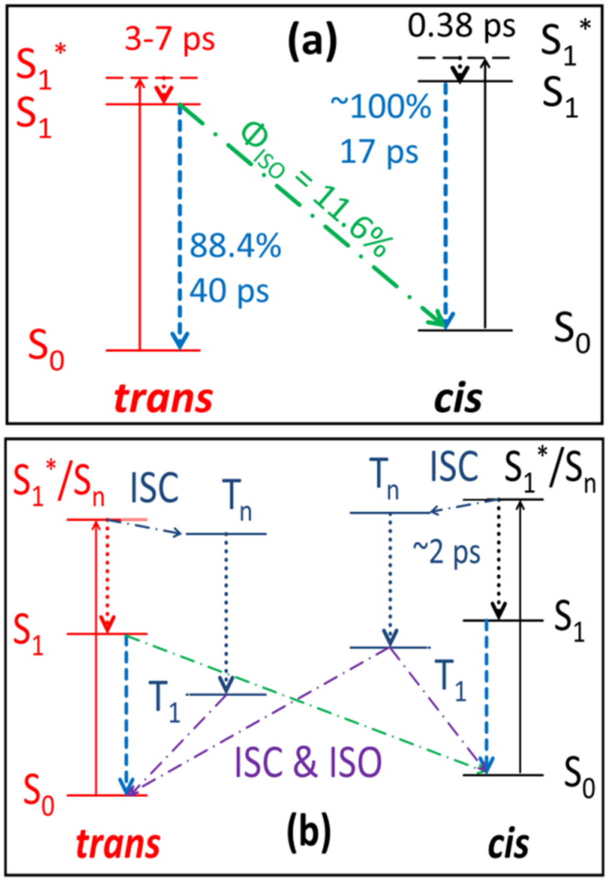

(a)
3-7 ps
S_1^*
S_1
S_0
88.4%
40 ps
$\varnothing_{ISO} = 11.6\%$
0.38 ps
~100%
17 ps
S_1^*
S_1
S_0
trans
cis
(b)
S_1^*/S_n
ISC
T_n
S_1
T_1
S_0
trans
ISC & ISO
T_n
ISC
S_1^*/S_n
~2 ps
S_1
T_1
S_0
cis

Figure 3.6. Schematic of isomerization pathways for 4TCE excited at (a) 530 nm and (b) 420 nm. For 530 nm excitation 11.6% of S_1 *trans* isomer undergoes isomerization to *cis*. For 420 nm excitation the relaxation for both isomers occurs in the triplet manifold. Ultrafast ISC (~2 ps) occurs in *cis*-4TCE, and *cis*-to-*trans* isomerization occurs through the T_1/S_0 coupling on a timescale of 0.4 ns.

Excited-state relaxation pathways following excitation at 420 nm are shown schematically in Figure 3.6(b) for both isomers. Excitation of *trans*-4TCE at this energy results in population of S_1 with considerable excess vibrational energy. Excited-state relaxation occurs on a timescale of 3-7 ps, similar to what is observed at lower energies. This is followed by excited-state decay on a timescale of 40 ps that results in a partial recovery of the *trans* ground state as well as intersystem crossing into the triplet manifold of 4TCE. We see no evidence for *trans*-to-*cis* isomerization from time-resolved measurements up to 5.5 ns. We note that this timescales is considerably longer than timescales for vibrational energy relaxation and transfer in solution, and therefore the triplet spectrum observed corresponds with a relaxed T_1. Triplet sensitizer measurements further suggest that isomerization only occurs via the singlet manifold for *trans*-4TCE. As both excitation pathways are expected to create T_1 with relatively little excess internal energy, we take both pieces of data to imply that *trans*-to-*cis* isomerization does not occur by way of the triplet manifold.

Excitation of *cis*-4TCE at the same energy reveals that a significant fraction of the population of photoexcited molecules undergoes ultrafast (~2 ps) intersystem crossing into the triplet manifold, with the remaining singlet excited 4TCE relaxing in a manner similar to *cis*-4TCE excited at 530 nm. A fraction of the triplet population relaxes to S_0 *trans*-4TCE on a 400 ps timescale, with the remaining triplet population persisting beyond 5 ns.

This interpretation of photophysical relaxation pathways based on our ultrafast spectral measurements is highly consistent with the wavelength-dependent isomerization yields observed for 4TCE. The following equation reflects the relationships that controls photoconversion,[47]

$$\frac{[t]}{[c]} = \frac{Y^{ct} \times \varepsilon_c}{Y^{tc} \times \varepsilon_t} \tag{3.1}$$

where [t] and [c] denote the concentration of *trans* and *cis* in the photostationary state (PSS), Y^{ct} and Y^{tc} are the quantum yields for the *cis*-to-*trans* and *trans*-to-*cis* isomerization reaction, respectively, and the extinction coefficients of *cis* and *trans* are represented by ε_c and ε_t. Thus, at 530 nm pump wavelength Y^{ct} is <2% while Y^{tc} = 11.6 ± 1.4%, meaning that the photoisomerization from *trans* to *cis* proceeds with nearly 100% efficiency. Meanwhile, the reverse reaction can be triggered by pumping at 420 nm; at this wavelength $\varepsilon_c/\varepsilon_t = 1.6$ and Y^{ct} and Y^{tc} are estimated as 4.68 ± 0.24% and 23.0 ± 1.5%, respectively (see supporting material). Relaxation of *cis*-4TCE by way of the triplet manifold therefore enables *cis*-to-*trans* isomerization with a large enough quantum yield to enable the build-up of a significant concentration of *trans*-4TCE at the PSS. We note, however, that the photostationary yields obtained are solvent dependent (0.3 for CB, 0.6 for toluene), which reflects differences in the relative stabilization of singlet vs. triplet levels that affect the ISC dynamics into and out of the triplet manifold.[48-50] Further work is underway to interrogate this solvent-dependent effect, as it represents a means for controlling relative isomerization yields and switch performance.

3.4.2 Photoisomerization of 4TCE through the triplet manifold.

3.4.2.1 Singlet-to-triplet intersystem crossing in 4TCE.

It is well known that short oligothiophenes have relatively fast ISC kinetics,[32-37] primarily due to the large spin-orbit coupling (SOC) induced by sulfur atoms. Large SOCs also can be expected for excited 4TCE, such that ISC will to be an important photophysical relaxation pathway for 4TCE. An important question regarding ISC relaxation is what gateway states are critical for quickly relaxing between the singlet and triplet manifolds. NTO analysis reveals that S_1, $T_{1\text{-}2}$ for both isomers evaluated at the optimized S_1 geometries, and S_6 (*trans*), S_2 and S_4 (*cis*) evaluated at the optimized S_0 geometries all exhibit π-π^* character (see supporting material). Therefore, ISC from the

S_1 level to these triplet states are less likely according to the El-Sayed rule.[51] This is in excellent agreement with our experimental findings that no triplet signals were observed at long time delays when pumping at the red side of the low energy absorption bands (530 nm). Higher-lying excited states are rather complicated and higher-level theoretical calculations are required to better understand the ultrafast ISC pathways that contribute following excitation at higher energies. Nonetheless, triplet excited states with large SOC are found 1.5-2.5 eV above the lowest singlet state in related oligothiophenes.[52] Additionally, these triplet states have been assigned as quasi-pure π-σ^* excitations that can enable efficient ISC in heterocyclic compounds.[53,54] We infer that a similar situation exists for photoexcited 4TCE, and would thus facilitate ISC when 4TCE is pumped into higher-lying singlet excited state(s) that are energetically close to triplet states with quasi-pure π-σ^* character. Wavelength-dependent transient absorption spectra collected at 1 ns for *trans* and 316 ps for *cis* strongly support this hypothesis (Figures 3.10S and 3.11S(b), respectively).

The fact that *cis*-4TCE exhibits a larger ISC rate than the *trans* isomer can be rationalized through comparisons with oligothiophenes of various lengths. By comparing the photodetachment spectroscopy of oligothiophene anions with the phosphorescence and STA of bi- (2T), ter- (3T) and quarter- (4T) thiophene, Rentsch *et al*. determined that the relative positions of the S_1 and high-lying triplet levels underlie the extremely high ISC rate observed for 2T when excited to the lowest singlet excited state and the decrease in this rate with increase in oligomer.[36] Beljonne *et al*. argued that lengthening an oligothiophene should decrease the SOC, since it could enlarge the energetic separation between the π and σ electronic structures and consequently reduce spin-orbit interactions.[52] The effective conjugation length in *cis*-4TCE must be shorter than that in *trans*, as a result of its highly nonplanar configuration; therefore, *cis* is more similar to smaller oligothiophenes (e.g. 2T or 3T), whereas *trans* is analogous to longer oligothiophenes (e.g. 4T or 5T). As a result, *cis* could be expected to have a higher ISC rate, as observed via 420-nm photoexcitation. Similarly, the ultrafast ISC (~2 ps) as well as the trend between pump energy and the triplet quantum yield in *cis*-4TCE is highly similar to what has been observed with 2T and 3T.[35,37] Paa et al. associated the ultrafast ISC of 3T on a ~2 ps timescale to the excited-state structural relaxation, as ISC is more favorable from the unrelaxed, non-planar excited vibronic singlet state. The triplet yield for 3T, as well as the 2 ps ultrafast decay component, becomes more prominent when the pump energy increases.[35,37] This is similar to what we observe for *cis*-4TCE. In contrast, *trans*-4TCE exhibits a much slower ISC timescale, which is consistent with the ISC of longer oligothiophenes.

The twisted conformation of *cis*-4TCE plays an important role in promoting ultrafast ISC, and therefore points to a structure-dynamics relationship that critically underlies the *cis*-to-*trans* isomerization pathway of this photoswitch. According to the symmetry selection rules for ISC, lower symmetry of an oligothiophene can strongly increase the SOC.[52] The planar conformation of the *trans* isomer can largely enhance the S_0-S_1 transition in the visible region, but would also impede ISC, even if the conjugated backbone contains heavy atoms. As a result, while longer effective conjugation length is attractive for the design of 4TCE derivatives because it can push the absorption transition that enables *trans*-to-*cis* isomerization further into the red, intramolecular interactions that maintain an effectively shorter conjugation length should be concurrently maintained in order to promote the reverse isomerization through excitation at higher energies to enable efficient ISC into the triplet manifold.

3.4.2.2 Triplet isomerization of cis-4TCE.

As with oligothiophenes, it can be presumed that 4TCE will undergo fast internal conversion through the dense manifold of triplet states once it crosses into the triplet manifold, quickly relaxing to the T_1 state. Isomerization or ground-state recovery must then occur via ISC from the lowest triplet level. The relaxed PES scan along the θ coordinate (Figure 3.5) indicates that the PES of T_1 has a flat minimum that is nearly perpendicular and slightly favors a configuration that falls within the *trans* ground-state well. Although the photoinduced excited-state dynamics need not follow this calculated pathway exactly, this observation helps to explain the observation of *cis*-to-*trans* but not *trans*-to-*cis* isomerization by way of triplet manifold. The T_1 PES also crosses the S_0 surface at nearly perpendicular geometries, which should greatly enhance the probability for isomerization via ISC when an excited-state wavefunction or wavepacket is able to approach the crossing. In fact, the T_1/S_0 SOC calculated at the $\theta=90$ geometry has a substantial value of 59.83 cm^{-1}, which is significantly larger than those of planar aromatic compounds (typically less than 1 cm^{-1}).[55] Therefore it is conceivable that T_1 4TCE could readily return to the singlet manifold through ISC on a sub-ns timescale.[56,57]

The conclusion that *cis*-to-*trans* photoisomerization occurs by way of the triplet manifold (whereas *trans*-to-*cis* isomerization does not) is further corroborated by triplet energy-transfer experiments. Conspicuously, excitation of MB at 650 nm induces *cis*-4TCE to isomerize, whereas the reverse isomerization under the same condition is not observed. More detailed interrogation with regards to the type and relative concentration of triplet sensitizer is certainly necessary to elucidate the generality of the triplet sensitization of 4TCE. However, sensitizer experiments raise interesting possibilities for future molecular design or applications with 4TCE derivatives: Specifically, one could conceivably combine the isomerizing moiety with a sensitizing group; this could enable shifting the wavelengths for *cis* to *trans* isomerization into redder spectral regions (Figure 3.4).[58,59] As demonstrated with MB, the triplet energy transfer to *cis*-4TCE is highly effective and far more photoselective that direct excitation of this isomer at bluer wavelengths: The formation of the *trans* isomer can be detected within a few minutes of radiation with 650-nm light, even in the presence of oxygen; this is similar to the timescale necessary to reach the PSS via direct excitation at 420 nm. Although the presence of oxygen has the potential to quench excited triplet sensitizers, we expect that *cis* to *trans* isomerization itself is efficient following energy transfer because isomerization is complete within a nanosecond, as observed following photoexcitation of *cis*-4TCE at 420 nm.

3.5. Conclusions

4TCE is an attractive switch for applications that require E/Z isomerization upon visible light irradiation and also exhibits an interesting and potentially exploitable exclusivity in its forward and reverse photoisomerization mechanisms: Upon photoexcitation with wavelengths longer than 460 nm, isomerization in 4TCE occurs exclusively from *trans* to *cis* and only involves electronic relaxation within the singlet manifold. In contrast, *cis*-to-*trans* isomerization can be achieved by irradiation at wavelengths < 460 nm, whereby the photoprepared state undergoes fast ISC into the triplet manifold and then isomerizes from the lowest triplet level within 1 ns; this pathway is possible due to large spin-orbit coupling common to short oligothiophenes and thiophene-based systems. In addition, triplet energy-transfer can be used to induce *cis* to *trans* isomerization, but not the reverse. Thus, the switching state can be selectively controlled by illumination at different visible wavelengths, but can also be selectively discriminated through indirect sensitization.

This separation of isomerization mechanisms between manifolds of different multiplicity has important implications for tailoring switch design: For instance, elongation of the effective conjugation of 4TCE derivatives by lengthening the pendant oligothienyl groups is an intriguing strategy for generating E/Z photoswitches that operate at even longer wavelengths. However, this design strategy must also take into consideration how the fast ISC process underlying the *cis*-to-*trans* isomerization pathway is altered with increased conjugation length; notably, related oligothiophenes exhibit slower ISC rates with increasing conjugation length. Therefore, it may be necessary to introduce a slightly twisted torsional conformation between thiophene rings through the addition of pendant substituents in order to maintain an efficient, ultrafast ISC[60] while increasing the length of the pendant oligothienyl groups. Alternatively, elongation of the oligothienyl groups could be used to squelch *cis*-to-*trans* photoisomerization, enabling unidirectional light-activated structural changes, as may be desired for the preparation of spatially patterned material morphologies. This separation of forward and reverse isomerization pathways could also lend itself to control with variation in chemical or physical environment (e.g. variations in solvent/matrix properties or presence of electric fields). Finally, incorporation of a triplet-sensitizing moiety into 4TCE derivatives has the potential to improve the selectivity of *cis* to *trans* isomerization, accompanied with a substantial red shift of the corresponding isomerization wavelength. As demonstrated here, the efficacy of all of these possibilities rests on the structure-dynamics relationships that control the photophysical dynamics underlying each photoisomerization mechanism.

3.6. Supporting material

3.6.1. Measurement of isomerization quantum yields at 420 nm

A $trans \leftrightarrow cis$ model was adopted for determination of isomerization quantum yields according to the time-evolution towards a photostationary state upon irradiation at 420 nm.[61,62]

$$\frac{d\chi_t}{dt} = k_{ct} \cdot \chi_c - k_{tc} \cdot \chi_t \tag{3.2}$$

$$\frac{k_{ct}}{k_{tc}} = \frac{Il(1 - 10^{-A(t)})}{VA(t)} \cdot \frac{Y^{ct}}{Y^{tc}} \cdot \frac{\varepsilon_c}{\varepsilon_t} \tag{3.3}$$

The definitions and units of all symbols are listed below.

χ_t, χ_c : Molar fractions of *trans* and *cis*, respectively

k_{tc}, k_{ct} : Rate for the $trans \rightarrow cis$ and $cis \rightarrow trans$ reaction, respectively (1/s)

I : Intensity of the incident light (E/s, determined by ferrioxalate actinometry, as described below)

l : Optical path length of the cuvette (cm)

A(t) : Time dependent sample absorbance at the excitation wavelength

Y^{tc}, Y^{tc}: Isomerization quantum yields for the $trans \rightarrow cis$ and $cis \rightarrow trans$ reactions, respectively

$\varepsilon_t, \varepsilon_c$: Extinction coefficients of the *trans* and *cis* isomer at the excitation wavelength, respectively (M^{-1} cm^{-1})

V: Volume of the irradiated solution (L)

At the photostationary state (PSS) $d\chi_t/dt = 0$, and thus

$$\frac{Y^{tc}}{Y^{ct}} = \frac{(1 - \chi_{t,\infty})\varepsilon_c}{\chi_{t,\infty}\varepsilon_t} \tag{3.4}$$

where $\chi_{t,\infty}$ is the *trans* molar fraction at the PSS. Integrating equation (2) with the initial condition $\chi_t(t = 0) = \chi_{t,0}$ and substitutions of equation (3) and (4) give

$$\chi_t\big(x(t)\big) = \big(\chi_{t,0} - \chi_{t,\infty}\big)\exp\left(-\frac{x(t)}{t_1}\right) + \chi_{t,\infty} \tag{3.5}$$

$$x(t) = \int_0^t \frac{(1 - 10^{-A(t)})}{A(t)}\,dt \tag{3.6}$$

$$\frac{1}{t_1} = \frac{IlY^{ct}\varepsilon_c}{V\chi_{t,\infty}} \tag{3.7}$$

where $x(t)$ represents the integrated photokinetic factor and $\chi_t\big(x(t)\big)$ is the time-dependent molar fraction of the *trans* isomer.

In our quantum yield measurement, 3 mL of *cis*-4TCE dissolved in chlorobenzene (CB) was placed in a 10-mm pathlength cuvette and illuminated with 420-nm light while stirred. The time dependent UV-vis spectrum was recorded every 30 s in the first 6 min and less frequently up to 30 min, long enough to capture the isomerization kinetics. The spectra exhibit an isosbestic point at 449 nm. $\chi_t\big(x(t)\big)$ was determined by least-squares fitting from 400 to 650 nm with the pure *trans* and *cis* UV-vis spectra. $x(t)$ was calculated by numerical integration. By fitting $\chi_t\big(x(t)\big)$ against $x(t)$ with an exponential function, the parameter t_1 and $\chi_{t,\infty}$ were determined as 634.3 ± 14.8 s and 0.286 ± 0.002, respectively (Figure 1S). The intensity of 420 nm light is $2.68 \times 10^{-9} \pm 0.12 \times 10^{-9}\ E/s$ measured by potassium ferrioxalate actinometry (vide infra). According to Equations (6) and (3), Y^{ct} and Y^{tc} were estimated as 4.68 ± 0.24% and 23.0 ± 1.5%, respectively, where the standard error was evaluated by propagation of uncertainty.

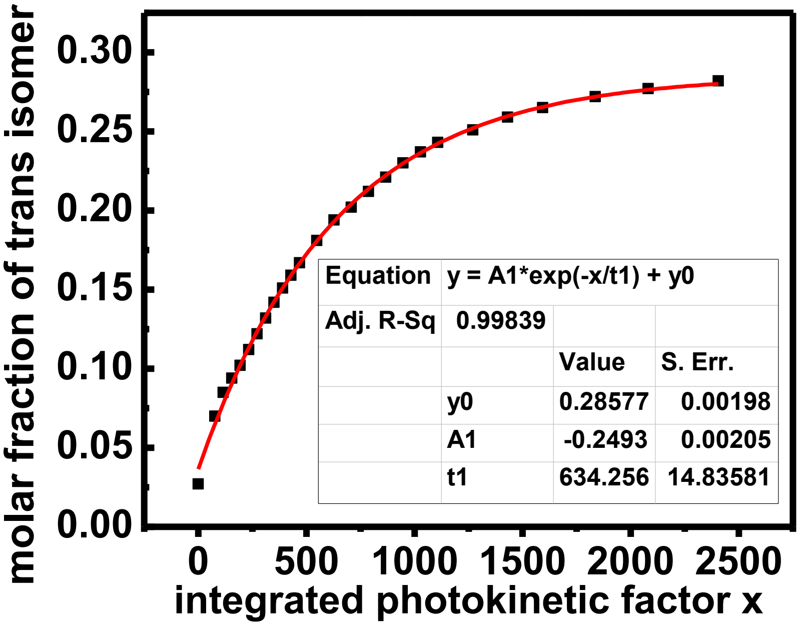

Figure 3.1S. Exponential fit of the *trans* molar fraction vs. the integrated photokinetic factor x.

3.6.2. Actinometry

We used potassium ferrioxalate actinometry to measure the intensity of our 420-nm light source for quantum yield measurements.[63] $K_3Fe(C_2O_4)_3 \cdot 3H_2O$ was synthesized in our lab according to the following procedure. First 14.0 g $K_2C_2O_4 \cdot H_2O$ and 12.5 g $FeCl_3$ were dissolved in 50 mL and 16.7 mL distilled water, respectively. Then two solutions were mixed together and the temperature was kept around 45^{o} C. The final product was obtained by recrystallization 3 times. 3 mL of a stirred $K_3Fe(C_2O_4)_3$ solution (0.016 M in 0.05 M H_2SO_4) was illuminated with 420-nm light for 20 s to 2 min. 0.5 mL of buffer solution (0.1 wt% phenanthroline in 0.5 M H_2SO_4 and 1.6 M NaOAc) was added afterwards and the absorbance at 510 nm was measured. A reference sample was prepared in the same way but was not exposed to the 420-nm light. The light intensity is calculated from the following equation[46]

$$I = \frac{\Delta A^{510\ nm} * 3.5\ mL}{\Delta t\ \phi^{420\ nm}\ \varepsilon^{510\ nm}} \tag{3.8}$$

where $\Delta A^{510\ nm}$ is the difference in absorbance of $\mathrm{Fe(phen)}_3^{2+}$ between sample and reference during an exposure time Δt, $\varepsilon^{510\ nm}$ = 11100 M^{-1} cm^{-1} is the extinction coefficient of $\mathrm{Fe(phen)}_3^{2+}$ at 510 nm, and $\phi^{420\ nm} = 1.12 \pm 0.01$.[63] The light intensity $I = 2.68 \times 10^{-9} \pm 0.12 \times 10^{-9}\ E/s$ was obtained by a series of 5 independent measurements and a linear regression fit.

3.6.3. Data acquisition of transient spectra

The actinic pump beam was blocked after the sample, and the probe beam was passed through a long-pass filter to remove scattered pump light. The probe was also passed through a bandpass filter in order to shape spectral intensity for detection. Probe light was collected and dispersed with a 300 mm spectrograph onto a CCD camera (Pixis-100BR, Princeton Instruments). The camera was configured to collect spectra at the laser's ~1 kHz repetition rate, with the pump and probe beams chopped at ~500 and ~250 Hz respectively to enable a two-chopper, four-phase data collection algorithm that could effectively discriminate against fluorescence and any residual actinic pump scatter from the transient absorption signal. Briefly, in each data acquisition cycle four spectra were taken consecutively: pump-on probe-on (1), pump-on probe-off (2), pump-off probe-on (3), and pump-off probe-off (4). The final fluorescence corrected TA spectrum was calculated as

$$\Delta\%T = \frac{(1) - (2)}{(3) - (4)}. \tag{3.8}$$

Each TA spectrum was an average of 30000 pumps on/off ratios.

3.6.4. Translation stage alignment

As drift in pump-probe overlap compromises the timescales extracted from measurements on a nanosecond timescale, all measurements were checked against the relaxation kinetics of various dyes. For example, a diluted Coumarin solution was excited by 400 nm actinic pump and its fluorescence-corrected stimulated emission (SE) spectrum was collected for delays up to 1.5 ns. The timescale observed for SE decay matched the fluorescence lifetime reported previously in the literature,[64] demonstrating that the drift in pump-probe overlap, particularly at long time delays, was negligible. Similar tests were done with longer pump wavelengths using other dyes (e.g. Rhodamine).

3.6.5. Fitting and comparison of GSB, SE and STA spectral dynamics in TAS of *trans*-4TCE following 530-nm photoexcitation

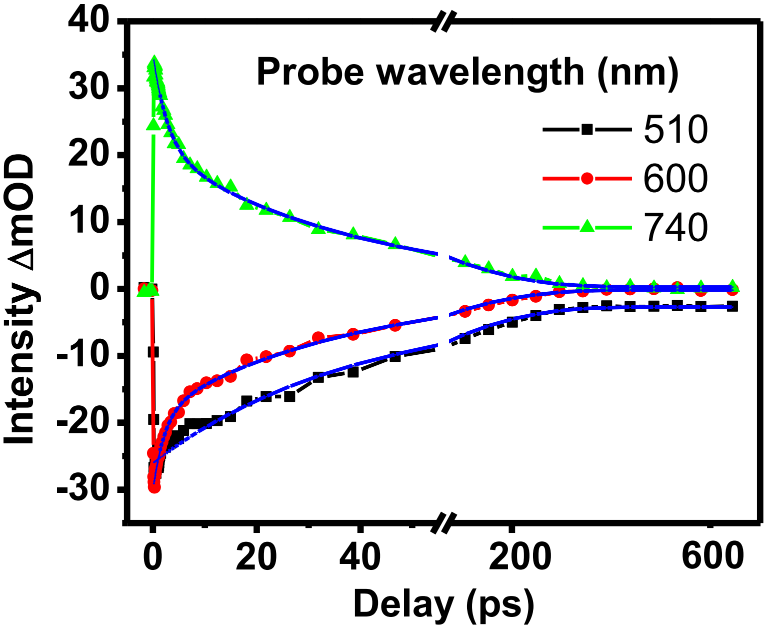

Figure 3.2S. Intensities at 600 and 740 nm are fitted with a biexponential function, exhibiting decay on both 2-3 ps and 38 ps timescales. GSB intensity at 510 nm recovers with a lifetime of 39.2 ps. Best-fit timescales for each trace are presented in Table 3.1 in the main text.

3.6.6. Separation of GSB and SE contributions to TAS of *trans*-4TCE photoexcited at 420 and 530 nm

The GSB and SE signals for *trans*-4TCE are significantly overlapped during the first 10 – 20 ps, which makes it difficult to characterize the SE spectral dynamics. The dynamic spectral shift of the SE band reflects the evolution in S_0-S_1 vertical energy gap between the Franck-Condon region and the excited-state minimum. In order to isolate the spectral dynamics of the SE, the following procedure was applied: The GSB spectrum was simulated using the shape of the *trans*-4TCE steady-state absorption band, scaled according to the intensity of the blue edge of the negative transient signal (determined by a least-squares fit from 466 to 534 nm between the GSB and the UV-vis spectrum of *trans*-4TCE), and subtracted from the transient spectra at each time delay (Figure 3.3S(a)). The weighted-average peak position between 550 to 630 nm was then calculated. Due to the weak SE intensity after 70 ps, the calculated peak position is not precise at the later time delays. A single exponential fit to the peak position in the first 70 ps gives a 7-ps time constant and a 9-nm red shift (Figure 3.4S(a)).

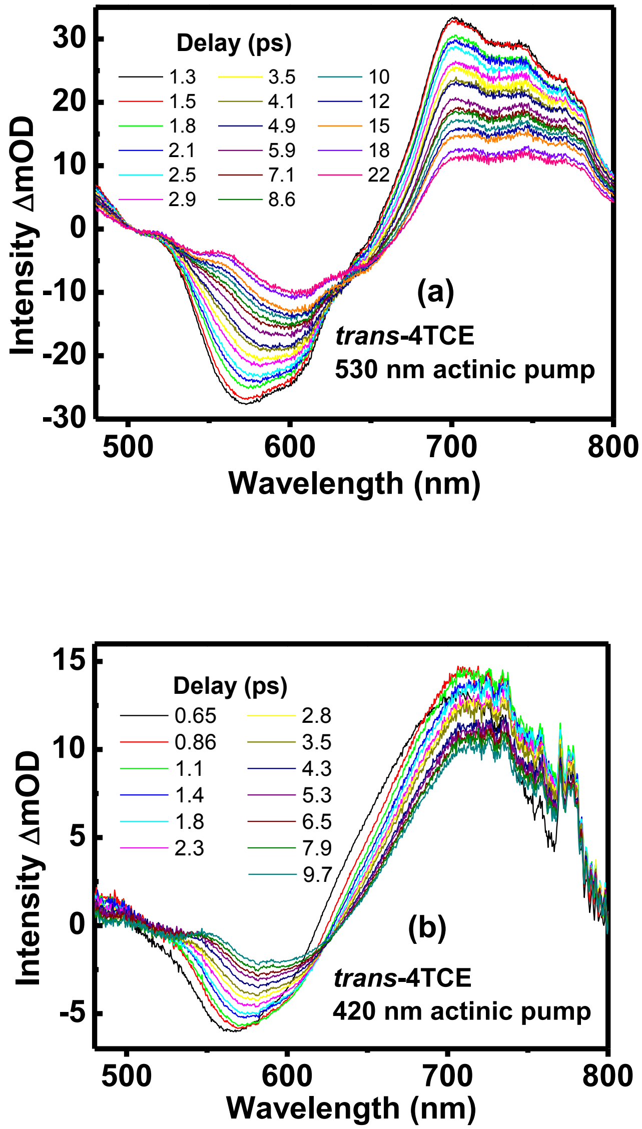

Figure 3.3S. TAS with the GSB components subtracted are shown in (a) and (b) for 530 nm and 420 nm excitation of *trans*-4TCE, respectively.

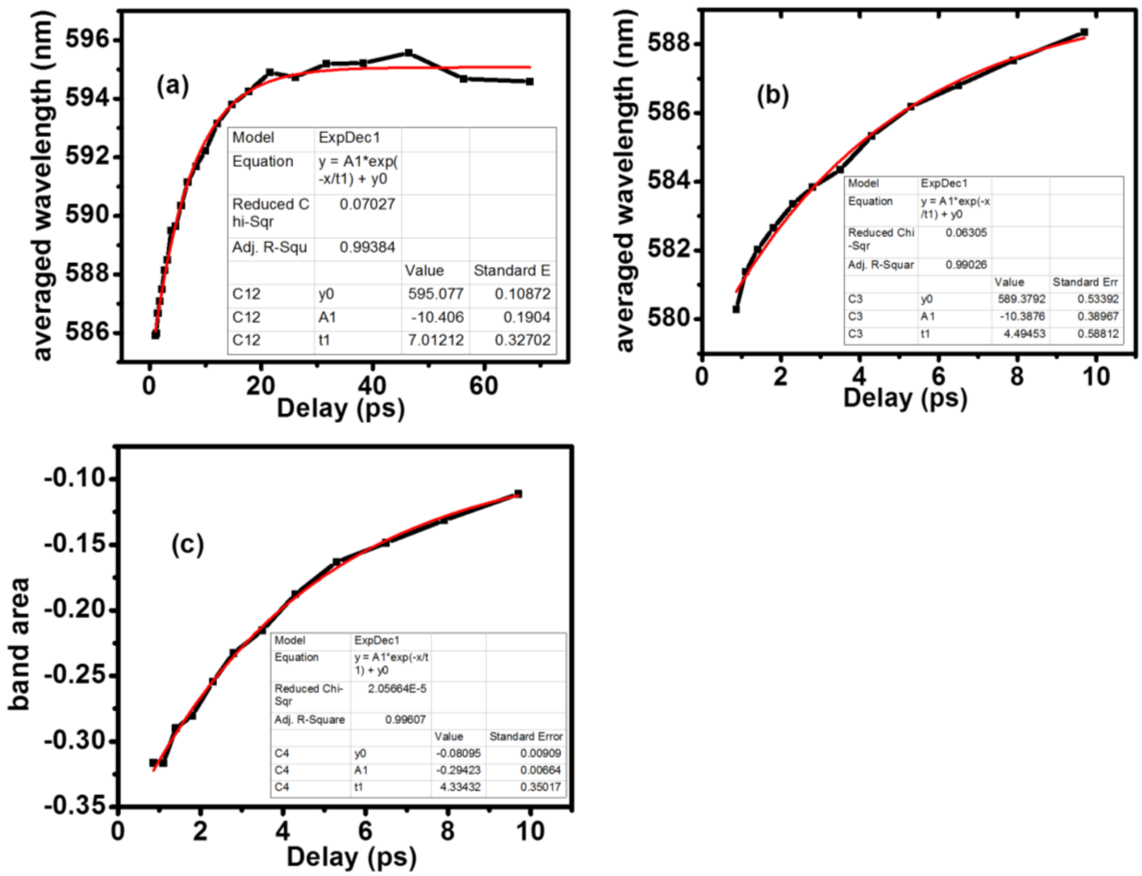

Figure 3.4S. The intensity weighted averaged wavelength of the isolated SE bands were calculated for 530 nm pump (averaged from 550 to 630 nm region) and 420 nm pump (averaged from 550 to 620 nm region) TAS, and the single exponential fit results are plotted in (a) and (b), respectively. The band area from 550 to 620 nm region was also calculated for the 420 nm excitation TAS, and it is shown in (c). For 420 nm pump TAS the time delays only extend up to 10 ps, since ISC begins to occur at longer delays.

3.6.7. Global analysis of *trans*-4TCE TAS following 420-nm excitation

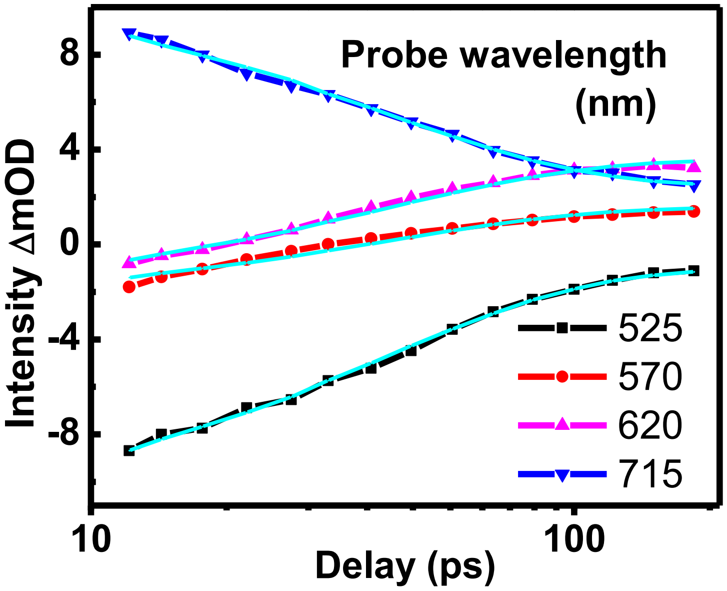

Figure 3.5S. The TAS of *trans*-4TCE with 420 nm excitation was globally fitted between 10 ps and 215 ps using a sequential kinetic interconversion model for ISC, producing an S_1 lifetime of 40.0 ps. Experimental data at selected probe wavelengths (525, 570, 620, 715 nm) are plotted and compared with the global fits.

3.6.8. Fitting and comparison of STA 2 spectral dynamics in TAS of *cis*-4TCE following 530-nm and 420-nm photoexcitation

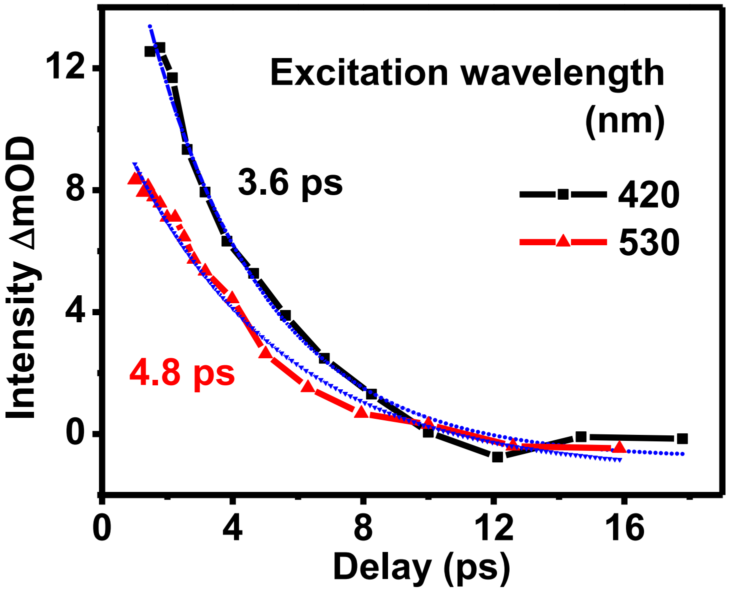

Figure 3.6S. Absorption decays at 452 nm and 472 nm were chosen to present the spectral dynamics of the STA 2 band following 530-nm and 420-nm excitation of *cis*-4TCE. Exponential fits give excited-state relaxation timescales of 4.8 ps and 3.6 ps, respectively.

3.6.9. Fitting of STA 1 spectral dynamics in TAS of cis-4TCE following 530- nm excitation

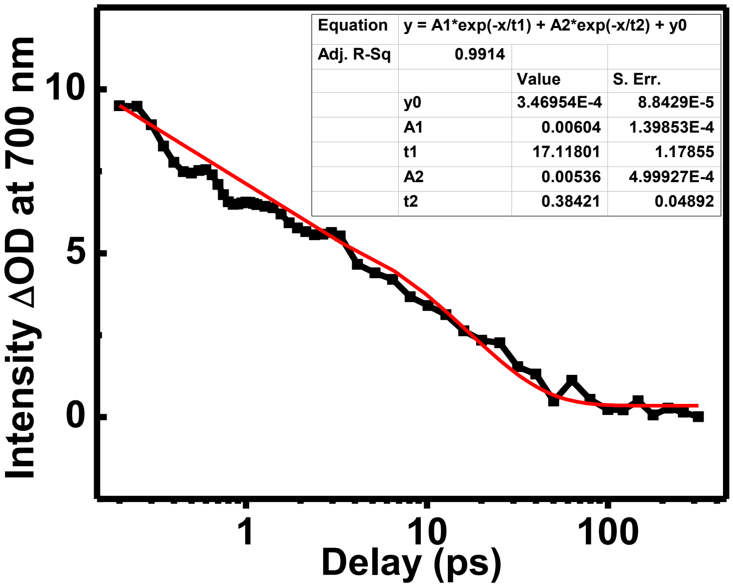

Equation	y = A1*exp(-x/t1) + A2*exp(-x/t2) + y0		
Adj. R-Sq	0.9914		
		Value	S. Err.
	y0	3.46954E-4	8.8429E-5
	A1	0.00604	1.39853E-4
	t1	17.11801	1.17855
	A2	0.00536	4.99927E-4
	t2	0.38421	0.04892

Figure 3.7S. The intensity at 700 nm of TAS of *cis*-4TCE was chosen to present the spectral dynamics of the STA 1 band with 530-nm excitation and was fit with a biexponential function. Experimental data are plotted and compared with fits.

3.6.10. Global analysis of *cis*-4TCE TAS following 420-nm excitation

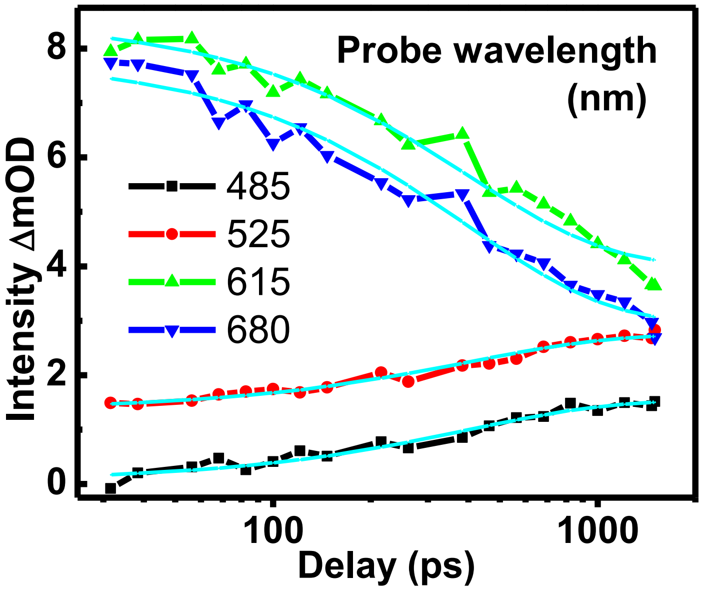

Figure 3.8S. The TAS of *cis*-4TCE photoexcited with 420 nm was globally fitted between 30 ps and 1500 ps using a sequential kinetic interconversion model for relaxation from the T_1 state to S_0 *trans*, which returns a 396 ps lifetime. Experimental data at selected probe wavelengths (485, 525, 615, 680 nm) are plotted and compared with the global fits.

3.6.11. Nanosecond TAS measurements

The spectrometer setup has been described in the main text. For nanosecond measurements, 4TCE was excited with 400 nm, which was obtained by frequency doubling 800-nm pulses in a β Barium borate (BBO) crystal. The white-light probe continuum was generated by focusing an 800 nm beam into a $CaCl_2$ crystal. We used a long manual translation stage (6-ft) to coarsely control the optical path-length of the 400-nm excitation pulses; a motorized translation stage was used to control the delay of the 800-nm beam for white-light probe generation. The time delay range on the motorized translation stage is slightly more than 1.5 ns, but the total pump-probe delay was lengthened by using mechanical and motorized stages together in a "scan and stitch" procedure: For the initial scan, time zero was located by scanning across the motorized translation stage, while the position of the manual stage was fixed. After this first data collection, the relative delay of the 400 nm pump was manually adjusted by 1.0 ns, shifting the scan range accessible with the motorized translation stage to 1.0 – 2.5 ns. The spatial overlap of the pump and probe beams was adjusted to maximize the signal intensity for each scan window. A 0.5 ns overlap between adjacent scans was intentionally retained in order to stitch together transients collected in each time window by signal normalization. Normalization factors were typically between 0.9 and 1.05.

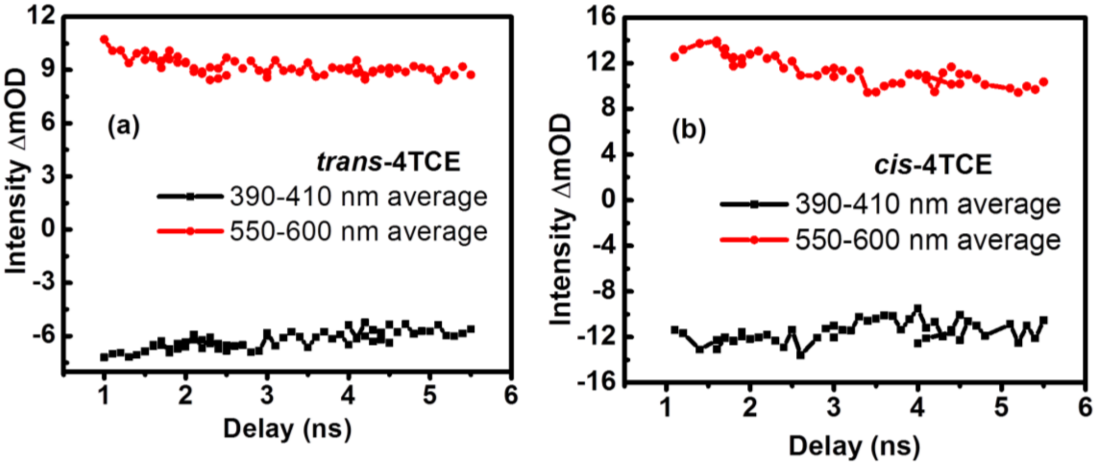

Figure 3.9S. Average intensity for the SE (390-410 nm) and TTA (550-600 nm) obtained via nanosecond TAS with (a) *trans* and (b) *cis* isomers.

3.6.12. Excitation-dependent transient spectra of *trans*-4TCE 1 ns after excitation

Spectral dynamics observed following 530 and 420 nm excitation of *trans*-4TCE are representative of two distinct excited-state relaxation behaviors; a transition between these two behaviors is observed as the pump pulse is tuned from the visible to the near

UV. Notably, we observe a correlation between the TTA absorption intensity and the photoexcitation wavelength: Figure 3.10S plots the TA spectra obtained 1 ns after excitation using various excitation wavelengths covering the lowest-energy transitions of *trans*-4TCE from 360 to 530 nm. For each excitation wavelength the TA spectra have been normalized according to the SE peak intensity at 528 nm at a delay of 10 ps, a delay at which the ultrafast spectral relaxation of the excited singlet is complete. The *cis*-*trans* difference spectrum is plotted with these for comparison. At redder excitation wavelengths (between 460 and 530 nm) transient spectra agree with the steady-state difference spectrum between *cis*- and *trans*-4TCE, demonstrating that the photoinduced isomerization occurs within a nanosecond. As the actinic pump energy increases, the ISC channel can be seen to become more prevalent, as evidenced by the increased triplet absorption at 600 nm.

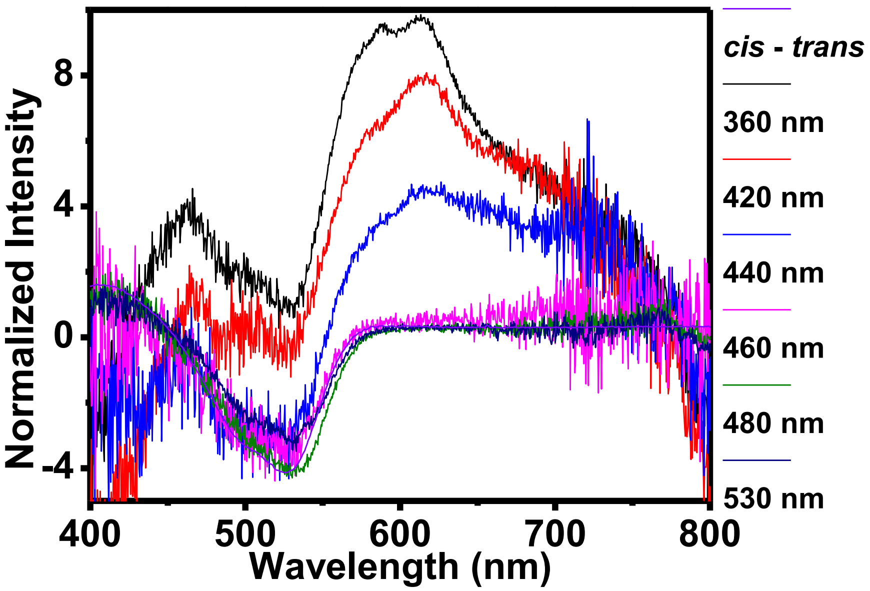

Figure 3.10S. TA spectra captured 1 ns after excitation with various wavelengths covering the S_1 absorption of *trans*-4TCE (360 to 530 nm). Time-resolved spectra were normalized according to SE peak intensity at 528 nm at a delay of 10 ps. TA spectra obtained with 460 to 530 nm match the steady-state difference spectrum between *cis* and *trans* isomers, whereas higher energy excitation leads to increased triplet absorption.

3.6.13. Excitation-dependent transient spectra of *cis*-4TCE 2 ps and 316 ps after excitation

The photoexcitation energy dependence of *cis*-4TCE transient spectroscopy is summarized in Figure 3.11S. TA spectra shown here are normalized by the intensity of STA 2 at 2 ps and plotted in Figure 3.11S(a) at 2 ps and in Figure 3.11S(b) at 316 ps. The position of STA 2 can be seen to red shift consistently when the pump energy is increased. STA 1 and a signature of SE are observed in spectra obtained with excitation wavelengths between 460 and 530 nm. Excitation at higher energies (420 and 440 nm) results in triplet formation, indicated by the appearance of the band peaked at 620 nm. Because STA 2 decays on a timescale longer than the ISC interconversion (Figure 3.3(b)), the data in Figures 3.3(b) and 3.11S(a) indicate that the net spectral relaxation of *cis*-4TCE excited at 420 nm must involve dynamics in both the singlet and triplet manifolds. However, only relaxation of the triplet appears to result in isomerization to the *trans* isomer.

Figure 3.11S(a) demonstrates that ISC can be initiated by pumping 4TCE to energies that can access relevant triplet state(s). Accordingly, at a time delay of 316 ps (Figure 3.11S(b)) only excitation wavelengths shorter than 440 nm generate TTA and a GSB, clearly indicating that some portion of the excited *cis* molecules have transferred into the triplet manifold and are unable to internally convert to the *cis* ground-state, as is observed with 530 nm excitation (Figure 3.3(a)).

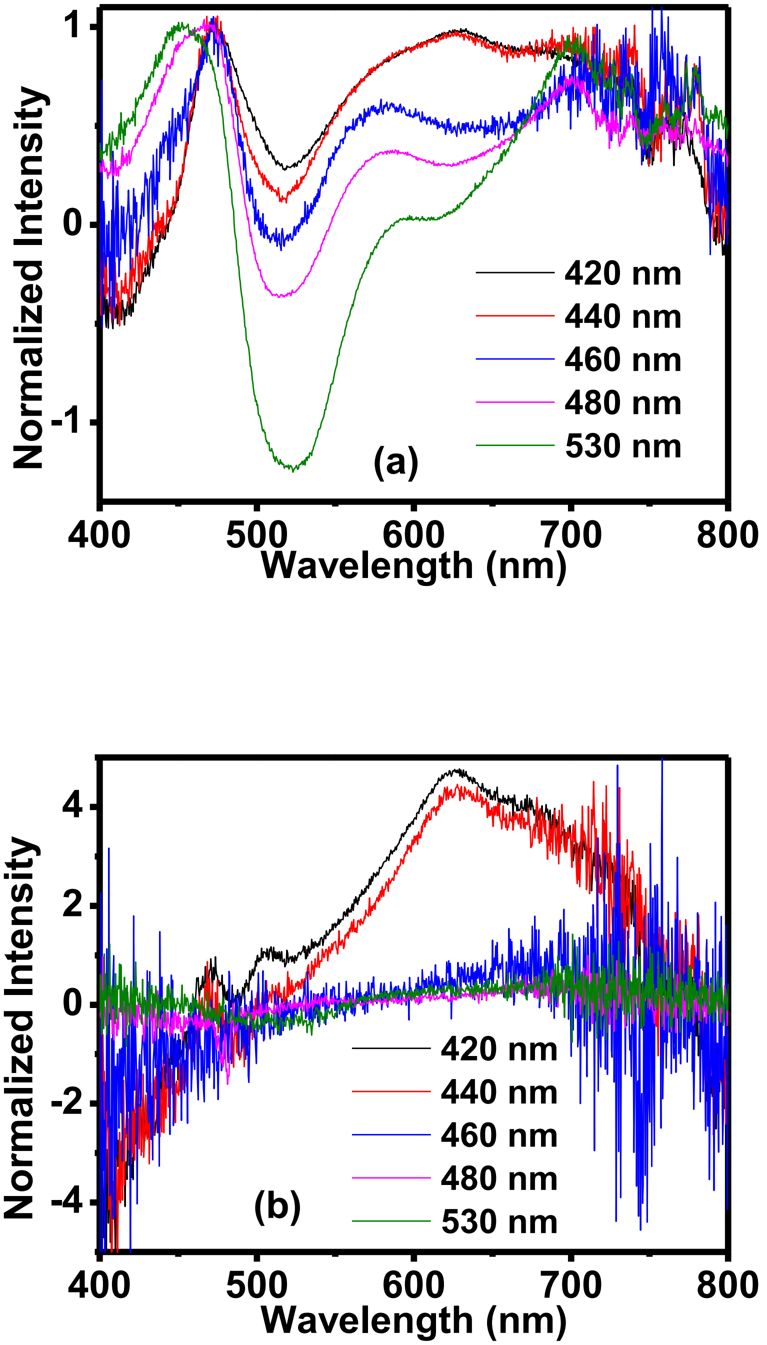

Figure 3.11S. TA spectra of *cis*-4TCE collected with various excitation wavelengths at (a) 2-ps and (b) 316-ps time delays; both sets are normalized according to the STA 2 peak intensity at 2 ps. A consistent red shift of the STA 2 is observed with increased pump energy. Excitations at low energy (between 460 and 530 nm) give a signal of STA 1 and SE, whereas high-energy excitations (420 and 440 nm) lead to TTA centered at 620 nm.

3.6.14. Quantum-chemical calculations

All calculations were performed at CAM-B3LYP/6-31G* level with Polarizable Continuum Model (PCM) (solvent=chlorobenzene) using the Gaussian 09 package.[42]

3.6.14.1 Time-dependent density functional theory (TD-DFT) optimization of S_1 *trans*- and *cis*- 4TCE structures and frequencies

No symmetry constraints were imposed during the S_1 geometry optimization of *trans*- and *cis*-4TCE. No imaginary frequencies were found at the optimized structures for both isomers. (S_0 geometry optimizations can be found in previous work.[27])

3.6.14.2 Natural transition orbital (NTO) analysis

NTO calculation, which relies on finding a compact orbital representation for the electronic transition density matrix,[65] was utilized to assign to transition type to the vertical excitation transitions and nonradiative transitions (ISC). NTO of S_1, S_2, S_4 for *cis* and S_1, S_6 for *trans* were performed at the ground state optimized geometry, and NTO of $T_{1\text{-}2}$ were carried out at the optimized geometry of the S_1. Only T_1 and T_2 are included here since activation energies larger than 0.5 eV result in negligible ISC.[52]

trans S_1 HOMO

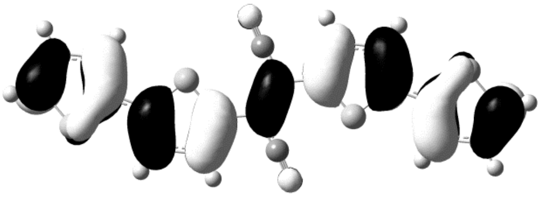

trans S_1 LUMO

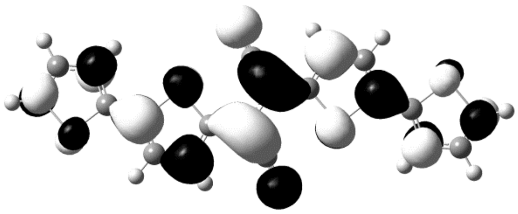

trans S_6 HOMO

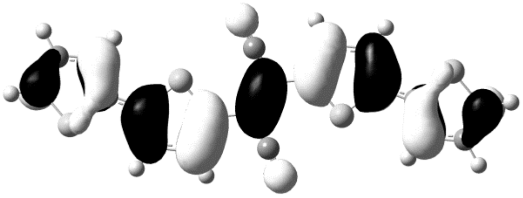

trans S_6 LUMO

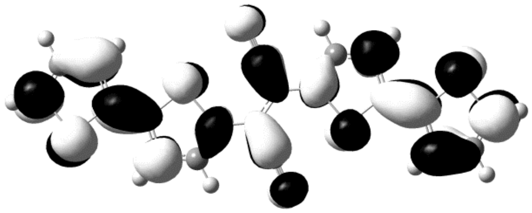

trans T_1 HOMO

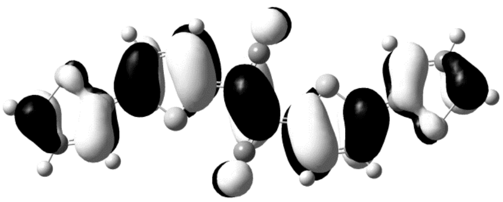

trans T_1 LUMO

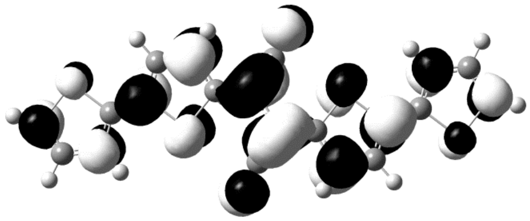

trans T_2 HOMO

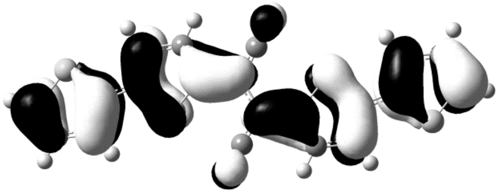

trans T_2 LUMO

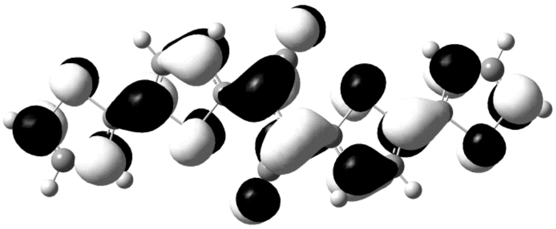

cis S_1 HOMO

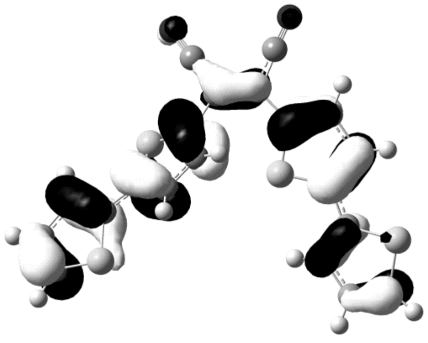

cis S_1 LUMO

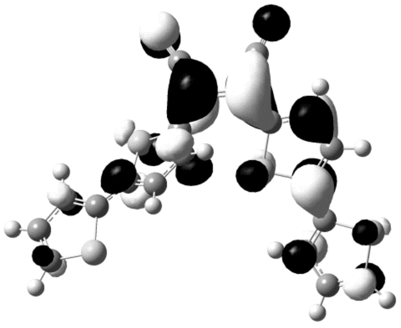

cis S_2 HOMO

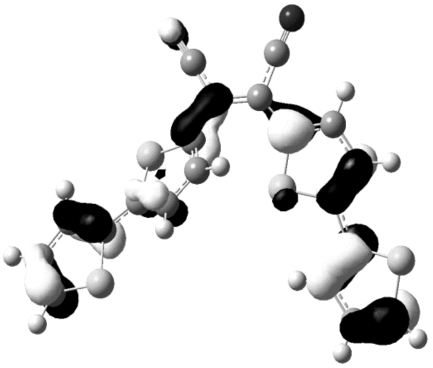

cis S_2 LUMO

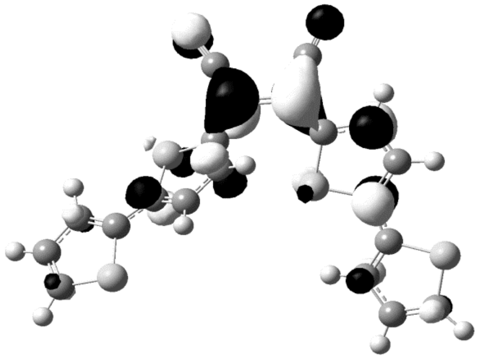

cis S_4 HOMO

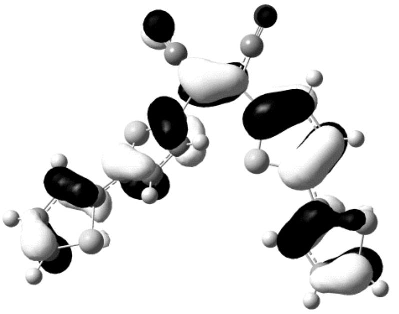

cis S_4 LUMO

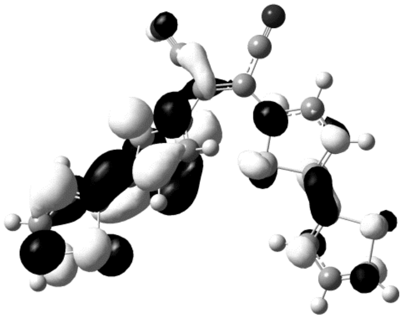

cis T_1 HOMO

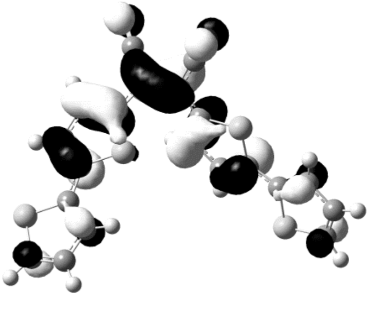

cis T_1 LUMO

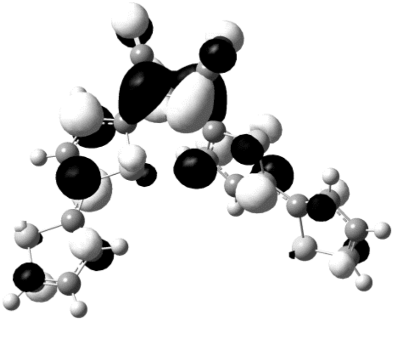

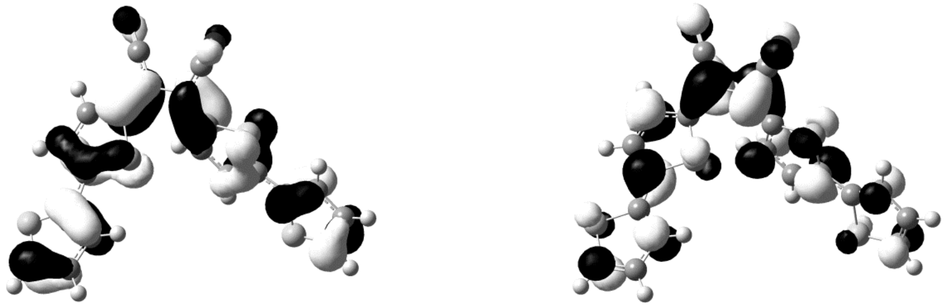

cis T_2 HOMO

cis T_2 LUMO

Figure 3.12S. Natural transition orbital analysis of S_1, S_2, S_4 for *cis* and S_1, S_6 for *trans*

Table 3.1S. DFT/TDDFT Calculated energies of the optimized S_0 geometries, S_1 Franck-Condon state, and S_1 minima for both isomers (unit: eV)

	S_0	S_1^*	S_1
trans	0	2.60	2.16
cis	0.078	2.94	2.17

3.7 References

(1) Irie, M. *Chem. Rev.* **2000**, *100*, 1685.

(2) Minkin, V. I. *Chem. Rev.* **2004**, *104*, 2751.

(3) Irie, M.; Fukaminato, T.; Matsuda, K.; Kobatake, S. *Chem. Rev.* **2014**, *114*, 12174.

(4) Helmy, S.; Leibfarth, F. A.; Oh, S.; Poelma, J. E.; Hawker, C. J.; Read de Alaniz, J. *J. Am. Chem. Soc.* **2014**, *136*, 8169.

(5) Natansohn, A.; Rochon, P.; Ho, M.-S.; Barrett, C. *Macromolecules* **1995**, *28*, 4179.

(6) Andreasson, J.; Pischel, U.; Straight, S. D.; Moore, T. A.; Moore, A. L.; Gust, D. *J. Am. Chem. Soc.* **2011**, *133*, 11641.

(7) Koumura, N.; Zijlstra, R. W. J.; Delden, R. A. v.; Harada, N.; Feringa, B. L. *Nature* **1999**, *401*, 152.

(8) Koumura, N.; Geertsema, E. M.; Meetsma, A.; Feringa, B. L. *J. Am. Chem. Soc.* **2000**, *122*, 12005.

(9) Beharry, A. A.; Woolley, G. A. *Chem. Soc. Rev.* **2011**, *40*, 4422.

(10) Samanta, S.; Qin, C.; Lough, A. J.; Woolley, G. A. *Angew. Chem., Int. Ed.* **2012**, *51*, 6452.

(11) Kamiya, Y.; Asanuma, H. *Acc. Chem. Res.* **2014**, *47*, 1663.

(12) Bandara, H. M.; Burdette, S. C. *Chem. Soc. Rev.* **2012**, *41*, 1809.

(13) Szymanski, W.; Beierle, J. M.; Kistemaker, H. A.; Velema, W. A.; Feringa, B. L. *Chem. Rev.* **2013**, *113*, 6114.

(14) Velema, W. A.; Szymanski, W.; Feringa, B. L. *J. Am. Chem. Soc.* **2014**, *136*, 2178.

(15) Gemayel, M. E.; Borjesson, K.; Herder, M.; Duong, D. T.; Hutchison, J. A.; Ruzie, C.; Schweicher, G.; Salleo, A.; Geerts, Y.; Hecht, S.; Orgiu, E.; Samori, P. *Nat. Commun.* **2015**, *6*, 6330.

(16) Martinez-Lopez, D.; Yu, M. L.; Garcia-Iriepa, C.; Campos, P. J.; Frutos, L. M.; Golen, J. A.; Rasapalli, S.; Sampedro, D. *J. Org. Chem.* **2015**, *80*, 3929.

(17) Leonard, J.; Schapiro, I.; Briand, J.; Fusi, S.; Paccani, R. R.; Olivucci, M.; Haacke, S. *Chem. Eur. J.* **2012**, *18*, 15296.

(18) Sinicropi, A.; Martin, E.; Ryazantsev, M.; Helbing, J.; Briand, J.; Sharma, D.; Leonard, J.; Haacke, S.; Cannizzo, A.; Chergui, M.; Zanirato, V.; Fusi, S.; Santoro, F.; Basosi, R.; Ferre, N.; Olivucci, M. *Proc. Natl. Acad. Sci. U. S. A.* **2008**, *105*, 17642.

(19) Greb, L.; Lehn, J. M. *J. Am. Chem. Soc.* **2014**, *136*, 13114.

(20) Bonacchi, S.; El Garah, M.; Ciesielski, A.; Herder, M.; Conti, S.; Cecchini, M.; Hecht, S.; Samori, P. *Angew. Chem., Int. Ed.* **2015**, *54*, 4865.

(21) Eelkema, R.; Pollard, M. M.; Katsonis, N.; Vicario, J.; Broer, D. J.; Feringa, B. L. *J. Am. Chem. Soc.* **2006**, *128*, 14397.

(22) Siewertsen, R.; Neumann, H.; Buchheim-Stehn, B.; Herges, R.; Näther, C.; Renth, F.; Temps, F. *J. Am. Chem. Soc.* **2009**, *131*, 15594.

(23) Bleger, D.; Schwarz, J.; Brouwer, A. M.; Hecht, S. *J. Am. Chem. Soc.* **2012**, *134*, 20597.

(24) Herder, M.; Schmidt, B. M.; Grubert, L.; Patzel, M.; Schwarz, J.; Hecht, S. *J. Am. Chem. Soc.* **2015**, *137*, 2738.

(25) Yang, Y.; Hughes, R. P.; Aprahamian, I. *J. Am. Chem. Soc.* **2014**, *136*, 13190.

(26) Yang, Y.; Hughes, R. P.; Aprahamian, I. *J. Am. Chem. Soc.* **2012**, *134*, 15221.

(27) Guo, X.; Zhou, J.; Siegler, M. A.; Bragg, A. E.; Katz, H. E. *Angew. Chem., Int. Ed.* **2015**, *54*, 4782.

(28) Saltiel, J.; Hammond, G. S. *J. Am. Chem. Soc.* **1963**, *85*, 2515.

(29) Herkstroeter, W. G.; Hammond, G. S. *J. Am. Chem. Soc.* **1966**, *88*, 4769.

(30) Beharry, A. A.; Woolley, G. A. *Chem. Soc. Rev.* **2011**, *40*, 4422.

(31) Bléger, D.; Hecht, S. *Angew. Chem. Int. Ed.* **2015**, *54*, 11338.

(32) D. Grebner, M. H., and S. Rentsch *J. Phys. Chem.* **1995**, *59*, 16991.

(33) Yang, J.-P.; Paa, W.; Rentsch, S. *Chem. Phys. Lett.* **2000**, *320*, 665.

(34) Chosrovian, H.; Rentsch, S.; Grebner, D.; Dahm, D. U.; Birckner, E. *Synt. Met.* **1993**, *60*, 23.

(35) Paa, W.; Yang, J.-P.; Helbig, M.; Hein, J.; Rentsch, S. *Chem. Phys. Lett.* **1998**, *292*, 607.

(36) Rentsch, S.; Yang, J. P.; Paa, W.; Birckner, E.; Schiedt, J.; Weinkauf, R. *Phys. Chem. Chem. Phys.* **1999**, *1*, 1707.

(37) Paa, W.; Yang, J. P.; Rentsch, S. *Appl. Phys. B* **2000**, *71*, 443.

(38) Waldeck, D. H. *Chem. Rev.* **1991**, *91*, 415.

(39) Quick, M.; Dobryakov, A. L.; Gerecke, M.; Richter, C.; Berndt, F.; Ioffe, I. N.; Granovsky, A. A.; Mahrwald, R.; Ernsting, N. P.; Kovalenko, S. A. *J. Phys. Chem. B* **2014**, *118*, 8756.

(40) Yu, W.; Zhou, J.; Bragg, A. E. *J. Phys. Chem. Lett.* **2012**, *3*, 1321.

(41) Yu, W.; Donohoo-Vallett, P. J.; Zhou, J.; Bragg, A. E. *J. Chem. Phys.* **2014**, *141*, 044201.

(42) Gaussian 09, R. A., M. J. Frisch, G. W. Trucks, H. B. Schlegel, G. E. Scuseria, M.; A. Robb, J. R. C., G. Scalmani, V. Barone, B. Mennucci, G. A. Petersson, H.; Nakatsuji, M. C., X. Li, H. P. Hratchian, A. F. Izmaylov, J. Bloino, G. Zheng, J. L.; Sonnenberg, M. H., M. Ehara, K. Toyota, R. Fukuda, J. Hasegawa, M. Ishida, T. Nakajima,; Y. Honda, O. K., H. Nakai, T. Vreven, J. A. Montgomery, Jr., J. E. Peralta, F. Ogliaro, M.; Bearpark, J. J. H., E. Brothers, K. N. Kudin, V. N. Staroverov, R. Kobayashi, J. Normand,; K. Raghavachari, A. R., J. C. Burant, S. S. Iyengar, J. Tomasi, M. Cossi, N. Rega, M. J.; Millam, M. K., J. E. Knox, J. B. Cross, V. Bakken, C. Adamo, J. Jaramillo, R. Gomperts,; R. E. Stratmann, O. Y., A. J. Austin, R. Cammi, C. Pomelli, J. W. Ochterski, R. L. Martin,; K. Morokuma, V. G. Z., G. A. Voth, P. Salvador, J. J. Dannenberg, S. Dapprich, A.; D. Daniels, Ö. F., J. B. Foresman, J. V. Ortiz, J. Cioslowski, D. J. Fox, Gaussian, Inc.,; Wallingford CT.

(43) Nicklass, A.; Peterson, K. A.; Berning, A.; Werner, H.-J.; Knowles, P. J. *J. Chem. Phys.* **2000**, *112*, 5624.

(44) Becker, R. S.; Melo, J. S. d.; Macanita, A. L.; Elisei, F. *J. Phys. Chem.* **1996**, *100*, 18683.

(45) Benincori, T.; Bongiovanni, G.; Botta, C.; Cerullo, G.; Lanzani, G.; Mura, A.; Rossi, L.; Sannicolo, F.; Tubino, R. *Phys. Rev. B* **1998**, *58*, 9082.

(46) Montalti, M.; Credi, A.; Prodi, L.; Gandolfi, M. T. *Handbook of Photochemistry*; CRC Press: Boca Raton, FL, 2006.

(47) Fischer, E. *J. Phys. Chem.* **1967**, *71*, 3704.

(48) Barik, A.; Indira Priyadarsini, K. *Spectrochim. Acta Mol. Biomol. Spectrosc.* **2013**, *105*, 267.

(49) Hare, P. M.; Crespo-Hernández, C. E.; Kohler, B. *J. Phys. Chem. B* **2006**, *110*, 18641.

(50) Suzuki, K.; Tanabe, H.; Tobita, S.; Shizuka, H. *J. Phys. Chem. A* **1997**, *101*, 4496.

(51) El-Sayed, M. A. *Acc. Chem. Res.* **1968**, *1*, 8.

(52) Beljonne, D.; Shuai, Z.; Pourtois, G.; Bredas, J. L. *J. Phys. Chem. A* **2001**, *105*, 3899.

(53) Lower, S. K.; El-Sayed, M. A. *Chem. Rev.* **1965**, *66*, 199.

(54) Krishna, V. G.; Goodman, L. *J. Chem. Phys.* **1962**, *37*, 912.

(55) Henry, B. H.; Siebrand, W. In *Organic Molecular Photophysis*; Birke, J. B., Ed.; Wiley: London, 1973; Vol. 1.

(56) Cembran, A.; Bernardi, F.; Garavelli, M.; Gagliardi, L.; Orlandi, G. *J. Am. Chem. Soc.* **2004**, *126*, 3234.

(57) Zhao, H.; Liu, K.; Song, D.; Su, H. *J. Phys. Chem. A* **2014**, *118*, 9105.

(58) Venkataramani, S.; Jana, U.; Dommaschk, M.; Sönnichsen, F. D.; Tuczek, F.; Herges, R. *Science* **2011**, *331*, 445.

(59) Cnossen, A.; Hou, L.; Pollard, M. M.; Wesenhagen, P. V.; Browne, W. R.; Feringa, B. L. *J. Am. Chem. Soc.* **2012**, *134*, 17613.

(60) Zheldakov, I. L.; Wasylenko, J. M.; Elles, C. G. *Phys. Chem. Chem. Phys.* **2012**, *14*, 6211.

(61) Zimmermann, G.; Chow, L.-Y.; Paik, U.-J. *J. Am. Chem. Soc.* **1958**, *80*, 3528

(62) Quick, M.; Berndt, F.; Dobryakov, A. L.; Ioffe, I. N.; Granovsky, A. A.; Knie, C.; Mahrwald, R.; Lenoir, D.; Ernsting, N. P.; Kovalenko, S. A. *J. Phys. Chem. B* **2014**, *118*, 1389.

(63) Hatchard, C. G.; Parker, C. A. *Proc. Roy. Soc. (London, Series A)* **1956**, *235*, 518

(64) Nad, S.; Pal, H. *J. Phys. Chem. A* **2003**, *107*, 501.

(65) Martin, R. L. *J. Chem. Phys.* **2003**, *118*, 4775.

Chapter 4: Photoinduced Charge Separation and Recombination in σ-π Conjugated Organosilanes

In part a compilation of two publications:

1. Zhou, J.; Surampudi, S.; Bragg, A. E.; Klausen, R. S. *Chem. Eur. J.* **2016,** *22,* 6204-6207.

2. Zhou, J.; Surampudi, S.; Klausen, R. S.; Bragg, A. E. *in preparation*

This work was collaborative in conjunction with Sravan K. Surampudi[†] and Rebekka S. Klausen[†].

[†]Department of Chemistry, Johns Hopkins University, Baltimore, MD 21218, USA

4.1. Introduction

The attractive features of flexible electronic devices motivate interest in the structure-function relationships underlying high-performance molecular semiconductors. While the tetrahedral semiconductor silicon dominates the electronics industry, most molecular semiconductors are based on π-conjugated organic cores.[1] Yet molecular silicon presents significant attractive opportunities for materials: like the bulk semiconductor, it is earth abundant and the unique tetrahedral and flexible structure of an oligosilane chain lends itself to new and distinct architectures in molecular electronics. Inspired to explore the structural diversity of molecular silicon semiconduc-tors, we recently described the synthesis and electronic characterization of a new class of hybrid organosilicon materials **1a-c** (Scheme 4.1).[2] Record-setting mobilities for a device with an oligosilanyl active layer (up to 0.06 $cm^2 V^{-1} s^{-1}$) were observed and attributed in part to a crystal packing structure inaccessible to all-organic analogs.

Silicon is not only the dominant semiconductor for electronics, but also for solar cells, raising questions about molecular silicon's photophysical properties and potential for optoelectronic device applications.[3,4] An attractive potential of Si-based molecular hybrids in particular is the prospect for optically manipulating charge separation between electron-rich Si and covalently bound electron-deficient acceptors. Here we show explicitly that the photoresponses of the organosilanes **1a-c** involve a direct σ-to-π electron transfer from silicon to an organic acceptor and that the degree of charge transfer depends on the silane chain length. We also demonstrate that the silanes' photophysical properties are similar in the solution and solid state. Insights from our work support the viability of molecular and nanoscale forms of silicon as photoresponsive materials in optoelectronic devices and offer prescriptions for manipulating charge separation in hybrid materials.

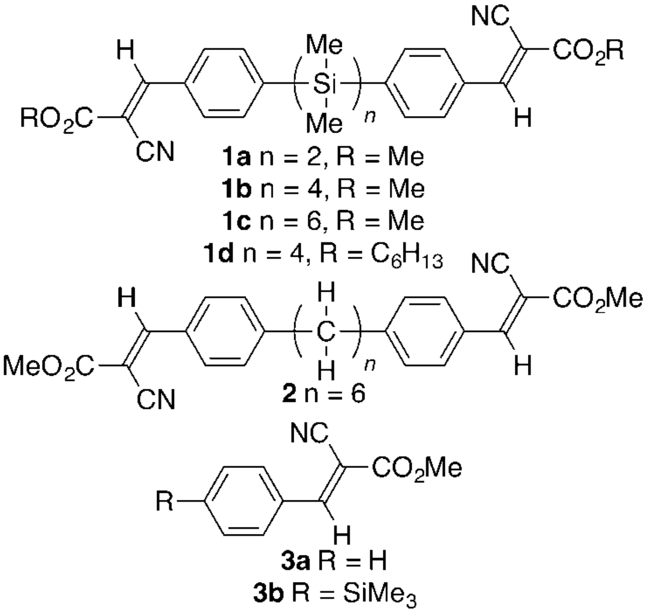

Scheme 4.1. Structures of organosilanes, the carbon analogue and the acceptor moiety

An arresting feature of **1a-c** is their yellow color in solution and in the film state.[2] In contrast, permethylated oligosilanes[5] and carbon-based analogs **2** and **3a**[2] are colorless, implicating the silicon chain as an essential contributor to the photophysical properties of the hybrid materials. We hypothesize an intramolecular charge transfer from silicon to the electron deficient cyanovinyl-substituted arene, an idea supported by solution-phase studies that suggested intermolecular charge transfer from permethylated oligosilanes to the powerful oxidant tetracyanoethylene (TCNE).[6] Incomplete mechanistic understanding of this Si-to-acceptor charge transfer has limited the development of molecular silicon electronic materials. To this end we have conducted a definitive spectroscopic study of charge separation in the covalently linked hybrid materials **1a-c**.

4.2. Experimental methods

Laser pulses for all measurements were generated with the fundamental output of an amplified Ti:Sapphire laser (Coherent Legend Elite, 3.5 mJ/pulse, 1 kHz repetition rate, 35-fs pulse duration, 800-nm peak wavelength). The 360-nm actinic pump was obtained from an optical parametric amplifier (Coherent OperaSolo) through fourth harmonic generation of the OPA signal at 1440 nm. The narrowband 480-nm Raman pump pulse was generated by a white-light-seeded OPA (TOPAS-400, Light Conversion) pumped with the 400-nm output of a second-harmonic bandwidth compressor (SHBC, Light Conversion). Broadband probe pulses (400-750 nm) were generated in a 2-mm calcium fluoride (CaF_2) plate. For transient absorption experiments the polarization of the probe pulse was set at the magic angle relative to the polarization of the actinic pump using a thin broadband wire-gird polarizer (Thorlabs) placed immediately before the sample in order to eliminate signatures of time-dependent polarization anisotropy in the measured spectral dynamics. In femtosecond stimulated Raman measurements, all polarization directions of the actinic pump, Raman pump and probe were kept the same.

The 360-nm actinic pump power was typically 2 μJ/pulse; 480-nm Raman pump power was attenuated to 5 μJ/pulse or less. Both pump pulses were focused to a size of less than 100 μm. The diameter of the white-light probe pulse was measured to be 50 μm. An effective time resolution of the TA measurements of 215-fs was determined by a convoluted fit between a Gaussian function and a single exponential decay of the 450 nm transient. The experimental frequency resolution of Raman measurements is estimated to be 22 cm^{-1}, according to the full width at half maximum (FWHM) of the 700 cm^{-1} C-Cl stretching mode of CH_2Cl_2.

The concentration of all oligosilane samples in dichloromethane (Fisher Scientific, >99% purity) was at the level of 10^{-4} mol/L. Sample solutions were circulated through a 1 mm path-length quartz flow cell, and the optical density of sample solutions were about 0.6 at the peak absorption wavelength. Steady-state UV-vis spectra of sample solutions were checked before and after measurements. No noticeable difference was observed, indicating that no photo degradation occurred during the photophysical measurement.

4.3. Results and discussion

Steady-state spectroscopic characterization (IR and electronic) of **1a-c** shows that charge separation does not occur in the ground state. Figure 4.1 presents FTIR spectra of **1a** and **1b** in film and solution, respectively. Key vibrational frequencies exhibit no appreciable dependence with morphology and comparison with the IR spectrum of **3a** in solution shows that these features arise predominantly from the cyanovinyl moiety. Calculated ground state IR spectra of **1a** and **3b** were obtained using DFT at the CAM-B3LYP/6-31+G* level (frequencies scaled by 0.950 and 4 cm-1 broadening applied) and exhibit remarkable agreement with experiment.

In contrast, the calculated spectrum of the reduced acceptor **3b**$^{\cdot -}$ predicts that the excess electron induces a significant bathochromic shift of the C=C, C=O and C≡N stretches and strongly perturbs the vibrational structure between 1500 and 1700 cm^{-1}. Our calculations show that the C=C bond in particular lengthens from 1.35 to 1.42 Å upon reduction, reflecting reduced bond order and correspondingly lower vibrational frequency. Thus, the experimental IR spectra agree closely with the calculated spectrum of the neutral (rather than reduced) acceptor. Additional evidence against ground-state charge transfer comes from the observed position of the C≡N stretch (~2220 cm^{-1}), which matches that of prototypical cyanovinyl acceptors such as tetracyanoquinodimethane (TCNQ):[7] the nitrile frequency in neutral TCNQ and the charge-transfer salt TTF-TCNQ are observed at 2222 cm^{-1} and 2201 cm^{-1}, respectively.[8]

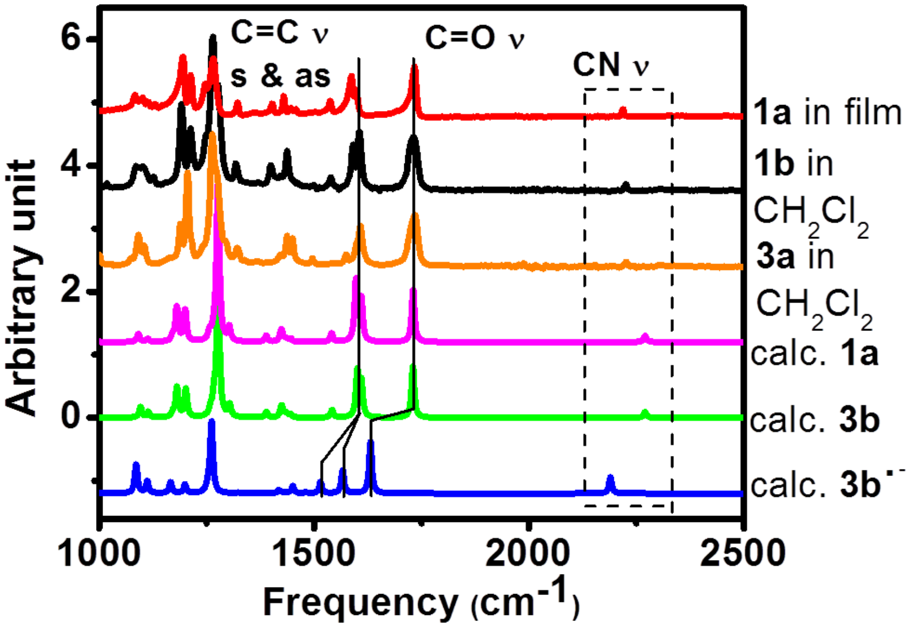

Figure 4.1. FTIR spectra of **1a** in a film and **1b** and **3a** in dichloromethane solution. Calculated IR spectra of **1a**, neutral **3b** and reduced **3b**$^{\cdot-}$ are plotted for comparison. Spectra are scaled according to the C=O feature intensity.

The electronic absorption spectroscopy of **1a-c** further supports that any charge separation must occur in the excited rather than ground state. Figure 4.2 illustrates that the UV-Vis absorbance spectrum of **1b** is dominated by a broad and intense transition around 350 nm (Figure 4.2, solid lines), giving rise to its characteristic yellow color. DFT and TF-DFT calculations indicate that the low-energy side of this feature is associated with a HOMO-LUMO transition, with the HOMO localized predominantly on the electron-rich silanyl core and the LUMO on the cyanovinyl end groups. Transitions localized on only the cyanovinyl moiety are predicted to fall at higher energies. The position of maximum absorbance varies only weakly with solvent polarity. In contrast, significant bathochromism of the dispersed fluorescence with increasing dielectric strength is observed, which is characteristic of excited-state charge transfer in donor-acceptor systems (Figure 4.2, dash lines).[6,7]

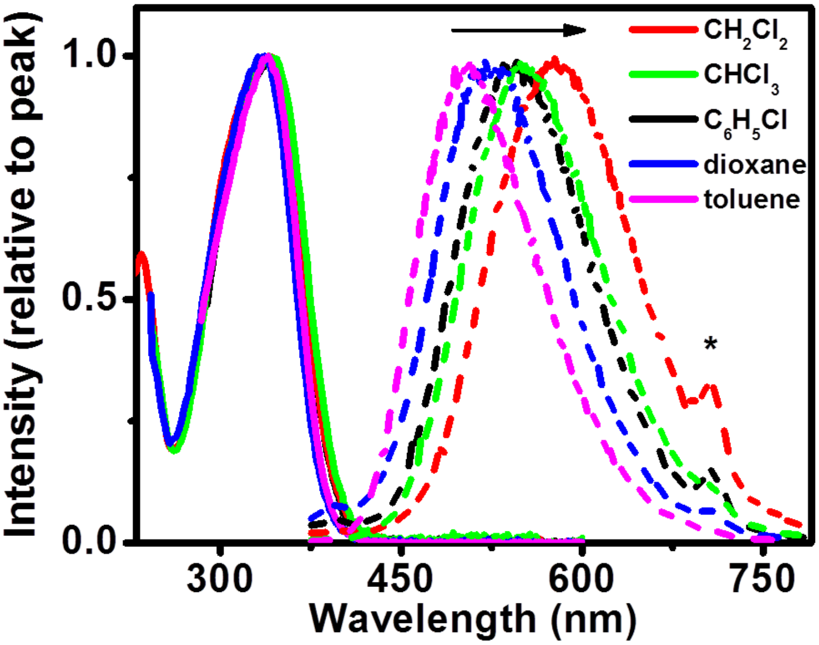

Figure 4.2. UV-Vis absorption (solid lines) and dispersed fluorescence (dash lines) of **1b** in various solvents. Second-order scatter from the fluorescence excitation (360 nm) is marked with an asterisk. The emission peak red-shifts with increasing solvent polarity (noted by the black arrow).

The Lippert equation was employed to further characterize charge separation in the excited state induced by the ICT excitation:

$$\Delta\nu = \frac{2\Delta\mu^2\Delta f}{2hca^3} + constant \tag{4.1}$$

$$\Delta f = \frac{\varepsilon-1}{2\varepsilon+1} - \frac{n^2-1}{2n^2+1} \tag{4.2}$$

Here Δν represents the emission Stokes shift; Δμ is the difference between the ground-state (μ_0) and the excited-state (μ_1) dipole moments; Δf is the orientation polarizability associated with the solvent dielectric constant (ε) and refractive index (*n*) as defined by Equation (2). *h* and *c* are Planck's constant and the speed of light, respectively. *a* is the Onsager cavity radius and its value was estimated from our optimized, calculated ground-state geometries. The linear correlation between Δν and Δf is plotted in Figure 4.3 for **1a-c**. Table 4.1 summarizes the Δμ obtained using a Lippert analysis, as well as the calculated dipole moments from both S_0 and S_1 for **1a-c**. The geometry of **1a** is assumed to be all-anti, as obtained by X-ray crystallography; the computational spectroscopy of such a structure would imply that μ_1 should be dramatically smaller than the others due to a symmetric HOMO orbital. However, the Lippert analysis reveals a significant excited-state dipole, pointing to a breakdown of symmetric ICT similar to the other A-D-A compounds **1b** and **1c**. We therefore infer that either **1a** has appreciable conformation disorder in solution to break the symmetry of the ICT 1 transition or must undergo a large structural reorganization prior to emission.

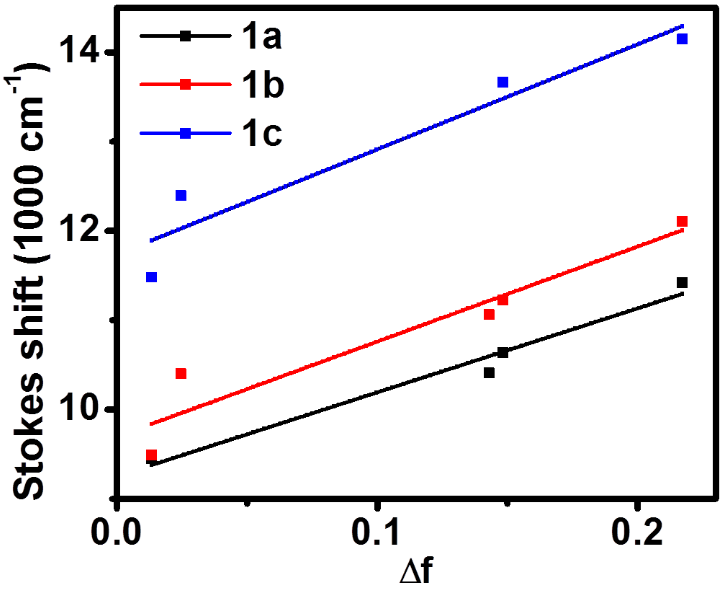

Figure 4.3. Lippert plot of emission Stokes shift, Δν, vs. solvent orientation polarizability, Δf, for **1a-c**.

Table 4.1. Dipole moments for **1a-c**

compound	Δμ from Lippert plot (dB)	μ_0 calc. (dB)	μ_1 calc. (dB)
1a	37.5	4.7	5.6
1b	26.5	5.9	24.5
1c	36.9	4.9	26.0

Ultrafast spectroscopic methods are best suited for characterizing an excited-state charge-transfer mechanism. Figure 4.4 presents the ultrafast transient absorption spectrum of **1b** dissolved in dichloromethane 1 ps after excitation at 360 nm (plotted in red). The two primary features of the transient spectrum include a positive feature peaked near 450 nm and a weaker negative feature centered at 640 nm. The former appears instantaneously (within the 200-fs time resolution of the experiment) and corresponds with absorption from the photoprepared excited state. The negative feature appears in the same wavelength range as the steady-state fluorescence, and therefore corresponds with stimulated emission (SE) from the excited state. Both features are observed to decay within hundreds of picoseconds; the 450 nm transient exhibits a lifetime of 119 ps, as determined with a single-exponential fit (inset of Figure 4.4).

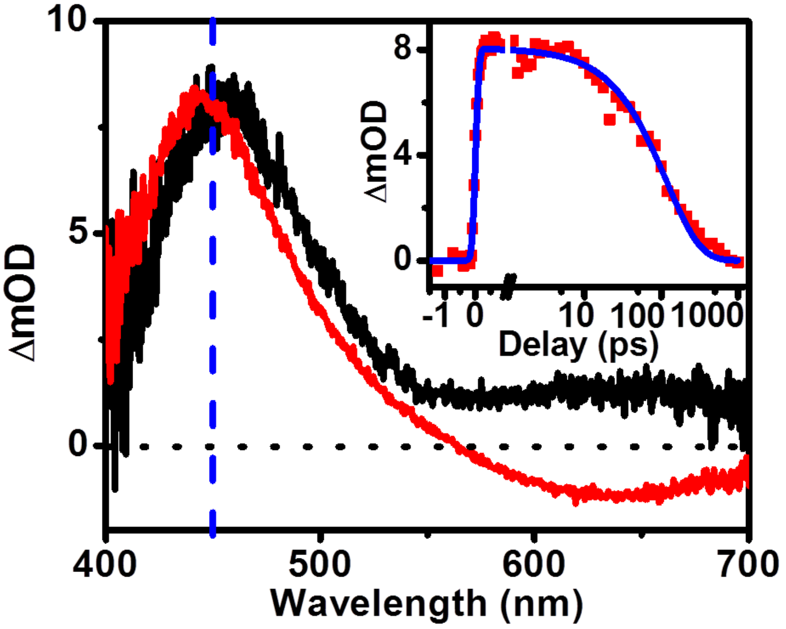

Figure 4.4. TA spectra of **1b** in dichloromethane solution (red) and **1d** cast as a film (black) probed 1 ps after excitation at 360 nm. The TA spectrum of the **1d** film is scaled by a factor of four for comparison with solution data. Inset: Transient decay of excited **1b** in solution as probed at 450 nm.

Greater structural insight is obtained by applying a vibrationally sensitive probe of the excited state.[9] Here we have used femtosecond stimulated Raman spectroscopy (FSRS) to interrogate the properties of photoexcited **1a-c**. FSRS uses the combination of a narrowband (~20 cm^{-1}) Raman excitation and ultrafast (<100 fs) broadband probe to stimulate Raman transitions of multiple vibrational modes coherently.[10] In our measurements resonantly enhanced excited-state FSRS spectra were obtained by using a Raman-excitation wavelength of 480 nm. The photoselectivity on resonance enables us to characterize charge-separated character of the electronic state that underlies the transient absorbance peaked at 450 nm.[11]

The excited-state FSRS (ER) spectra of **1a-c** and the ground-state FSRS (GR) spectrum of **1c** are plotted in Figure 4.5. The ground-state spectrum exhibits a feature discernible from noise near 1600 cm^{-1}; the weak intensity of this spectrum can be attributed to a lack of resonant enhancement with the ground-state transition in the near-UV. In contrast, the Raman spectra of the excited oligomers exhibit a series of intense resonantly enhanced features between 1000 and 1650 cm^{-1}. Time-resolved measurements show that all of these features decay simultaneously on a timescale commensurate with the decay of the transient electronic absorption spectrum (Figure 4) and therefore can be assigned to vibrations of the corresponding photoprepared electronic state.

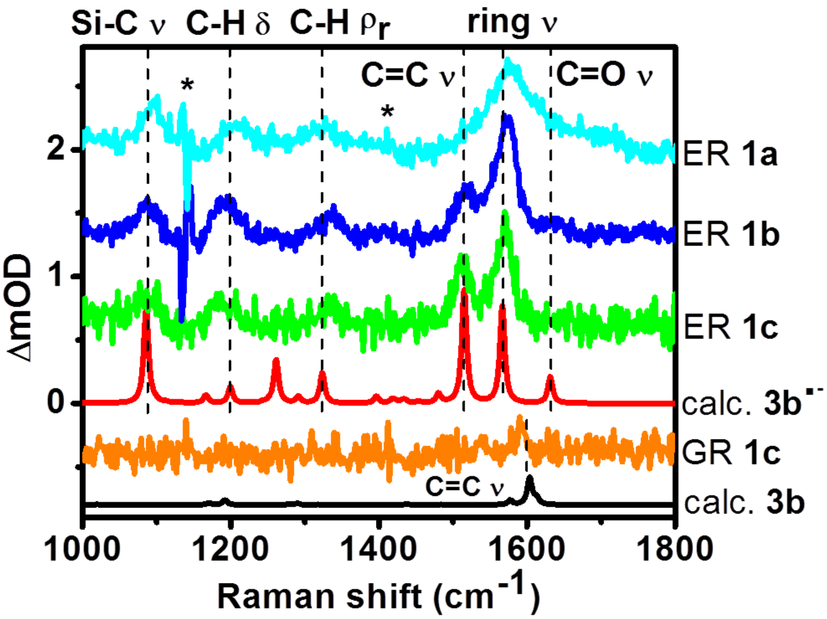

Figure 4.5. Excited-state Raman (ER) of **1a-c** and ground-state Raman (GR) of **1c** in dichloromethane with 360 nm actinic and 480 nm Raman excitations. The time delay between actinic and Raman pulses is 10 ps. Calculated Raman spectra of neutral and reduced forms of **3b** are also plotted for comparison. Residual solvent signals at 1139 and 1415 cm^{-1} are marked with asterisks.

The Raman features apparent in Figure 4.5 arise largely from cyanovinyl vibrational modes. We calculated Raman spectra of the neutral and reduced forms of **3b** in their optimized ground-state geometries using DFT to make comparisons similar to those used in Figure 4.1. Calculated Raman spectra for the neutral and reduced model structures are plotted with the data in Figure 4.5.

Although our calculated Raman spectra do not account for resonance enhancement, comparisons between experiment and calculations show reasonable agreement. The most intense excited-state features observed correspond with C=C stretching (1516 cm^{-1}) and ring-stretching (1568 cm^{-1}) in the reduced cyanovinyl arene moiety. A weaker C=O stretching band appears at 1630 cm^{-1}, whereas three features in the region between 1000 and 1400 cm^{-1} arise from vibrational modes associated with the arene ring of the negatively charged acceptor (Si-C stretch, C-H bend, and C-H rock). The ground-state feature at 1592 cm^{-1} is consistent with the C=C stretching mode predicted for the neutral cyanovinyl. We note that since the C=C and C=O stretches are both IR and Raman active the predicted vibrational spectra of **3b** and **3b**$^{\cdot-}$ are consistent. Thus, Figures 4.1 and 4.5 in combination illustrate that charge separation occurs in the excited but not ground states of these compounds.

Figure 4.5 also reveals a correlation between the C=C stretching frequency and silane chain length: For **1b** and **1c** the C=C and ring stretching modes are separated by 54 and 60 cm^{-1}, respectively, with partial overlap of these features in the spectrum of the former. For **1a** the C=C and ring stretching modes merge entirely. This correlation implies that the degree of photoinduced charge transfer is related to the electron donating strength of the silane chain,[4,12] a general property of charge transfer complexes.[7]

To establish the relevance of the optical charge-transfer mechanism in the solid state, we explored the photoresponse of **1d** drop-cast as a film on a glass slide. We have previously shown that replacement of the methyl ester with n-hexyl side chains results in a more continuous film morphology without perturbing solution phase electronic properties. Figure 4.4 compares the TA spectra of **1d** in film (black line) with **1b** in dichloromethane (red line), both probed 1 ps after 360-nm excitation. Both excited samples exhibit the absorption band near 450 nm attributed to the reduced cyanovinyl arene moiety based on the results of our resonant FSRS measurements. This similarity reveals that charge transfer within the oligosilane compounds can be induced by photoillumination in the solid state as well. The most significant difference between the two TA spectra is the lack of stimulated emission from the film, which may reflect intermolecular charge separation; further characterization of photoinduced electron transfer and transport in the solid-state is underway.

TA spectra of **1c** at time delays shortly following 405-nm excitation are presented in Figure 4.6 to demonstrate the excitation solvation and the ensuing charge recombination processes. The instantaneous appearance of both transient species is within our instrument resolution (0.18 ps). Following the initial appearance of these features the peak negative intensity is observed to red shift from 575 to 665 nm, with a shoulder appearing at 550 nm next to the STA absorption. This spectral shift most likely reflects excited-state structural relaxation and/or dynamic solvation in response to the large nascent dipole of the charge separated excited state. A 5.5-ps timescale for this bathochromic shift is obtained from an exponential fit to the time-dependent position of the SE band, as determined from a weighted average between 560 and 700 nm. Neither the peak position nor intensity of the STA band changes significantly during this spectral evolution (Figure 4.6(b)). Finally, over the course of hundreds of picoseconds both features decay simultaneously (Figure 4.6(c)), reflecting decay of the photoprepared charge-separated excited state. An excited-state lifetime of 170 ps is determined from a single exponential fit to the transient absorbance at 440 nm for delays longer than 5.65 ps (after the ultrafast spectral shift).

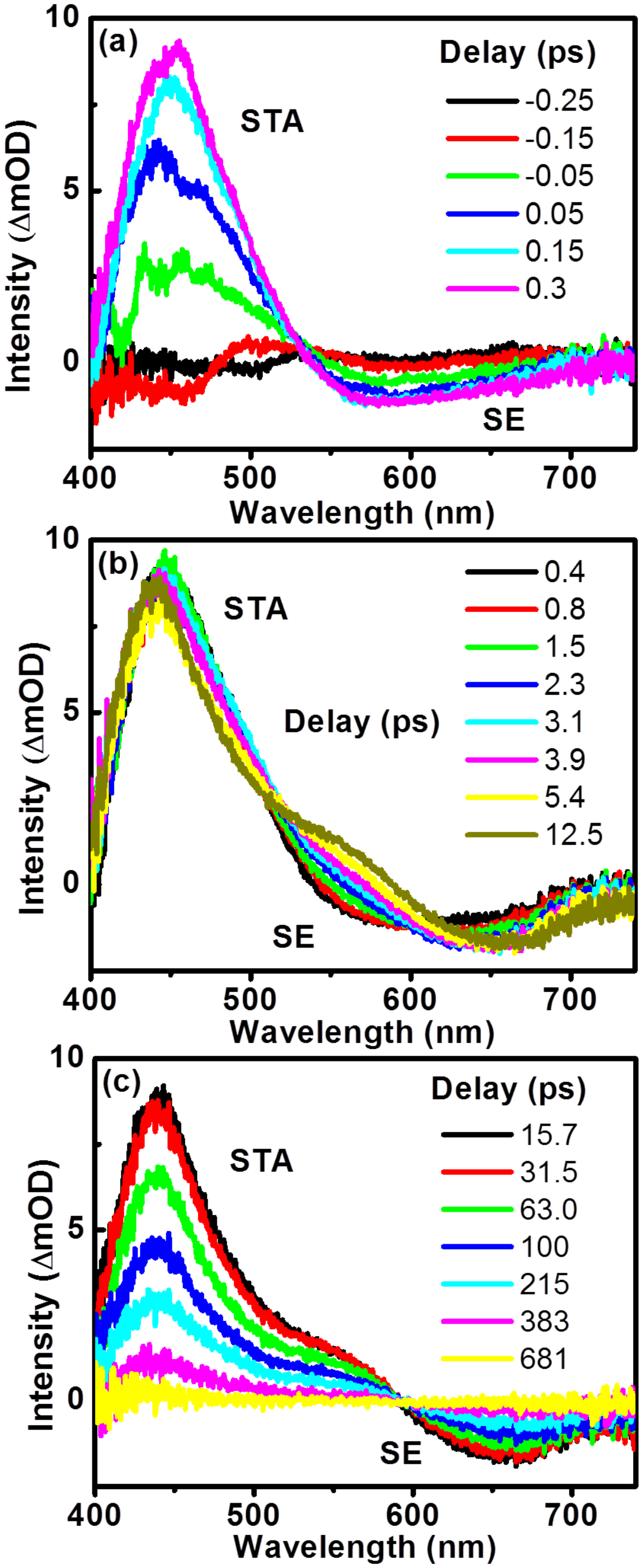

Figure 4.6. TA spectra of **1c** in $CHCl_3$ following 405 nm excitation: (a) ~ -0.25 – 0.3 ps (b) ~ 0.4 – 12.5 and (c) ~ 15.7 – 681 ps.

In conclusion, we have characterized the photophysics of a series of σ,π-hybrid materials using a combination of steady-state and transient spectroscopies. These compounds undergo Franck-Condon (optical) intramolecular electron transfer from the silane to cyanovinyl moieties upon excitation. This is illustrated most clearly with excited-state FSRS spectra that show reduction of the cyanovinyl arene moiety in the photoprepared excited state. Additionally, the frequency of the C=C stretch mode is correlated with the length of the central silane chain and is related to the degree of charge transfer. Similar transient spectroscopy of these compounds in the solution and film states indicates that photoinduced intramolecular charge transfer also occurs in the solid state. Notably, our work is distinguished from the body of research in which silicon chains bridge aromatic donors and acceptors,[13] as the silane chain itself is the electron donor in our materials. Thus, σ-π hybrids such as compounds **1a-c** present interesting new possibilities for controlled, light-driven manipulation of charge in molecular silicon material architectures.

4.4. Supporting material

4.4.1. General Information

4.4.1.1 General Experimental Procedures

All reactions were performed in oven-dried glassware (oven temperature: 170 °C). The flasks were fitted with rubber septa and reactions were conducted under a positive pressure of argon, unless otherwise noted. Anhydrous anaerobic solvents were obtained from JC Meyer solvent purification system (Model: Phoenix 5 solvent freestanding double columns 24 x 24). All column chromatography was performed on a Teledyne ISCO Combiflash Rf using Redisep RF silica columns.

4.4.1.2 Instrumentation

^{1}H NMR, ^{13}C NMR, and ^{29}Si NMR spectra were recorded on a Bruker Avance III 400 MHz Spectrometer. Spectra are reported in parts per million downfield from tetramethylsilane and are referenced to residual protium in the NMR solvent for ^{1}H NMR ($CHCl_3$: δ 7.26; C_6H_6: δ 7.16), carbon resonances of the solvent for ^{13}C NMR ($CDCl_3$: δ 77.0; C_6D_6: δ 128.5) and silicon resonance of tetramethylsilane (TMS) for ^{29}Si NMR (TMS: δ 0.0). Data are represented as follows: chemical shift, multiplicity (br = broad, s = singlet, d = doublet, t = triplet, q = quartet, m = multiplet), coupling constants in Hertz, and integration. High-resolution mass spectra were obtained at the Johns Hopkins University Mass Spectrometry Facility using a VG Instruments VG70S/E magnetic sector mass spectrometer with EI (70 eV). Solid-state infrared (IR) spectrum was obtained using Thermo Scientific Nicolet iS 5 FT-IR spectrometer with iD 5 ATR attachment. Solution-phase IR spectrum was obtained using Nexus 670 FT-IR with Smart Golden Gate ATR attachment. UV-vis spectrum was recorded by a diode-array spectrometer fiber-optically coupled to tungsten and incandescent deuterium light sources (Stellarnet). Fluorescence spectrum was collected by a PERKIN-ELMER LS-5B Luminescence Spectrometer. The UNIlab Plus Glove Box by MBRAUN was maintained under nitrogen atmosphere.

4.4.2. Time-resolved transient absorption (TA) spectra of 1b in CH_2Cl_2 following 360-nm excitation

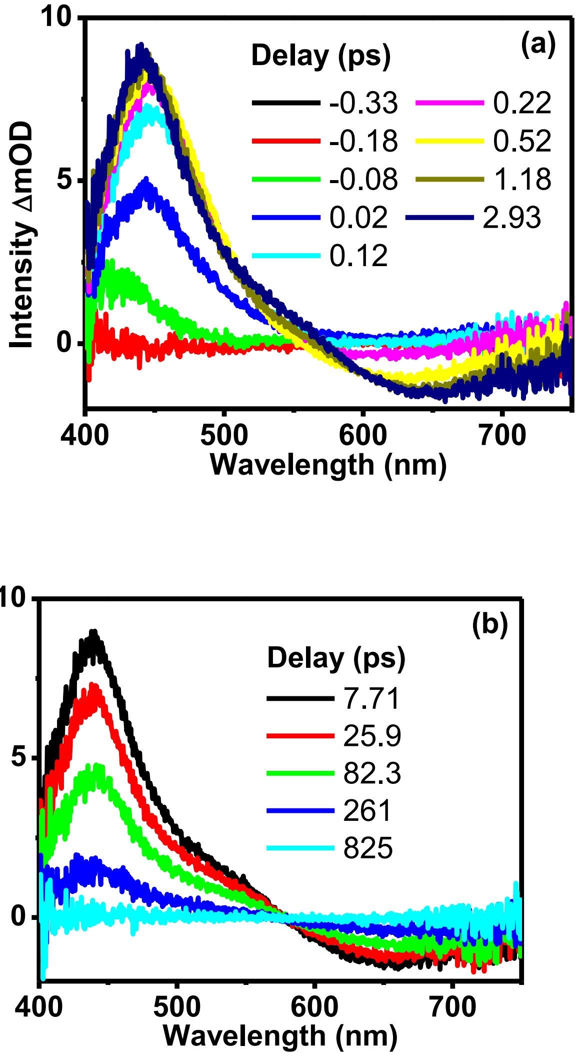

Figure 4.1S. TA spectra of **1b** in CH_2Cl_2 excited at 360 nm (a) before and (b) after 5 ps.

4.4.3. Acquisition algorithms for femtosecond stimulated Raman spectroscopy (FSRS)

FSRS data acquisition algorithms have been described previously.[4,5,7] Pulse combinations for excited-state Raman (ER) and ground-state Raman (GR) spectra are indicated with subscripts in Equation 4.3:

$$\mathrm{ER} = \log(I_{\mathrm{pu+r+pr}}/I_{\mathrm{pr}}) \tag{4.3a}$$

$$\mathrm{GR} = \log(I_{\mathrm{r+pr}}/I_{\mathrm{pr}}) \tag{4.3b}$$

The subscripts in Eqn. 4.1S refer to the actinic photoexcitation (pu), Raman excitation (r) and white light probe (pr) pulses, respectively.

The processing of FSRS data has also been described in our previous publications.[7] In order to isolate the pure ER spectrum, we first subtract the solvent (CH_2Cl_2) and non-resonant solute Raman signals from the raw ER spectrum. For these purposes the GR spectrum has been scaled based on the size of the solvent peak at 700 cm^{-1} and subsequently subtracted at all delays. Since the shape of the broad baseline (500-2600 cm^{-1}) are quasi-linear, we account for it with a second-order polynomial fit, which is determined and subtracted from each spectrum to yield those presented in Figure 4.4 of the text. Figure S4.2 presents a graphical example of the processing of FSRS data of **1b** at a 10 ps time delay.

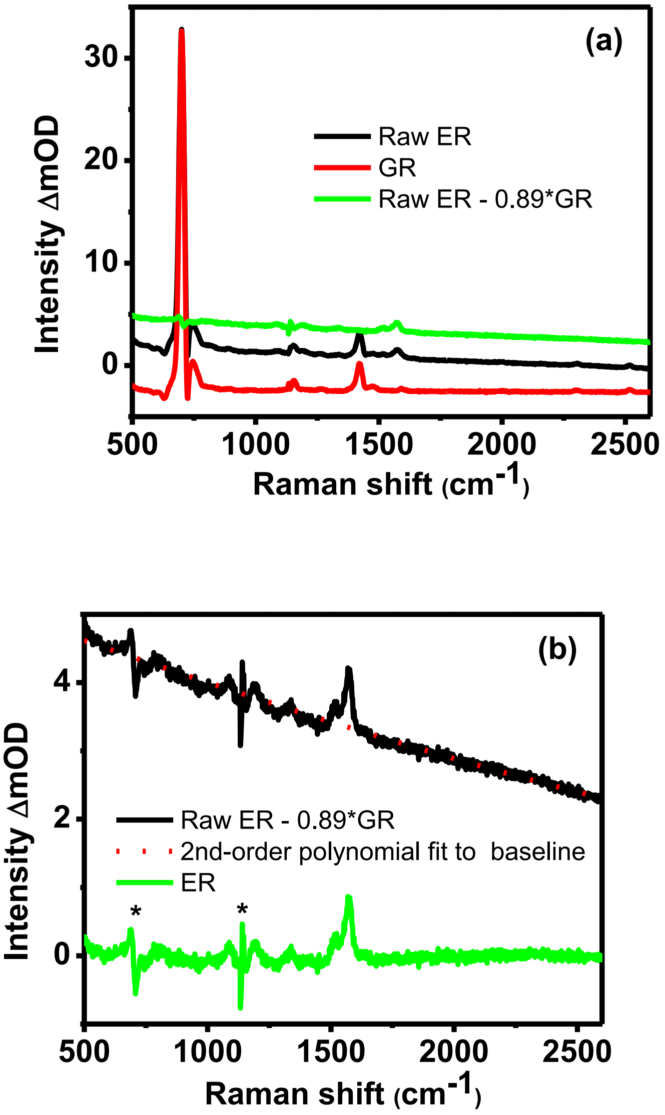

Figure 4.2S. (a) Raw ER and GR spectra and their difference after scaled subtraction. In order to fully remove the solvent signal, a scaling factor of 0.89 has been determined using the intensity of the 700 cm^{-1} solvent feature. (b) The broad baseline remaining is fit with a second-order polynomial, and contributions to the spectrum from only Raman-active excited-state vibrations are isolated by baseline subtraction. No spectral smoothing process has been applied. Residual solvent signals from imperfect subtraction are marked with asterisks.

4.4.4. Time-resolved FSRS spectra of 1b in CH_2Cl_2 following 360-nm actinic and 480-nm Raman excitations

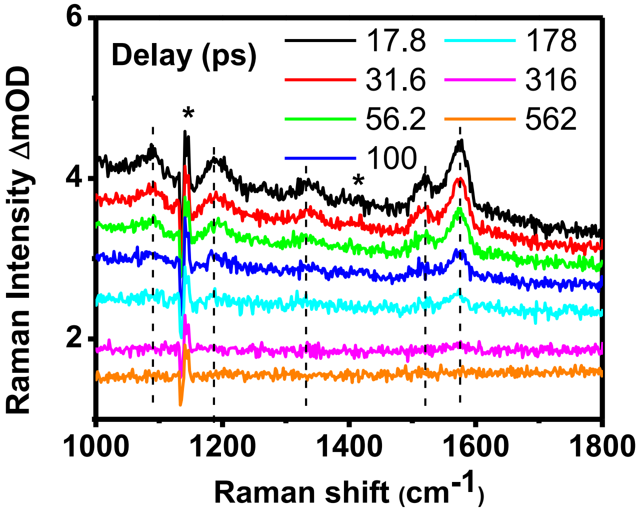

Figure 4.3S. Time-resolved excited-state Raman spectra from **1b** in dichloromethane with 360 nm actinic and 480 nm Raman excitations. Ground-state Raman signals have been scaled based on the size of the solvent peak at 700 cm^{-1} and subsequently subtracted at all delays. The broad baseline has not been removed and the entire spectra are presented without smoothing. Residual solvent signals at 1139 and 1415 cm^{-1} are marked with asterisks.

4.4.5. Fitting of ring-stretching mode intensity of 1b in CH_2Cl_2 observed with FSRS following 360-nm actinic excitation

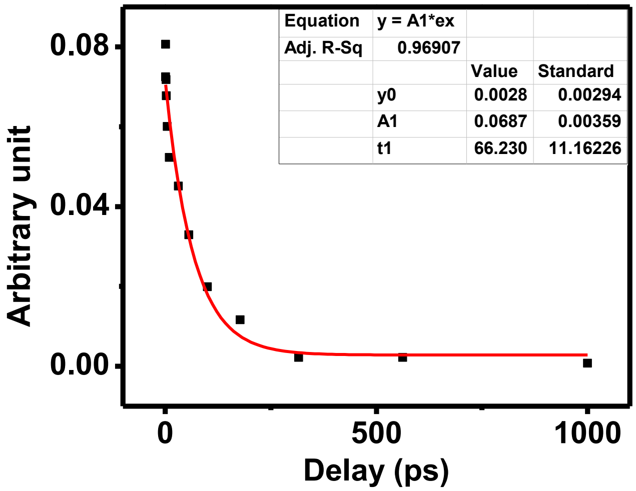

Equation	y = A1*ex		
Adj. R-Sq	0.96907		
		Value	Standard
	y0	0.0028	0.00294
	A1	0.0687	0.00359
	t1	66.230	11.16226

Figure 4.4S. A single exponential fit to the intensity of the ring stretching mode returns a lifetime of 66 ps. The different in the lifetimes obtained from TA and FSRS arises from the different polarization conditions of these measurements: in TA the angle polarization of the pump and probe pulses is set to magic angle, whereas in FSRS all polarization directions of the actinic pump, Raman pump and probe are parallel. Consequently, the lifetime estimated from FSRS is considerably shorter than that from TA, as it includes relaxation of the polarization anisotropy not present in magic angle TA measurements.

4.4.6. Quantum-chemical calculations

All computational geometry optimizations were performed at the CAM-B3LYP/6-31+G* level using the Gaussian 09 package.

4.4.6.1 Ground-state optimization of neutral acceptor structure, identification of important vibrational modes and their frequencies

S_0 geometry optimization of the neutral cyanovinyl acceptor was performed without symmetry constraints. No imaginary frequencies were found at the optimized structure.

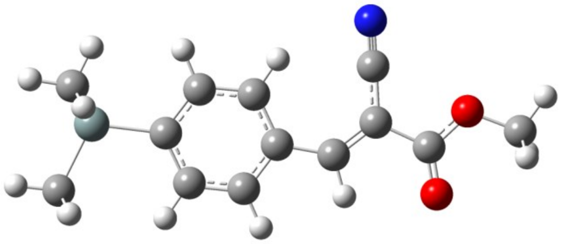

Figure 4.5S. S_0 optimized structure of neutral acceptor.

4.4.6.2 Ground-state optimization of negatively charged acceptor structure, frequency and important vibrational modes

S_0 geometry optimization of the reduced cyanovinyl acceptor was performed without symmetry constraints. No imaginary frequencies were found at the optimized structure.

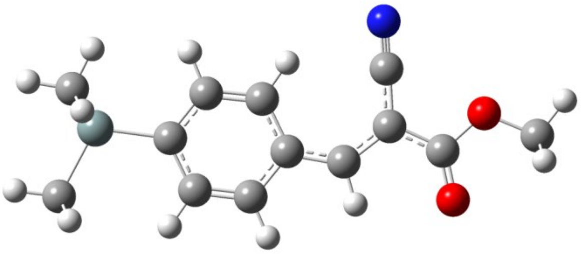

Figure 4.6S. S_0 optimized structure of negatively charged acceptor

4.4.6.3 Important vibrational modes

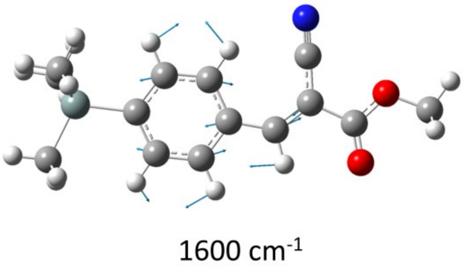

Figure 4.7S. Strongly Raman-active vibrational mode of the neutral acceptor (present in FSRS spectrum).

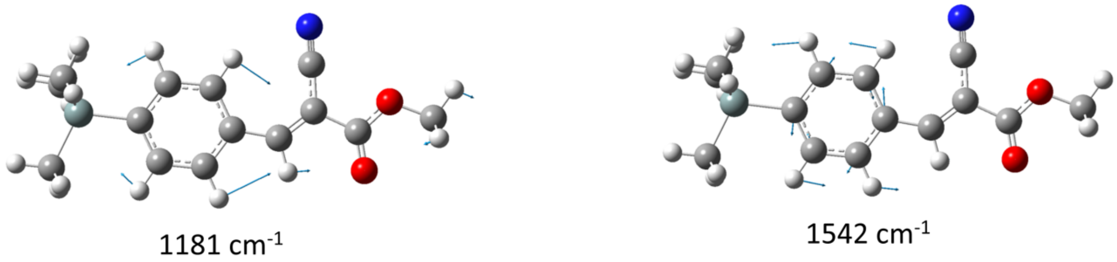

Figure 4.8S. Weakly Raman-active vibrational modes of the neutral acceptor (not apparent in experimental FSRS spectrum).

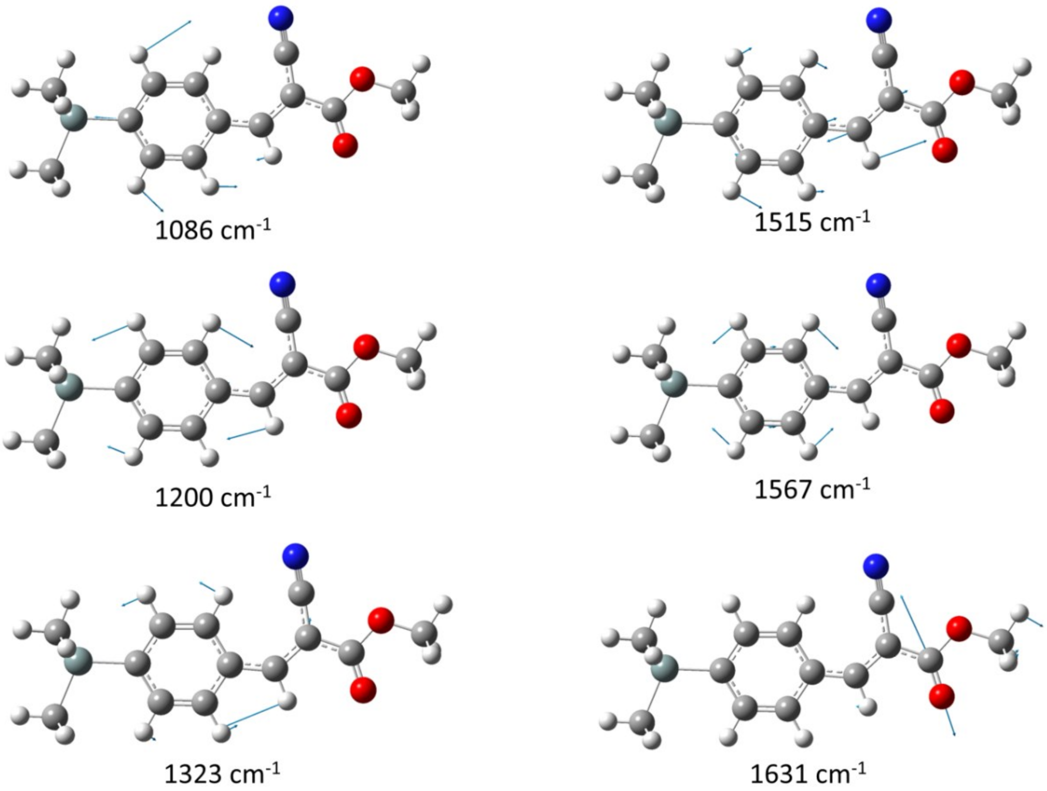

1086 cm^{-1}

1515 cm^{-1}

1200 cm^{-1}

1567 cm^{-1}

1323 cm^{-1}

1631 cm^{-1}

Figure 4.9S. Strongly Raman-active vibrational modes of the reduced acceptor (present in experimental FSRS spectrum). In Figure 3 of the main text the three FSRS features in the region between 1000 and 1400 cm^{-1} can be assigned as Si-C stretching at 1085 cm^{-1}, C-H bending at 1197 cm^{-1} and C-H rocking on the aryl ring at 1333 cm^{-1}.

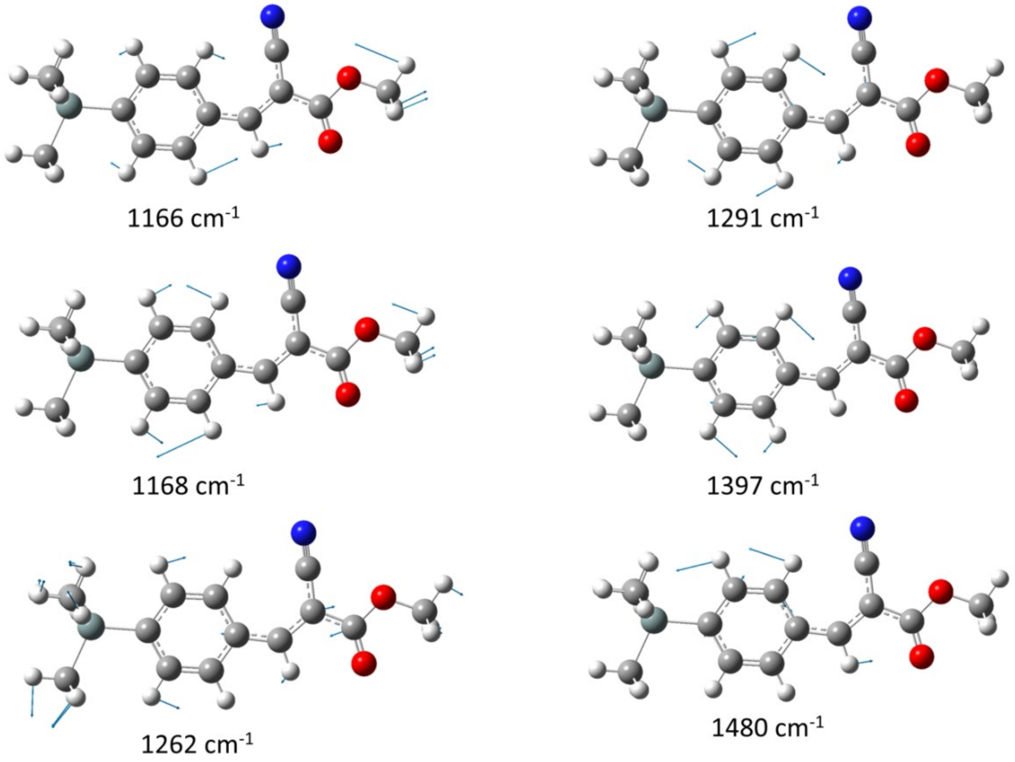

1166 cm^{-1} 1291 cm^{-1}

1168 cm^{-1} 1397 cm^{-1}

1262 cm^{-1} 1480 cm^{-1}

Figure 4.10S. Weakly Raman-active vibrational modes of the reduced acceptor (not apparent in the experimental FSRS spectrum).

4.5 References

(1) F. Cicoria, C. Santato. Organic Electronics: Emerging Concepts and Technologies, Somerset: Wiley, 2013.

(2) S. Surampudi, M. L. Yeh, J. F. M. Hardigree, M. A. Siegler, T. A. Kasl, H. E. Katz, R. S. Klausen, *Chem. Sci*. **2015**, *6*, 1905-1909.

(3) L. Li, T. Matsuo, D. Hashizume, H. Fueno., K. Tanaka, K. Tamao, *J. Am. Chem. Soc*. DOI: 10.1021/jacs.5b10113

(4) R. D. Miller, J. Michl, *Chem. Rev.* **1989**, *89*, 1359-1410.

(5) H. Gilman, W. H. Atwell, G. L. Schwebke, *J. Organometal. Chem*. **1964**, *2*, 369-371.

(6) a) V. F. Traven, R. West, *J. Am. Chem. Soc*. **1973**, *95*, 6824-6826. b) H. Sakurai, M. Kira, T. Uchida, *J. Am. Chem. Soc*. **1973**, *95*, 6826-6827.

(7) K. P. Goetz, D. Vermeulen, M. E. Payne, C. Kloc, L. E. McNeil. D. O. Jurchescu, *J. Mater. Chem. C* **2014**, *2*, 3065-3076.

(8) J. S. Chappell, A. N. Block, W. A. Bryden, M. Maxfield, M. T. O. Poehler, D. O. Cowan, *J. Am. Chem. Soc.* **1981**, *103*, 2442-2443.

(9) a) W. Yu, J. Zhou, A. E. Bragg, *J. Phys. Chem. Lett*. **2012**, *3*, 1321-1328. b) J. Zhou, W. Yu, A. E. Bragg, *J. Phys. Chem. Lett.* **2015**, *6*, 3496-3502.

(10) R. R. Frontiera, R. A. Mathies, *Laser Photonics Rev.* **2011**, *5*, 102-113.

(11) a) T. Magnanelli, A. E. Bragg, *J. Phys. Chem. Lett*. **2015**, *6*, 438-445. b) F. Provencher, N. Bérubé, A. W. Parker, G. M. Greetham, M. Towrie, C. Hellman, M. Côté, N. Stingelin, C. Silva, C., S. C. Hayes, *Nat. Commun*. **2014**, *5*, 4288-4293. c) A. L. Smeigh, M. Creelman, R. A. Mathies, J. K. McCusker, *J. Am. Chem. Soc.*, **2008**, *130*, 14105-14107.

(12) D. W. Rooklin, T. Schepers, M. K. Raymong-Johansson, J. Michl, *Photochem. Photobiol. Sci.*, **2003**, *2*, 511-517.

(13) a) G. Mignani, A. Krämer, G. Puceeti, I. Ledoux, G. Soula, J. Zyss, R. Meyrueix, *Organometallics* **1990**, 9, 2640-2643. b) G. Mignani, A. Krämer, G. Pucceti, I. Ledoux, J. Zyss, G. Soula, Organometallics 1991, 10, 3656-3659. c) G. Mignani, M. Barzoukas, J. Zyss, G. Soula, F. Balegroune, D. Grandjean, D. Josee, *Organometallics* **1991**, *10*, 3660-3668. d) H. K. Sharma, K. H. Pannell, I. Ledoux, J. Zyss, A. Ceccanti, P. Zanello, *Organometallics* **2000**, *19*, 770-774. e) M. Shimada, Y. Yamanoi, T. Matsushita, T. Kondo, E. Nishibori, A. Hatakeyama, K. Sugimoto, H. Nishihara, *J. Am. Chem. Soc.* **2015**, *137*, 1024-1027.

Chapter 5: Quenching of pH-Responsive Luminescence of a Benzoindolizine Sensor by Ultrafast Hydrogen Shift

In part a compilation of two publications:

1. Outlaw, V. K.; Zhou, J.; Bragg, A. E.; Townsend C. A. *RSC Adv.* **2016,** *6,* 61249-61253.

2. Zhou, J.; Outlaw, V. K.; Townsend C. A.; Bragg, A. E. *Chem. Eur. J.* DOI: 10.1002/chem.201603284

This work was collaborative in conjunction with Victor K. Outlaw [†] and Craig A. Townsend [†].

[†]Department of Chemistry, Johns Hopkins University, Baltimore, MD 21218, USA

5.1. Introduction

The design of fluorescent molecular sensors requires consideration of how photoinduced structural dynamics control the photophysics of a sensing state.[1, 2] For example, sensors that operate via excited-state proton transfer (ESPT)[3] require the analyte to disrupt or create H^+ transfer networks between donating and accepting groups. For sensors based on fluorescent proteins,[4-7] intrinsic ESPT within the fluorophore alters the emission gap; interactions with an analyte quench ESPT and alter the sensor's fluorescence. In contrast, fluorescent sensors for anion detection involves ESPT directly to the analyte.[8, 9] A related consideration is how secondary interactions (in addition to those with an analyte) affect sensor photophysics and can thus be used to limit sensing to specific environments, such as surfaces, interfaces, chemical hosts, or binding pockets. Here we report quenching of pH-responsive emission of a methoxylated benzoindolizine (bi) through a novel mechanism: ultrafast, net [1,3] H shift. Through comparison with the photophysics of methyl bi, we illustrate that this rearrangement is controlled by electronic interactions between the core bi chromophore and strongly electron-donating methoxyl group – an effect that could be modulated through binding interactions for location-specific sensing.

5.2. Experimental methods

The synthesis of biMe and biOMe has been reported in detail elsewhere.[10] In brief, the bi compounds can be made by an efficient one-pot synthesis by Wittig reaction of the corresponding indole-2-carboxaldehydes with fumaronitrile and triethylphosphine, followed by base-catalyzed cyclization.[19, 20] Methanol and TFA were of analytical grade and purchased from Fisher Scientific. UV-vis spectra were recorded with a diode-array spectrometer fiber-optically coupled to tungsten and incandescent deuterium light sources (Stellarnet). Fluorescence spectra were collected with a PERKIN-ELMER LS-5B Luminescence Spectrometer. The concentration of biMe and biOMe were at the level of 10^{-4} mol/L for time-resolved measurements. Excess TFA was added to solutions to prepare protonated samples; complete protonation was determined from changes in the steady-state UV-vis spectra. Sample solutions were circulated through a 1 mm path-length quartz flow cell, and the optical density of sample solutions were typically ~ 0.5 at the peak absorption wavelength. No photodegradation occurred during the photophysical measurement as evidenced by identical UV-vis spectra of sample solutions collected before and after TA experiments.

The ultrafast laser setup has been described previously.[21-23] Here we briefly note experimental details essential to this work. Laser pulses for all measurements were generated with the fundamental output of an amplified Ti:Sapphire laser (Coherent

Legend Elite, 3.5 mJ/pulse, 1 kHz repetition rate, 35-fs pulse duration, 800-nm peak wavelength). The 360-nm excitation was obtained from an optical parametric amplifier (Coherent OperaSolo) through fourth harmonic generation of the OPA signal at 1440 nm. The excitation power was attenuated to about 2 μJ/pulse by passing through a neutral density filter. Broadband probe pulses (400-750 nm) were obtained through white-light generation in a 2-mm calcium fluoride (CaF_2) plate. The polarization of the probe pulse was set at the magic angle (54.7^o) relative to the polarization of the excitation pulse using a thin broadband wire-gird polarizer (Thorlabs) placed immediately before the sample in order to eliminate signatures of time-dependent polarization anisotropy in the measured spectral dynamics. The pump pulse was focused to a size of less than 100 μm. The diameter of the white-light probe pulse was measured to be 50 μm. The effective time resolution for TAS was measured as 125 fs, as determined by a Gaussian convoluted fit to the 600-nm trace in the $biMeH^+$ TAS (Figure 5.3S).

5.3. Computational methods

The ground-state geometries of the three tautomers (N, T1, and T2) for each protonated compound were optimized by DFT. All computational geometry optimizations were performed at the CAM-B3LYP/6-31G* level with Polarizable Continuum Model (PCM) to incorporate the effect of CH_3OH using the Gaussian 09 package.[24] TDDFT was then used to calculate the vertical $S_0 \rightarrow S_1{}^*$ (absorption) gap, optimize the minimum-energy S_1 structure, and calculate the $S_1 \rightarrow S_0{}^*$ (emission) gap for each tautomer. No imaginary frequencies were found at the optimized structures for all tautomers.

5.4. Results and discussion

6-amino-8-cyanobenzo[1,2-*b*]indolizines (bi), which exhibit pH-responsive fluorescence, were synthesized by our collaborators.[10] The emission peak for a methylated derivative (biMe, Scheme 5.1) dissolved in methanol (MeOH) blueshifts from 510 to 442 nm upon adding trifluoroacetic acid (TFA), with an increase in emission quantum yield (QY) from 0.10 to 0.24. In contrast, a 2-methoxylated derivative (biOMe) exhibits no significant fluorescence shift and a drop in emission QY from 0.10 to < 0.01 with decrease in pH. The UV-vis and fluorescence spectra of both samples in CH_3OH with TFA titration are displayed in Figure 5.1. With increasing TFA concentration, the intensities of the absorption bands at 274 and 440 nm decrease, while a new band associated with the protonated biOMe centred at 370 nm concurrently emerges (Figure 5.1(a)). Two isosbestic points at 297 and 398 nm manifest one major protonated product being formed during the TFA titration. Figure 5.1(b) presents the fluorescence emission spectra when excited at 370 nm, resonant with absorption of the protonated biOMe. Upon addition of TFA, a new feature becomes apparent at 440 nm with a quantum yield of 0.24. In contrast, biOMe exhibits fairly different acid-responsive fluorescent behaviour. The UV-vis spectra of biOMe with TFA titration, shown in Figure 5.1(c), strongly resemble the absorption changes observed for 3b. However, unlike the increased fluorescence intensity seen for protonated biMe, titration of biOMe with TFA resulted in a sharp decrease in the fluorescence intensity, as shown in Figure 5.1(d). Figure 5.2 plots normalized absorption and fluorescence spectra of protonated biMe and biOMe ($biMeH^+$ and $biOMeH^+$, respectively) in MeOH. A modest absorption redshift from $biMeH^+$ to biOMeH$^+$ [$\Delta E_{Abs} = 584$ cm^{-1}] is attributed to a stronger electronic push-pull effect across biOMeH$^+$. However, the large difference in Stokes' shifts [4403 vs. 6445 cm^{-1}, $\Delta(\Delta E_{Stokes}) = 2042$ cm^{-1}] cannot be attributed to increased charge separation in excited biOMeH$^+$, as emission from both exhibits weak solvatochromism [$\Delta E_{Solv} = 371$ vs. 506 cm^{-1}; Figure 5.1S].

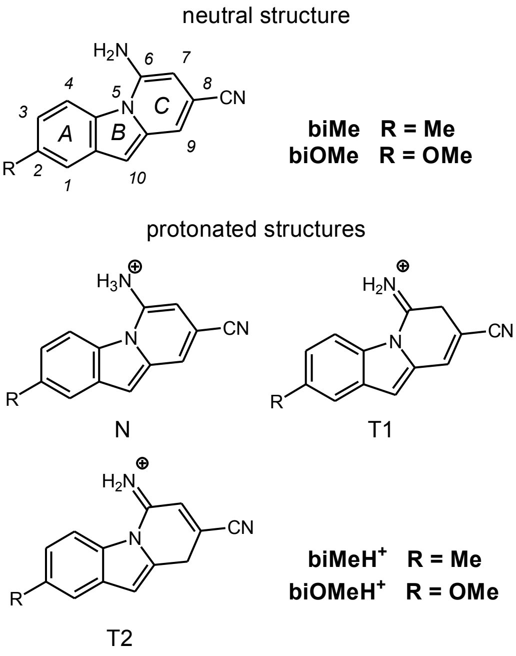
neutral structure
H_2N
6
7
4
5
8
N
C
CN
3
A
B
biMe R = Me
biOMe R = OMe
9
R
2
10
1
protonated structures
$H_3N^\oplus$
CN
N
R
N
$H_2N^\oplus$
N
CN
R
T1
$H_2N^\oplus$
CN
N
biMeH$^+$ R = Me
biOMeH$^+$ R = OMe
R
T2

Scheme 5.1. 6-amino-8-cyanobenzo[1,2-*b*]indolizines (bi) and their protonated amino (N) and methylene (T1, T2) tautomers.

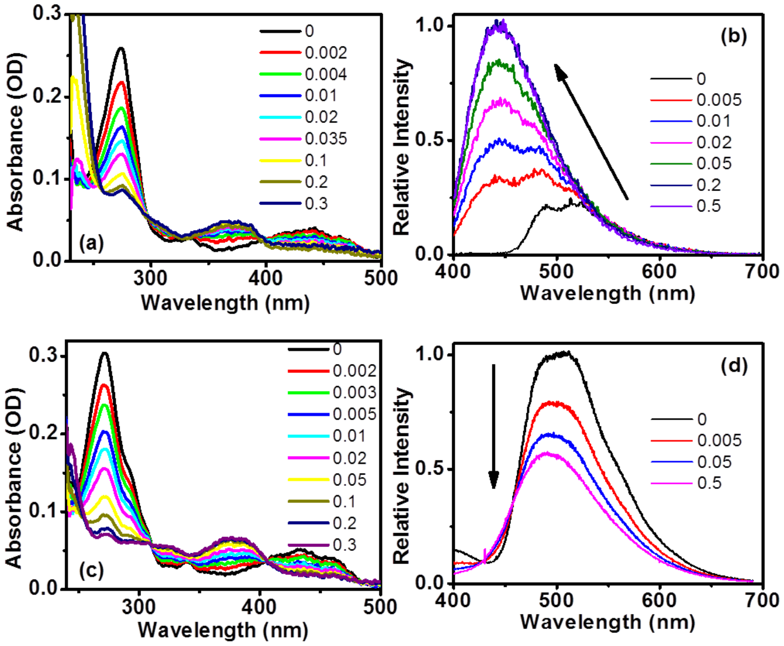

Figure 5.1. (a) UV-Vis and (b) fluorescence spectra of biMe and (c) UV-Vis and (d) fluorescence spectra of biOMe upon addition of TFA (vol %).The concentrations of biMe and biOMe in fluorescence measurement are 5.4 μM and 2.8 μM, respectively.

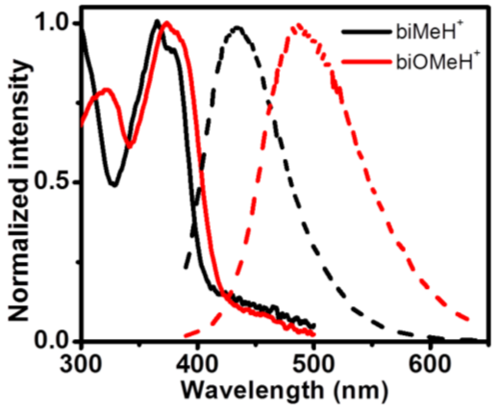

Figure 5.2. Normalized absorption (solid) and dispersed fluorescence (dashed) of biMeH$^+$ and biOMeH$^+$ in MeOH. Fluorescence excitation – 370 nm.

NMR spectra of both protonated compounds in CD_3CN reveal a loss of C-ring aromaticity to yield a methylene (T1 or T2) – not amino (N) – tautomer.[10] Only one protonated species of either compound is observed; however, ^1H signals from the amino, C-7, and C-9 sites disappear for CD_3OD solutions, indicating facile H/D exchange at each of these sites (Figure 5.2S). Quantum-chemical computations illuminate the relative energies of protonated tautomers in their ground (S_0) and first electronically excited (S_1) states, as well as their vertical absorption and emission gaps (Table 5.1). The structures and relative energies of S_0 and S_1 N, T1 and T2 are similar for biMeH$^+$ and biOMeH$^+$: T1 has the lowest ground-state energy for both systems. In contrast, T2 has the lowest energy in the excited state for both protonated compounds and the smallest emission gap. Our calculations reveal that conversion from T1 to T2 is downhill energetically for both excited, protonated compounds. In contrast, the N tautomer has the highest calculated excited-state energy, and conversion of T1 or T2 to N would increase the emission gap.

Table 5.1. Calculated Energies, Absorption and Emission Gaps/Wavelengths of N, T1, T2, and C-8 Protonated (Int) Tautomers of biMeH$^+$ and biOMeH$^+$ in MeOH (DFT/TDDFT at CAM-B3LYP/6-31G*/PCM).

	biMeH$^+$				**biOMeH$^+$**			
Tautomer	N	T1	Int	T2	N	T1	Int	T2
S_0 (eV)	0.68	0	1.49	0.19	0.67	0	1.50	0.236
S_1 (eV)	3.51	3.14	2.99	2.71	3.55	3.08	2.99	2.73
$S_0 \rightarrow S_1$* (eV/nm)	3.25/381	3.80/326	2.15/576	3.23/384	3.29/377	3.71/334	2.08/595	2.72/382
$S_1 \rightarrow S_0$* (eV/nm)	2.56/484	2.44/509	0.55/2259	1.72/723	2.63/472	2.38/521	0.51/2421	1.76/704

Our computational results suggest that the different emission Stokes' shifts for biOMeH$^+$ and biMeH$^+$ may be due to emission from different tautomers. We therefore used ultrafast spectroscopy to probe photochemical dynamics of both systems to look for signs of excited-state tautomerization. TA spectra of biMeH$^+$ excited at 360 nm are presented in Figure 5.2. A negative feature peaks below 500 nm near the peak position of dispersed fluorescence (Figure 5.2) and is ascribed to $S_1 \rightarrow S_0$* stimulated emission (SE). The difference in fluorescence and SE peak positions arises from overlap of the latter with excited-state absorption (ESA) that spans the visible and dominates spectra at the shortest wavelengths probed. The SE position redshifts from 440 to 480 nm and ESA above 500 nm decays in the 20 ps that follow excitation (Figure 5.3(a), Figure 5.3S). Spectra do not change appreciably between 50 ps and 1 ns (Figure 5.3(b)), indicating that biMeH$^+$ relaxes to a long-lived state. A single-exponential fit to the SE position vs. time yields a spectral relaxation time of 3.7 ps (Figure 5.4S). Notably, TA spectroscopy of biMe and biMeH$^+$ are distinctly different (Figure 5.5S).

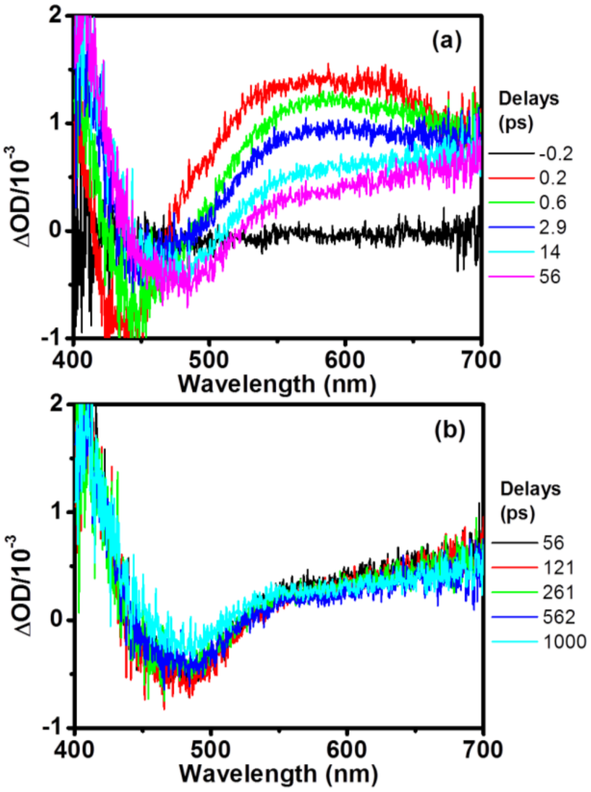

Figure 5.3. TA spectroscopy of biMeH$^+$ in MeOH following 360 nm excitation (a) ~ 0 – 56 ps (b) ~ 56 – 1000 ps

Figure 5.4 presents the TA spectroscopy of biOMeH$^+$ excited at 360 nm. At 200 fs the TA spectrum consists of SE peaked at 450 nm flanked by absorption below and above 420 and 510 nm, respectively. The SE position shifts dramatically from 450 to 560 nm within a few picoseconds, resulting in a spectrum dominated by ESA below 500 nm. Global Analysis with a three-state kinetic model ($A \rightarrow B \rightarrow C$) was applied to spectra collected between 0.15 and 21 ps, returning (exponential) kinetic interconversion lifetimes of 0.21 and 2.6 ps (Figure 5.4(a)). The short-lived spectral component obtained from this analysis, A, is similar to the TA spectrum of unrelaxed biMeH$^+$ (Figure 5.3(a), Figure 5.6S); intermediate component B is similar to C but blueshifted. SE and ESA of excited biOMeH$^+$ decay with a 295-ps lifetime, with residual absorption below 500 nm remaining after SE disappears (Figure 5.4(b), Figure 5.7S). TA spectroscopy of biOMe and biOMeH$^+$ likewise differ qualitatively (Figure 5.8S).

Our analyses of TA spectra from biMeH$^+$ and biOMeH$^+$ indicate initial preparation of excited species with similar emission gaps. The SE band for excited biMeH$^+$ red shifts modestly with time, whereas that of biOMeH$^+$ evolves dramatically. Although the SE peak position of neither species matches the corresponding fluorescence maximum due to overlapping ESA, the differences in emission energy from the two methods roughly agree ($\Delta E_{SE} = 2868$ vs. $\Delta E_{FL} = 2544$ cm^{-1}).

We therefore interpret TA data as follows: the modest SE shift observed for biMeH$^+$ is consistent with vibrational relaxation or dynamic solvation of long-lived S_1 T1.[11, 12] In contrast, the dramatic spectral evolution observed for biOMeH$^+$ reflects substantial structural changes in the excited state that we ascribe to T1-to-T2 tautomerization. Spectral dynamics in Figure 5.4(a) do not exhibit isosbestic behavior and can only be fit by adding an intermediate component, B. Non-isosbestic behavior can be due to vibrational relaxation or dynamic solvation in the excited state that is concurrent with or follows tautomerization; we expect that both molecules should exhibit such relaxation, and indeed similar relaxation timescales (3.7 and 2.6 ps) are extracted from our spectral analyses for excited biMeH$^+$ and biOMeH$^+$. Alternatively, *B* could correspond with a short-lived intermediate structure. The difference in excited-state lifetimes further supports that these species emit from different tautomers. Finally, the residual absorption below 500 nm following decay of excited biOMeH$^+$ is consistent with an S_0 T2-T1 difference spectrum given the relative energies of the calculated vertical excitation gaps.

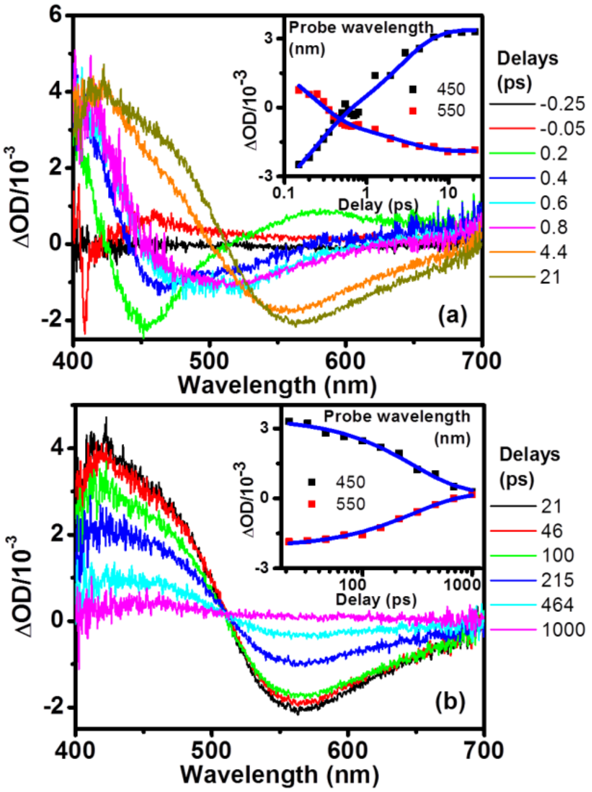

Figure 5.4. TA spectroscopy of biOMeH$^+$ in MeOH following 360 nm excitation (a) ~ 0 – 21 ps (b) ~ 21 – 1000 ps. Insets: Experimental data at selected probe wavelengths (symbols) compared with global fits (solid lines) from three- and two-state interconversion models in (a) and (b), respectively.

Various controls clarify the tautomerization mechanism. biOMeH$^+$ fluoresces similarly in solvents that can serve as H$^+$ donors, acceptors or neither (Figure 5.1S), implying that tautomerization does not require solvent-assisted proton transfer (PT).[13] Furthermore, biOMeH$^+$ fluorescence reveals no changes in band shape or position across a large biOMe concentration range (2.5-240 μM) with excess TFA (Figure 5.9S). If dimers facilitate tautomerization (by intermolecular PT), we would expect fluorescence similar to biMeH$^+$ at low concentrations.[13] Finally, a large local TFA concentration would be required for a reliable intermolecular PT network to facilitate tautomerization.

We also recognize that there should be some ion-pair interaction between biOMeH$^+$ and the trifluoroacetate counter-ion (TFA-) in organic solvents,[14, 15] such that tautomerization might occur by PT via TFA-. However, the TFA- is more likely to interact with the iminium group, as natural population analysis (NPA)[16] of computed structures reveals that the iminium carries most of the formal positive charge in S_0 biOMeH$^+$ (Table 5.16S). Furthermore, we expect different distributions of ion-pair types (e.g. contact, solvent-separated, free) in various media;[14, 17] presumably only contact pairs would enable ultrafast PT back to TFA-, while solvent-separated pairs would have different behavior. Hence PT via TFA- does not seem to be a plausible pathway for ultrafast tautomerization. Finally, significant differences in the TA spectroscopy (Figure 5.8S) and fluorescence of biOMe and biOMeH$^+$ indicate that the dynamics are not due to excited-state quenching by PT to TFA- to create excited biOMe.

We conclude that S_1 tautomerization of biOMeH$^+$ is an intramolecular process. As C-7 and C-9 are at the ends of an allylic moiety, S_1 T1-to-T2 interchange occurs by *net* [1,3] H shift. Orbital-symmetry correlations predict that photoinduced suprafacial [1,3] H shift is allowed,[18] but this rearrangement could alternatively involve photoinduced C-to-C PT coupled with electronic rearrangement within the allylic moiety. Calculated minimum-energy structures support the feasibility of either mechanism (Figure 5.5): the C-ring remains roughly planar in the ground state, with the C-H bond at C-7 oriented 38° relative to the plane of the ring. C-7 moves above the plane in excited T1, such that the C-H bond is oriented almost perpendicular to the rest of the C-ring and proximal to the pi-cloud of the neighboring bond between C-8 and C-9. This leaves the H (or H^+) poised for suprafacial transfer to C-9. Thus, the two-step dynamics observed spectroscopically can be interpreted as a rapid net H shift followed by relaxation of nascent S_1 T2.

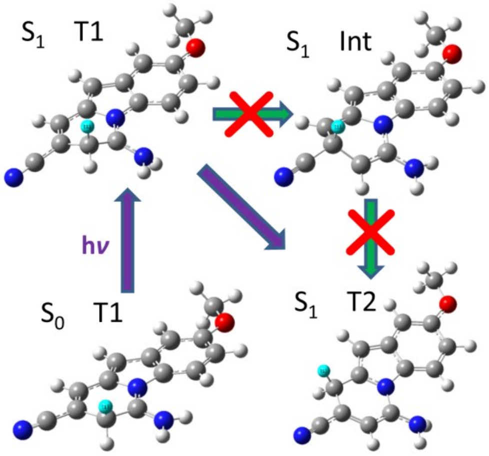

Figure 5.5. Optimized structures of S_0 T1, and S_1 T1, a C-8 protonated intermediate (Int), and T2. The H shifted is highlighted in light blue.

We also found a stable, excited-state tautomer in which the extra H resides at C-8 (Figure 5.5, Int). This structure's energy lies between that of excited T1 and T2, such that H shift might rather occur by a two-step transfer (C-7 to C-8 to C-9) that would also match observed kinetics. However, the calculated SE gap for Int is quite small due to its relative instability in S_0. Hence, this mechanism does not match our observables.

The driving force for the shift is presumably greater conjugation and lower S_1 energy in T2. However, our calculations predict the same relative tautomer energies for

S_1 biMeH$^+$, which does not tautomerize. Fluorescence spectra from a series of biXH$^+$, where X are substituents with electron-donating strengths somewhat weaker than methoxyl, fluoresce like biMeH$^+$ (Figure 5.10S). These discrepancies indicate that the strongly donating methoxyl must uniquely lower the tautomerization barrier. Higher-level calculations are required to chart the H-shift coordinate and how the electronic push-pull effect introduced by methoxyl lowers the energetic barrier.

In sum, we used ultrafast spectroscopy and quantum-chemical calculations to elucidate the photochemistry underlying disparate photophysics of biMeH$^+$ and biOMeH$^+$ in solution. Dramatic TA spectral evolution observed for biOMeH$^+$ results from an ultrafast, net [1,3] H shift not active in biMeH$^+$. Although photoinduced suprafacial [1,3] H shift is predicted to be symmetry-allowed it is virtually unreported in the literature; biOMeH$^+$ and analogues may present possibilities for further fundamental exploration of this mechanism – or, alternatively, a likewise unusual C-to-C PT. We note that this rearrangement quenches a pH-dependent emission shift observed with other bi compounds. We hypothesize that chemical interactions or binding that modulate the donating strength of a methoxyl or hydroxyl substituent could suppress the H shift; thus, the photophysics of biOMeH$^+$ could be useful for surface- or binding-specific acid-responsive tagging.

5.5. Supporting material

5.5.1. Dispersed fluorescence spectra of biMeH$^+$ and biOMeH$^+$ in CH_3CN, $CHCl_3$, toluene and CH_3OH

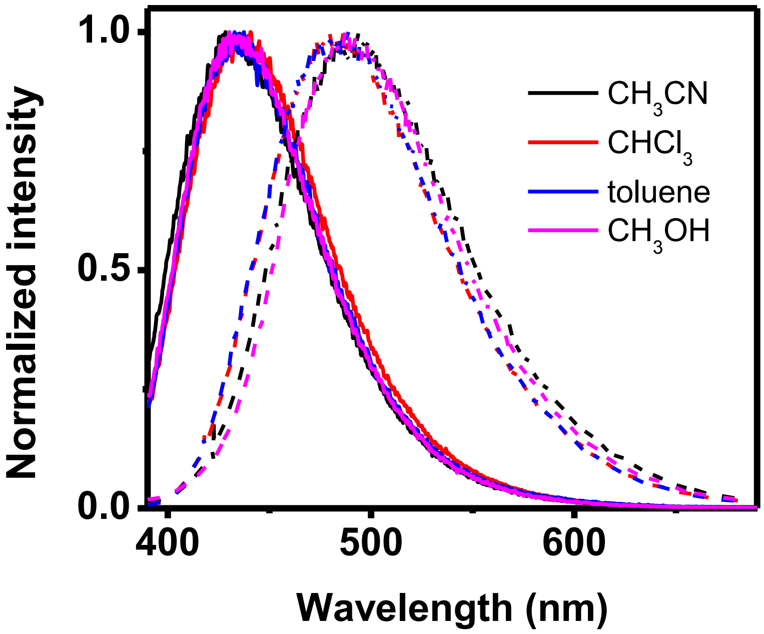

Figure 5.1S. Normalized dispersed fluorescence spectra of biMeH$^+$ (solid lines) and biOMeH$^+$ (dash lines) dissolved in CH_3CN, $CHCl_3$, toluene and CH_3OH excited at 360 nm. Neither sample exhibits significant solvatochromism relative to the large difference in emission peak for these two species.

5.5.2. NMR spectra of neutral and protonated biMe and biOMe in CD_3OD

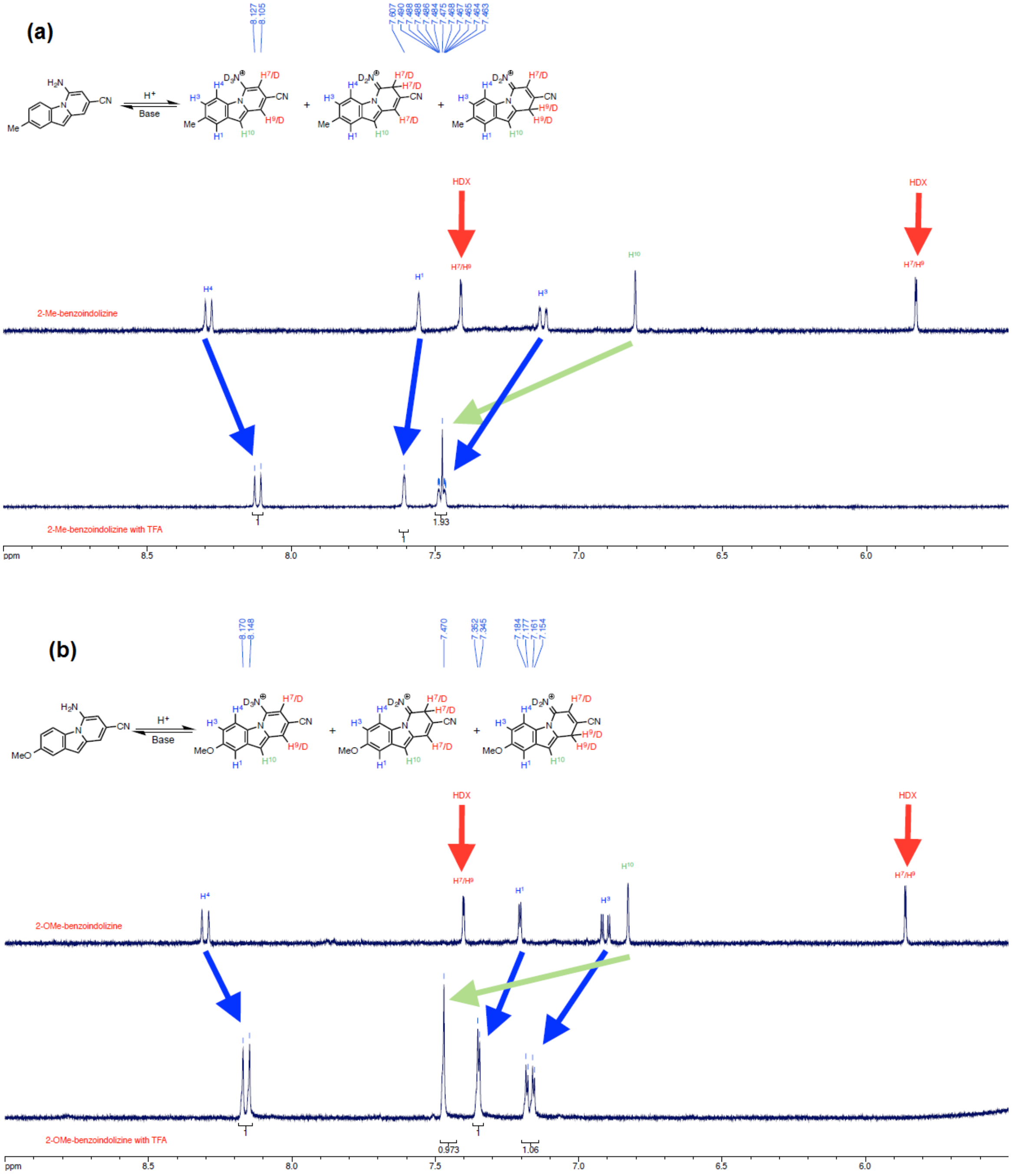

Figure 5.2S. NMR analysis of (a) $biMeH^+$ and (b) $biOMeH^+$ in CD_3OD. Red arrows denote features that disappear due to facile H/D exchange.

5.5.3. Fitting of time-dependence of biMeH$^+$ excited-state absorption (ESA) following 360-nm excitation

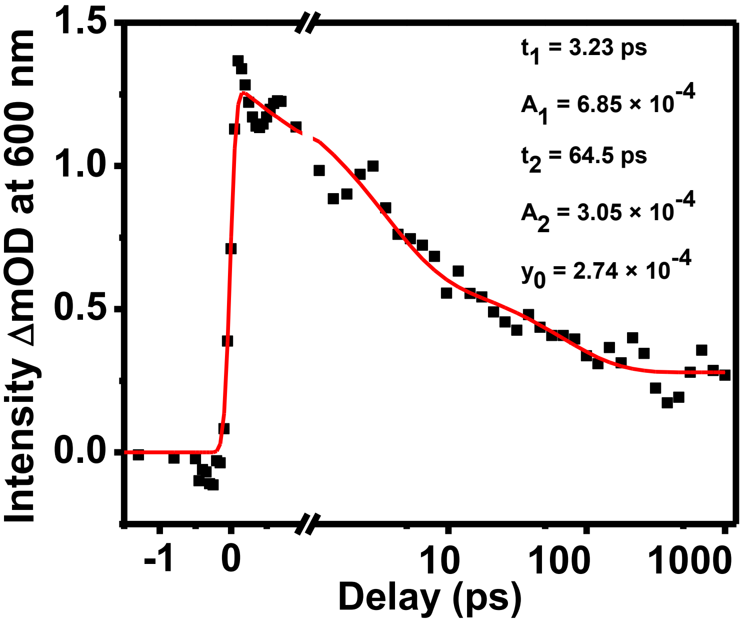

Figure 5.3S. Excited-state absorption (ESA) of biMeH$^+$ in methanol as probed by TAS at 600 nm following 360-nm excitation. Time-dependent absorption (symbols) was fit with a convoluted biexponential function (red line), yielding decay time scales of 3.2 and 65 ps. The former dominates the decay and is consistent with the time-dependent shift in SE, whereas the latter may be associated with further vibrational cooling of the long-lived excited state.

5.5.4. Fitting of transient shift in SE peak position for biMeH$^+$ following 360-nm excitation

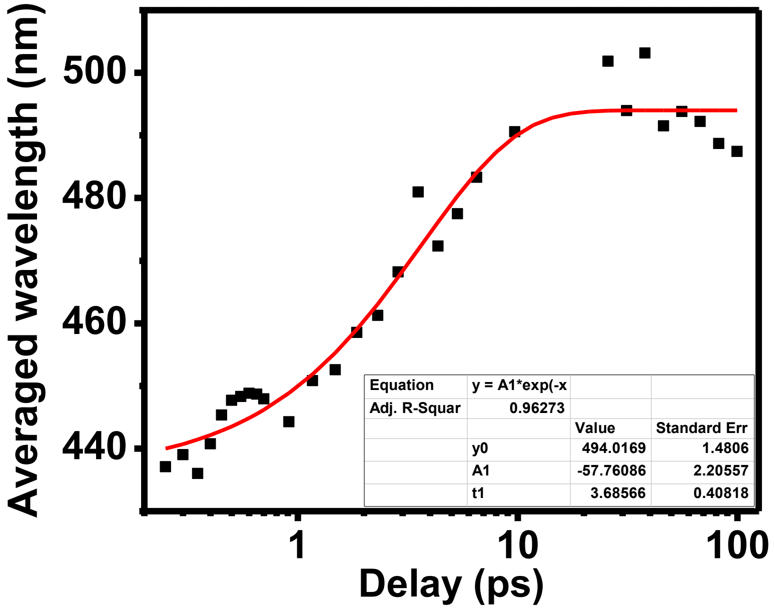

Equation	y = A1*exp(-x		
Adj. R-Squar	0.96273		
		Value	Standard Err
	y0	494.0169	1.4806
	A1	-57.76086	2.20557
	t1	3.68566	0.40818

Figure 5.4S. Single exponential fit of the intensity-weighted averaged wavelength of the SE band (averaged from 425 to 500 nm region) as measured following 360-nm excitation of biMeH$^+$ in CH_3OH.

5.5.5. TAS of biMe in CH_3OH following 360-nm excitation

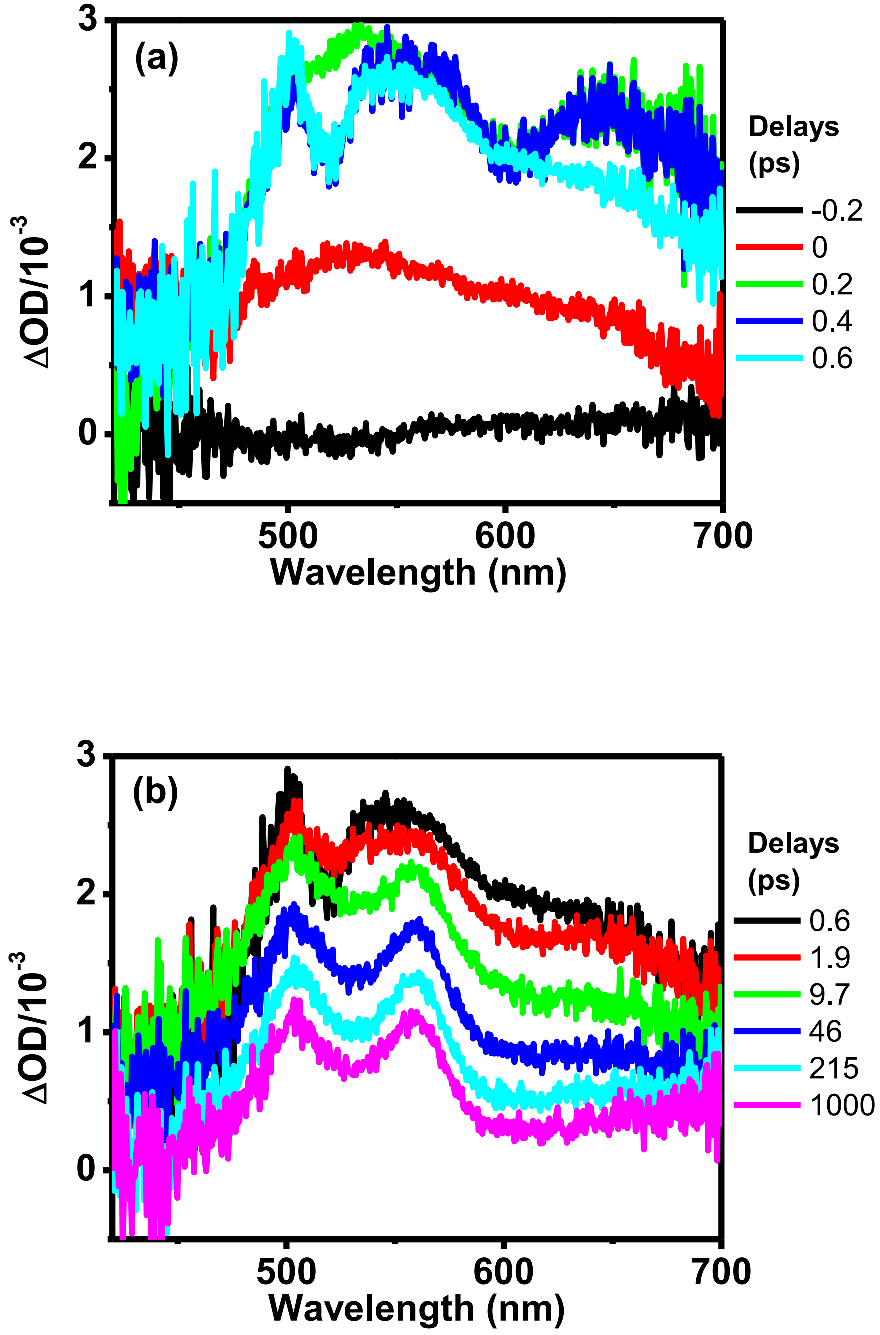

Figure 5.5S. TA spectra of neutral biMe in CH_3OH following 360 nm excitation (a) ~ 0 – 0.6 ps (b) ~ 0.6 – 1000 ps.

5.5.6. Decay-associated spectra obtained from global analysis of biOMeH$^+$ TAS (~ 0 – 21 ps) following 360-nm excitation

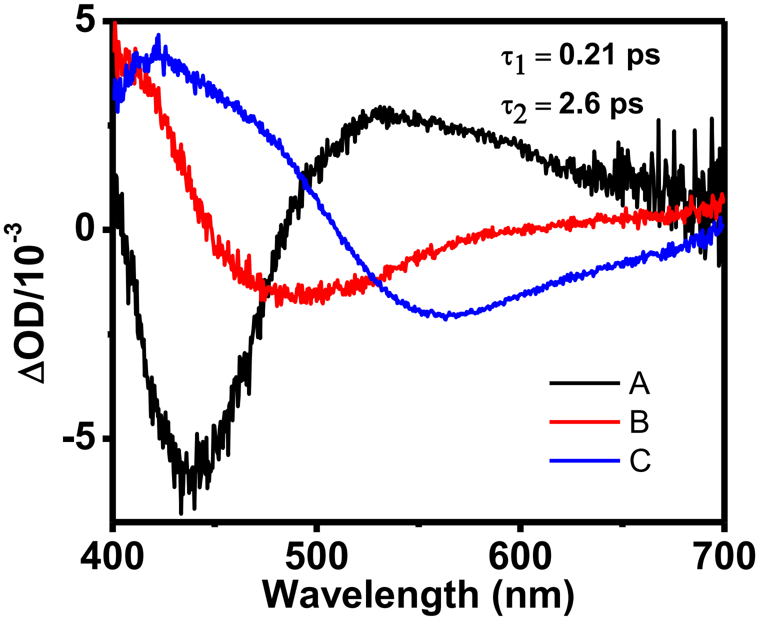

Figure 5.6S. Decay-associated spectra obtained by global analysis of TAS of biOMeH$^+$ in CH_3OH ~ 0 – 21 ps following 360 nm excitation. Global analysis used a sequential kinetic interconversion model (A→B→C).

5.5.7. Decay-associated spectra from global analysis of biOMeH$^+$ TAS 21 – 1000 ps following 360-nm excitation

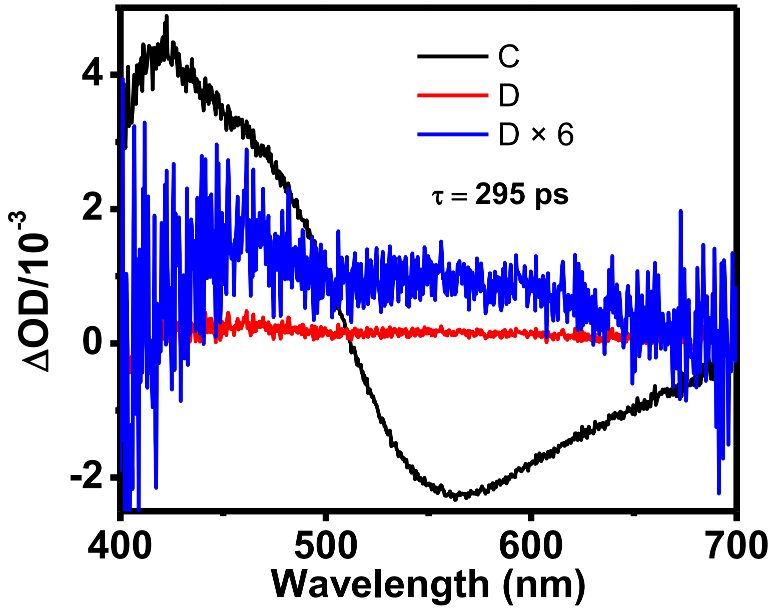

Figure 5.7S. Decay-associated spectra obtained by global analysis of TAS of biOMeH$^+$ in CH_3OH 21-1000 ps following 360-nm excitation. Global analysis used a sequential kinetic interconversion model (C→D).

5.5.8. TAS of biOMe in CH_3OH following 360-nm excitation

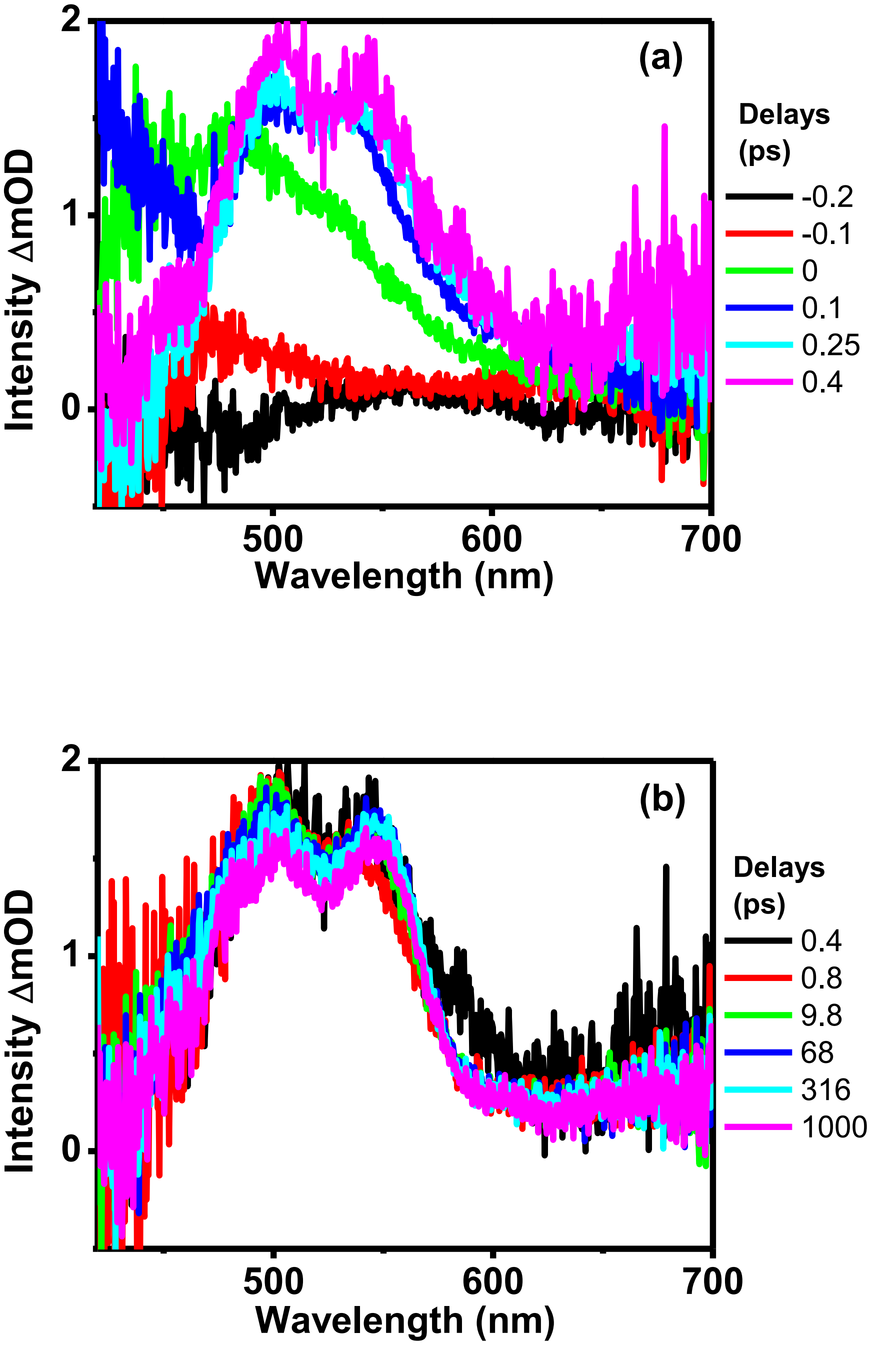

Figure 5.8S. TA spectra of neutral biOMe in CH_3OH following 360 nm excitation (a) ~ 0 – 0.4 ps (b) ~ 0.4 – 1000 ps.

5.5.9. Concentration-dependent fluorescence spectroscopy of biOMeH$^+$ in CH_3OH

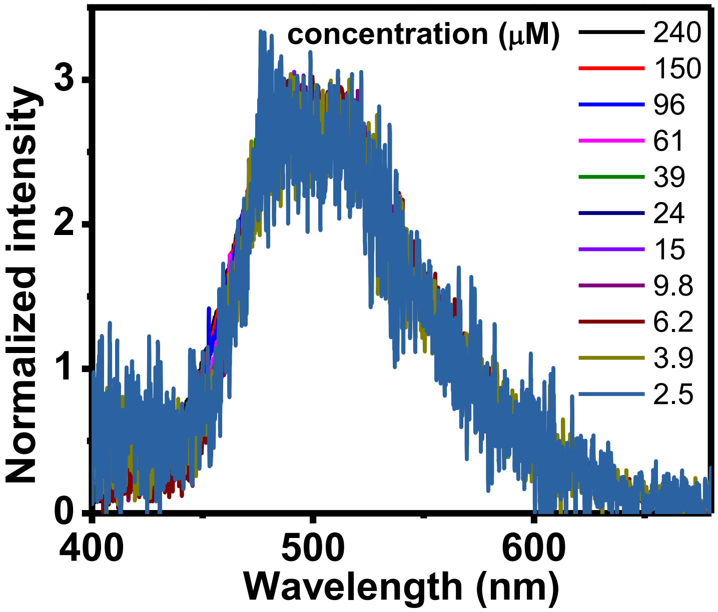

Figure 5.9S. Normalized dispersed fluorescence spectra of biOMeH$^+$ in CH_3OH excited at 370 nm. No noticeable change in either band shape or band position is observed while the biOMeH$^+$ concentration is decreased from 240 to 2.5 μM.

5.5.10. Acid-responsive optical properties of other benzo[1,2-*b*]indolizines compounds

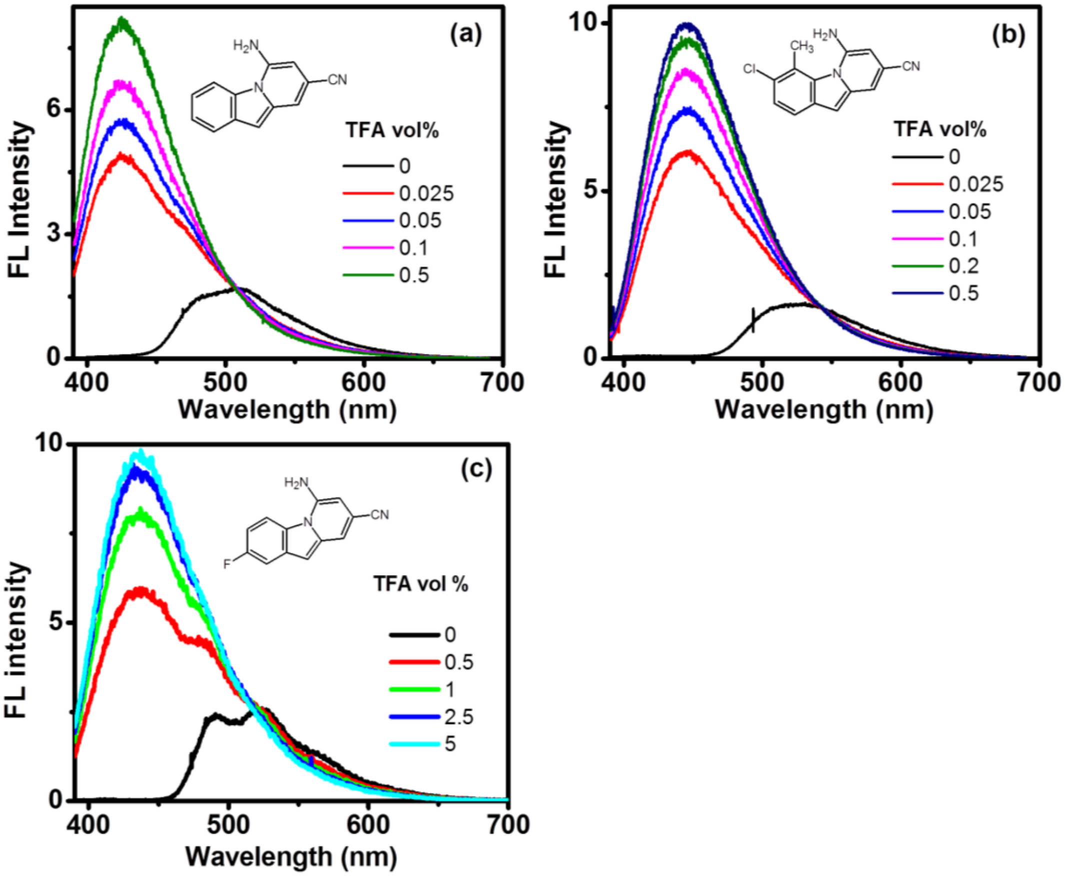

Figure 5.10S. Fluorescence spectra excited at 370 nm of other benzo[1,2-b]indolizines compounds with TFA (vol %) titration in methanol. Their structures are displayed in the inset.

5.5.11. Quantum-chemical calculations

The ground-state geometries of the three tautomers (N, T1, and T2) for each protonated compound were optimized by DFT. All computational geometry optimizations were performed at the CAM-B3LYP/6-31G* level with Polarizable Continuum Model (PCM) to incorporate the effect of CH_3OH using the Gaussian 09 package.[16] TDDFT was then used to calculate the vertical $S_0 \rightarrow S_1^*$ (absorption) gap, optimize the minimum-energy S_1 structure, and calculate the $S_1 \rightarrow S_0^*$ (emission) gap for each tautomer.

5.5.11.1 Ground-state optimization of S_0 biMeH$^+$ and biOMeH$^+$ in three tautomeric structures (N, T1 and T2)

S_0 geometry optimization of biMeH$^+$ and biOMeH$^+$ was performed without symmetry constraints. No imaginary frequencies were found at the optimized structures for all tautomers.

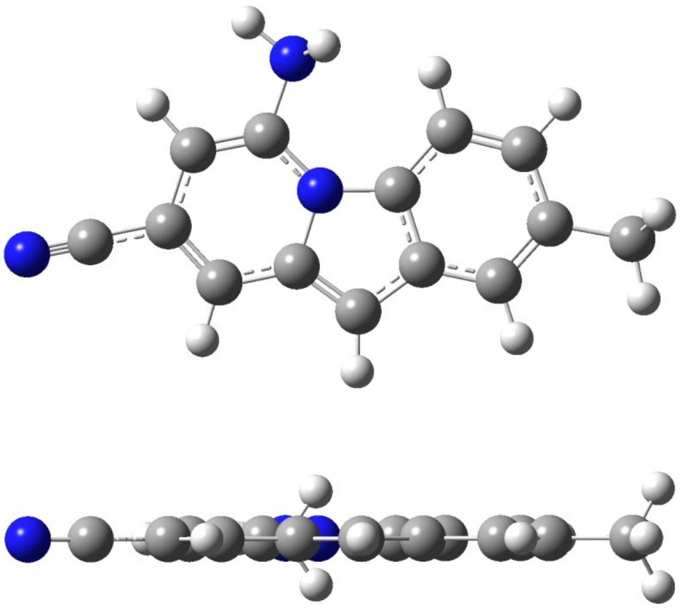

Figure 5.11S. S_0 optimized structure of biMeH$^+$ (N) viewed from top (above) and side (bottom).

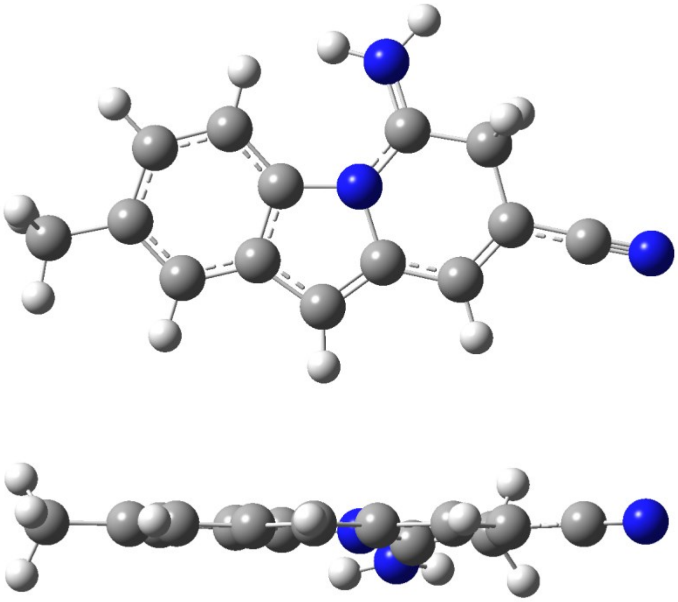

Figure 5.12S. S_0 optimized structure of biMeH$^+$ (T1) viewed from top (above) and side (bottom).

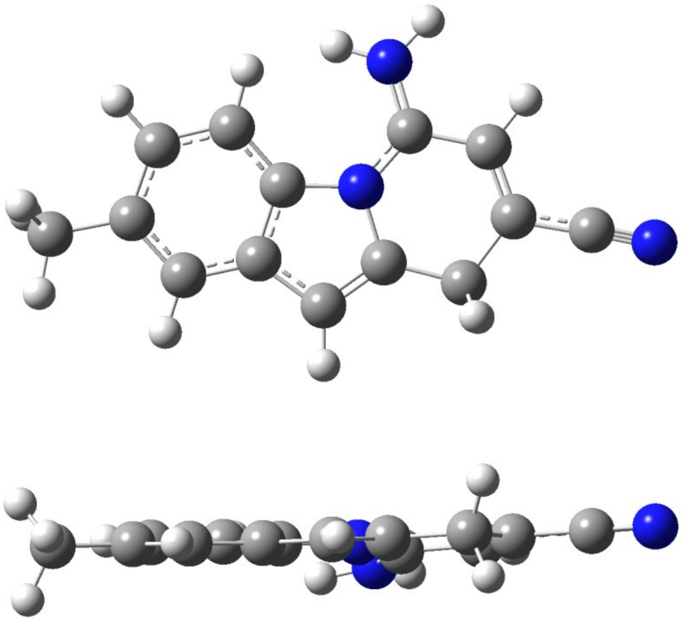

Figure 5.13S. S_0 optimized structure of biMeH$^+$ (T2) viewed from top (above) and side (bottom).

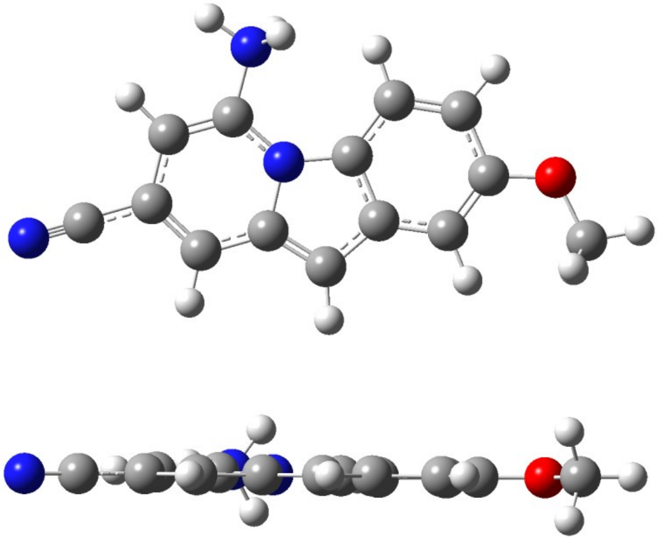

Figure 5.14S. S_0 optimized structure of biOMeH$^+$ (N) viewed from top (above) and side (bottom).

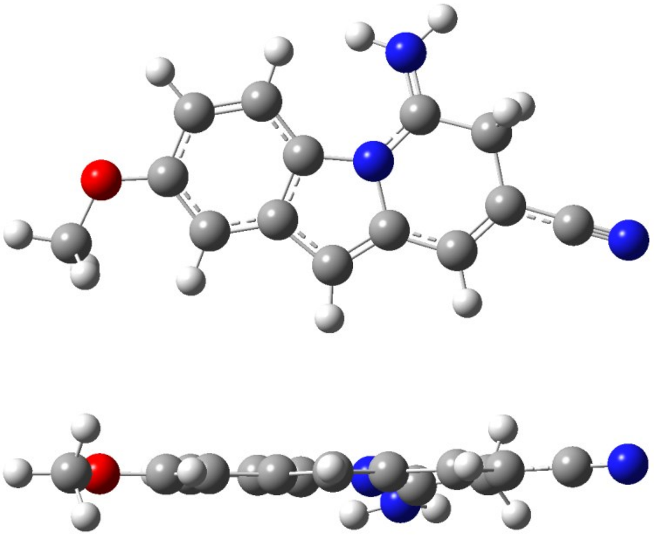

Figure 5.15S. S_0 optimized structure of biOMeH$^+$ (T1) viewed from top (above) and side (bottom).

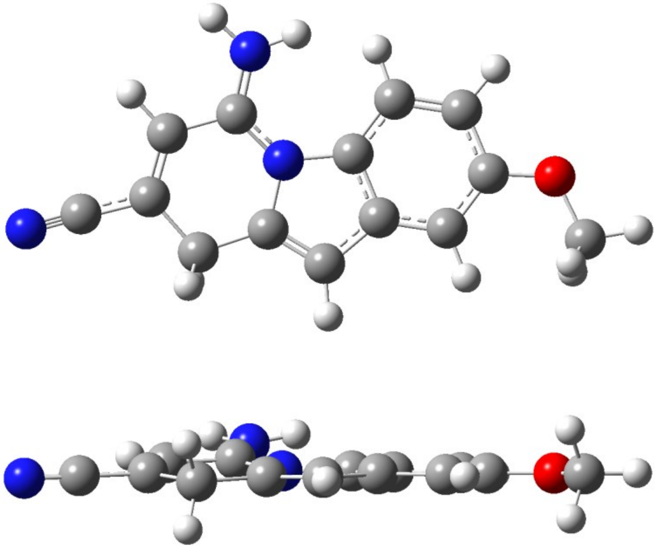

Figure 5.16S. S_0 optimized structure of biOMeH$^+$ (T2) viewed from top (above) and side (bottom).

5.5.11.2 Time-dependent density functional theory (TD-DFT) optimization of S_1 biMeH$^+$ and biOMeH$^+$ in three tautomers (N, T1, and T2) and one intermediate (Int) structure

S_1 geometry optimization of biMeH$^+$ and biOMeH$^+$ was performed without symmetry constraints. No imaginary frequencies were found at the optimized structures for all tautomers.

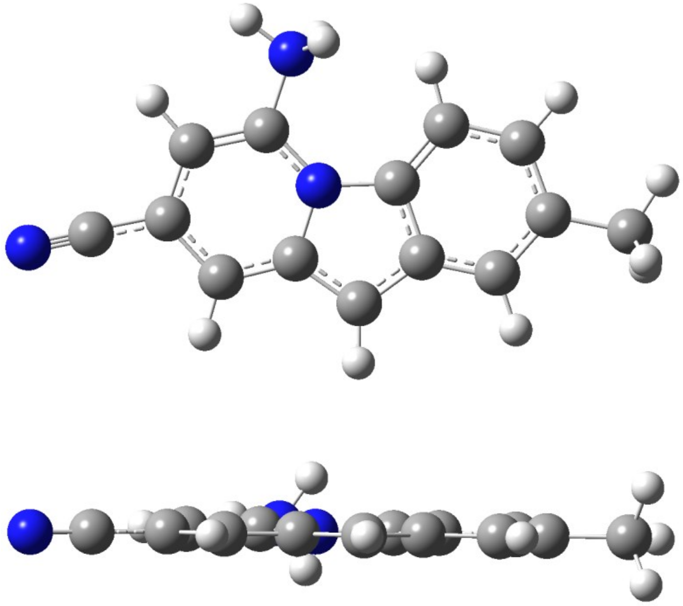

Figure 5.17S. S_1 optimized structure of $biMeH^+$ (N) viewed from top (above) and side (bottom).

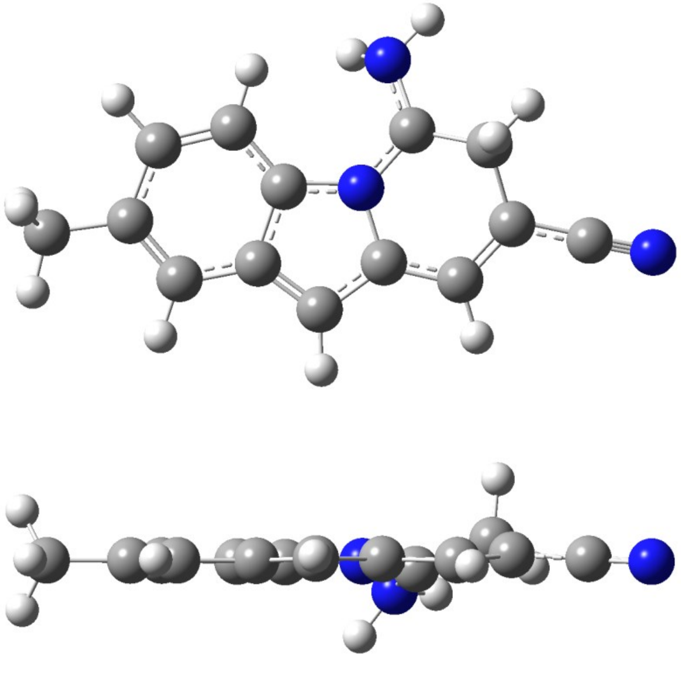

Figure 5.18S. S_1 optimized structure of $biMeH^+$ (T1) viewed from top (above) and side (bottom).

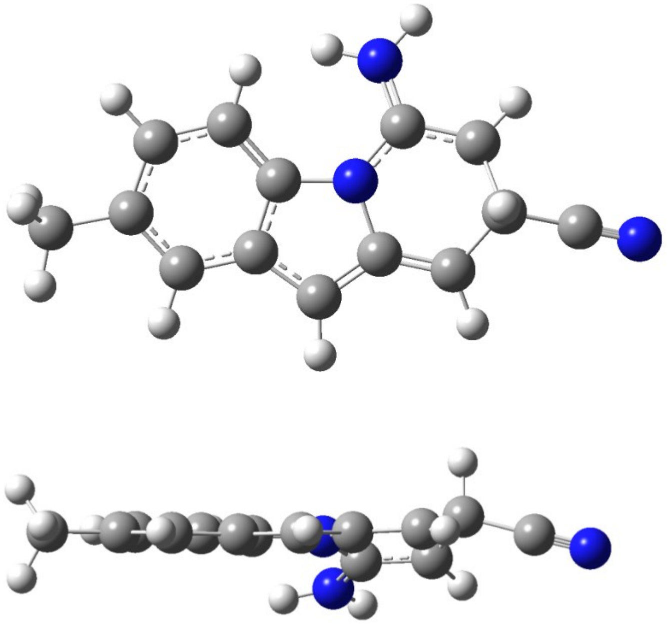

Figure 5.19S. S$_1$ optimized structure of biMeH$^+$ (Int) viewed from top (above) and side (bottom).

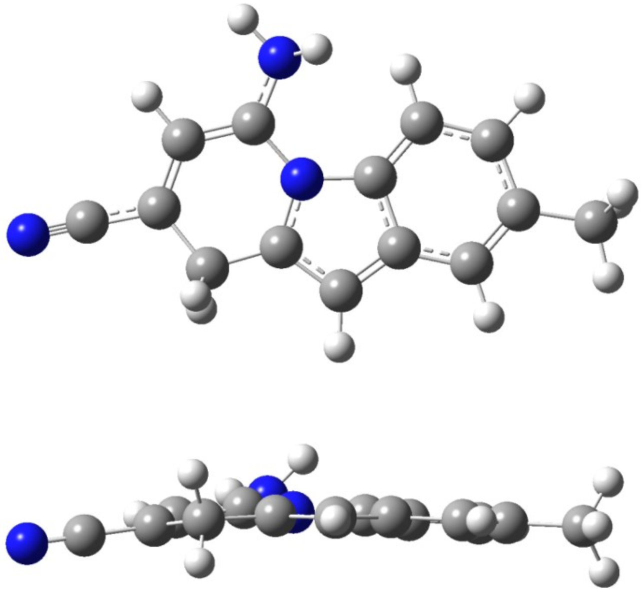

Figure 5.20S. S$_1$ optimized structure of biMeH$^+$ (T2) viewed from top (above) and side (bottom).

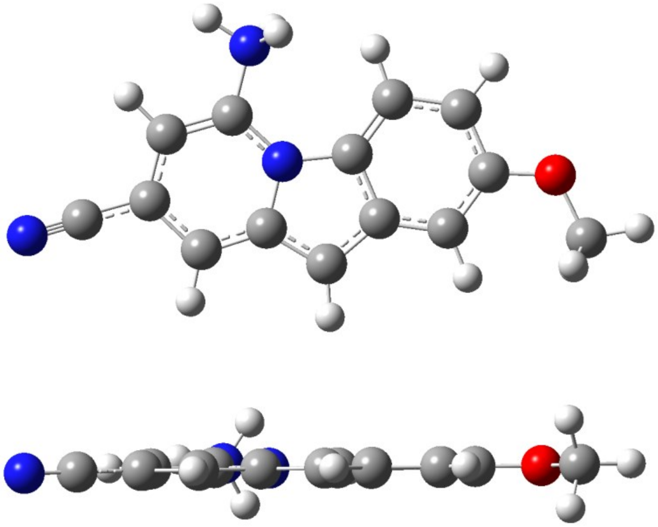

Figure 5.21S. S_1 optimized structure of biOMeH$^+$ (N) viewed from top (above) and side (bottom).

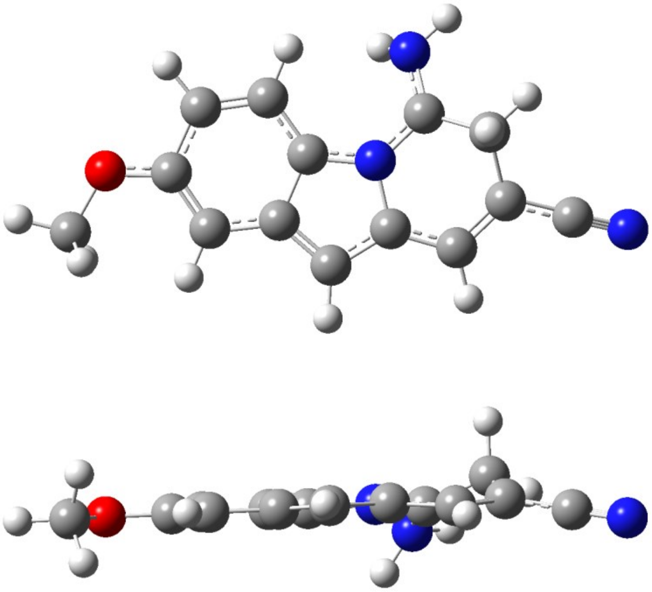

Figure 5.22S. S_1 optimized structure of biOMeH$^+$ (T1) viewed from top (above) and side (bottom).

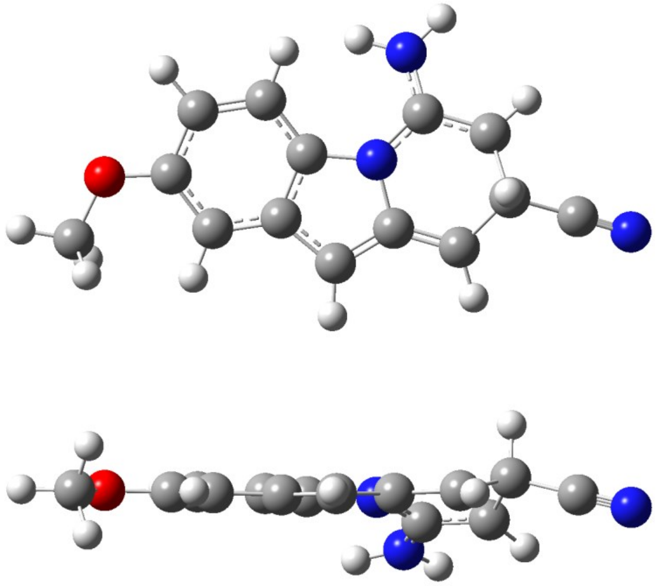

Figure 5.23S. S_1 optimized structure of biOMeH$^+$ (int) viewed from top (above) and side (bottom).

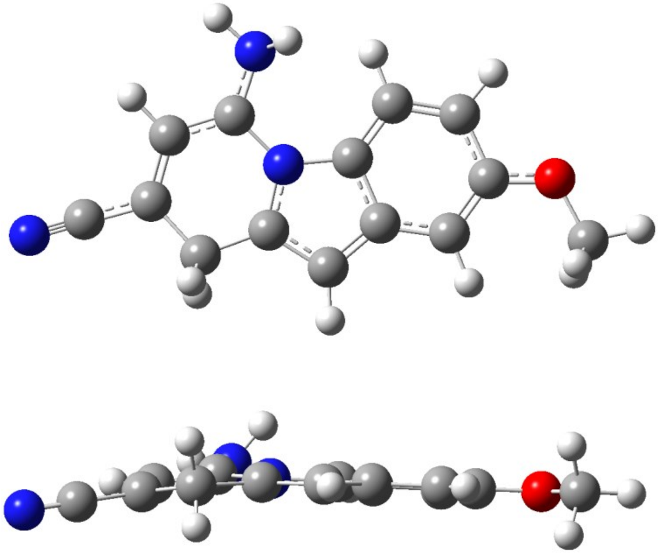

Figure 5.24S. S_1 optimized structure of biOMeH$^+$ (T2) viewed from top (above) and side (bottom).

5.5.11.3 Nature population analysis (NPA) of biMeH$^+$ and biOMeH$^+$ T1 tautomeric structures in the first excited state

The NPA method is employed to analyze the charge distribution in the enamine (C6-NH$_2$), methylene (C7-H$_2$) and methine (C9-H) groups and individual hydrogens. The numbers are tabulated below.

Table 5.15S. Sums of natural charges for enamine (C6-NH$_2$), methylene (C7-H$_2$) and methine (C9-H) groups in the T1 tautomeric structure of the S$_0$ and S$_1$ biMeH$^+$ and biOMeH$^+$.

	S$_0$ biMeH$^+$	**S$_1$ biMeH$^+$**	**S$_0$ biOMeH$^+$**	**S$_1$ biOMeH$^+$**
C6-NH$_2$	0.834	0.449	0.829	0.498
C7-H$_2$	0.101	0.048	0.100	0.049
C9-H	0.139	0.110	0.138	0.107

Table 5.16S. Natural charges for hydrogen in the T1 tautomeric structure of the S$_1$ biMeH$^+$ and biOMeH$^+$.

	biMeH$^+$	**biOMeH$^+$**
H1	0.267	0.274
H3	0.266	0.278
H4	0.280	0.284
NH$_2$	0.435/0.445	0.439/0.450
H7	0.284/0.297	0.280/0.294
H9	0.298	0.296
H10	0.287	0.284

5.6 References

(1) Valeur, B.; Leray, I. *Coord. Chem. Rev.* **2000**, *205*, 3.

(2) Callana, J. F.; Silva, A. P. d.; Magria, D. C. *Tetrahedron* **2005**, *61*, 8551.

(3) Demchenko, A. P.; Tang, K. C.; Chou, P. T. *Chem. Soc. Rev.* **2013**, *42*, 1379.

(4) Oscar, B. G.; Liu, W.; Zhao, Y.; Tang, L.; Wang, Y.; Campbell, R. E.; Fang, C. *Proc. Nat. Acad. Sci.* **2014**, *111*, 10191.

(5) McAnaney, T. B.; Park, E. S.; Hanson, G. T.; Remington, S. J.; Boxer, S. G. *Biochemistry* **2002**, *41*, 15489.

(6) Remington, S. J. *Protein Science* **2011**, *20*, 1509.

(7) Yoon, E.; Konold, P. E.; Lee, J.; Joo, T.; Jimenez, R. *J. Phys. Chem. Lett.* **2016**, *7*, 2170.

(8) Zhao, Y.; Zhang, B.; Duan, C.; Lin, Z.; Meng, Q. *New. J. Chem.* **2006**, *30*, 1207.

(9) Liu, K.; Zhao, X.; Liu, Q.; Huo, J.; Zhu, B.; Diao, S. *Beilstein J. Org. Chem.* **2015**, *11*, 563.

(10) Outlaw, V. K.; Zhou, J.; Bragg, A. E.; Townsend, C. A. *RSC Advances* **2016**.

(11) Outlaw, V. K.; Townsend, C. A. *Org. Lett.* **2014**, *16*, 6334.

(12) Outlaw, V. K.; d'Andrea, F. B.; Townsend, C. A. *Org. Lett.* **2015**, *17*, 1822.

(13) Yu, W.; Zhou, J.; Bragg, A. E. *J. Phys. Chem. Lett.* **2012**, *3*, 1321.

(14) Yu, W.; Donohoo-Vallett, P. J.; Zhou, J.; Bragg, A. E. *J. Chem. Phys.* **2014**, *141*, 044201.

(15) Zhou, J.; Guo, X.; Katz, H. E.; Bragg, A. E. *J. Am. Chem. Soc.* **2015**, *137*, 10841.

(16) In Gaussian09, RevisionA.1: M. J. Frisch, et al. Gaussian, Inc., Wallingford CT, 2009.

(17) Rosspeintner, A.; Lang, B.; Vauthey, E. *Annu. Rev. Phys. Chem.* **2013**, *64*, 247.

(18) Stratt, R. M.; Maroncelli, M. *Journal of Physical Chemistry* **1996**, *100*, 12981.

(19) Vetokhina, V.; Dobek, K.; Kijak, M.; Kaminska, I. I.; Muller, K.; Thiel, W. R.; Waluk, J.; Herbich, J. *ChemPhysChem* **2012**, *13*, 3661.

(20) Marcus, Y.; Hefter, G. *Chemical Reviews* **2006**, *106*, 4585.

(21) Nagya, P. I.; Takacs-Novak, K. *J. Am. Chem. Soc.* **2000**, *122*, 6583.

(22) Foster, J. P.; Weinhold, F. *J. Am. Chem. Soc.* **1980**, *102*, 7211.

(23) Ciccotti, G.; Ferrario, M.; Hynes, J. T.; Kapral, R. *J. Chern. Phys.* **1990**, *93*, 7137.

(24) Woodward, R. B.; Hoffmann, R. *Angew. Chem. Int. Ed. Engl.* **1969**, *8*, 781.

Curriculum Vitae

Mr. Jiawang Zhou

Email: jzhou24@jhu.edu Cell phone: 410-209-7108

Address: 231 Remsen Hall, 3400 N. Charles St. Baltimore, MD 21218

EDUCATION

2010.07 – Present Ph.D. Candidate, Johns Hopkins University, Department of Chemistry

2006.09 – 2010.07 B.S. Chemistry, University of Science and Technology of China (USTC), Department of Chemical Physics

RESEARCH EXPERINCE

2011.01 – Present Department of Chemistry, Johns Hopkins University

Supervisor: Prof. Arthur E. Bragg

Research Topics: Studies of exciton conformational dynamics of poly- and oligo-thiophenes, photoinduced isomerization mechanism and singlet fission in 1,2-dicyanothene derivative photoswitch, charge separation and recombination in molecular silicon, and excited-state hydrogen shift in benzoindolizines by means of femtosecond stimulated Raman and transient absorption spectroscopies

2009.09 – 2010.07 Division of Theoretical and Computational Sciences, Hefei National Laboratory for Physical Sciences at the Microscale (HFNL)

Supervisor: Prof. Jinlong Yang

Research Topics: First-principles study of luminescent behavior of the graphene quantum dot

2009.07 – 2009.08 The State Key of Molecular Reaction Dynamics, Institute of Chemistry,

Chinese Academy of Sciences (ICCAS)

Supervisor: Prof. Weijun Zheng

Research Topics: Laser dissociation of the Mn-S binary clusters

HONORS

2016.05	Shepard Memorial Travel Award, Johns Hopkins University
2016.03	Chinese Government Award for Outstanding Self-Financed Students Abroad, China Scholarship Council
2015.05	Langmuir-Cresap Fellowship, Johns Hopkins University
2010.07	Honors Degree in Physical Sciences, USTC
2008.09	Outstanding Student Scholarship (Grade Two), USTC
2007.09	Outstanding Student Scholarship (Grade Two), USTC

Teaching Experience

AS.030.101 (01) Introductory Chemistry I (Teaching assistance)

AS.030.306 (01) Physical Chemistry Instrumentation Laboratory II (Teaching assistance)

AS.030.308 (01) Elementary Computational Chemistry (Teaching assistance)

AS.030.690 (01) Intermediate Computational Chemistry (Teaching assistance)

AS.030.693 (01) Methods in Time-Resolved Spectroscopy (Teaching assistance)

Languages Spoken

Mandarin and Cantonese Chinese (native), English (fluent), German (comfortable), French (basic)

Publication

(12) **Zhou, J.**; Surampudi, S.; Klausen, R. S.; Bragg, A. E., “Photoinduced Charge Separation and Charge Recombination in σ-π Conjugated Organsilanes” *J. Phys. Chem. C* in preparation

(11) Zhao, X.; Madan, D.; **Zhou, J.**; Liu, F.; He, B.; Ireland, R. M.; Alley, O. J.; Liu, Y.; Russell, T. P.; Bragg, A. E.; Katz, H. E., “Synthesis and Structure of Main-chain Electron-deficient Ring-Linked and Bromide-Dopable Naphthalenetetracarboxylic Diimide Polymers as Unipolar Electron-carrying Semiconductors” *J. Am. Chem. Soc.* in preparation

(10) **Zhou, J.**; Outlaw, V. K.; Townsend C. A.; Bragg, A. E., “Quenching of Acid-Responsive Luminescence in Benzoindolizines by Photoinduced Hydrogen Shift” *Chem. Eur. J.* accepted

(9) Bragg, A. E.; Yu, W.; **Zhou, J.**; Magnanelli, T., “Probing Structure Dynamics, and Disorder of Excitonic States in Conjugated Organic Polymers and oligomers with Raman Spectroscopy” *J. Phys. Chem. Lett.* accepted (invited Perspective)

(8) Outlaw, V. K.; **Zhou, J.**; Bragg, A. E.; Townsend C. A., “Unusual Blue-Shifted Acid-Responsive Photoluminescence Behavior in 6-Amino-8-cyanobenzo[1,2-b]indolizines.” *RSC Adv.* **2016,** *6,* 61249-61253.

(7) Yu, W.; Magnanelli, T.; **Zhou, J.**; Bragg, A. E., “Structural Heterogeneity in the Localized Excited States of Poly(3-Hexylthiophene).” *J. Phys. Chem. B* **2016,** *120,* 5093-5102.

(6) **Zhou, J.**; Surampudi, S.; Bragg, A. E.; Klausen, R. S., “Photoinduced Charge Separation in Molecular Silicon” *Chem. Eur. J.* **2016**, *22*, 6204-6207.

(5) **Zhou, J.**; Yu, W.; Bragg, A. E., “Structural Relaxation of Photoexcited Quaterthiophenes Probed with Vibrational Specificity.” *J. Phys. Chem. Lett.* **2015,** *6*, 3496-3502.

(4) **Zhou, J.**; Guo, X.; Katz, H. E.; Bragg, A. E., “Molecular Switching via Multiplicity-Exclusive E/Z Photoisomerization Pathways.” *J. Am. Chem. Soc.* **2015,** *17*, 10841-10850.

(3) Guo, X.; **Zhou, J.**; Siegler, M. A.; Bragg, A. E.; Katz, H. E., "Visible-light-triggered molecular photoswitch based on reversible E/Z isomerization of a 1,2-dicyanoethene derivative." *Angew. Chem., Int. Ed.* **2015,** *54*, 4782-4786. (Hot paper)

(2) Yu, W.; Donohoo-Vallett, P. J.; **Zhou, J.**; Bragg, A. E., "Ultrafast photo-induced nuclear relaxation of a conformationally disordered conjugated polymer probed with transient absorption and femtosecond stimulated Raman spectroscopies." *J. Chem. Phys.* **2014,** *141*, 044201.

(1) Yu, W.†; **Zhou, J.†**; Bragg, A. E., "Exciton Conformational Dynamics of Poly(3-hexylthiophene) (P3HT) in Solution from Time-Resolved Resonant-Raman Spectroscopy." *J. Phys. Chem. Lett.* **2012,** *3*, 1321-1328. († Equal contribution)